Knut Nordanger

# Two-dimensional simulation methods for offshore wind turbines

Doctoral Thesis

Knut Nordanger

**NTNU**
Norwegian University of
Science and Technology
Faculty of Information Technology,
Mathematics and Electrical Engineering
Department of Mathematical Sciences

**NTNU – Trondheim**
Norwegian University of
Science and Technology

**NTNU – Trondheim**
Norwegian University of
Science and Technology

NTNU

Knut Nordanger

# Two-dimensional simulation methods for offshore wind turbines

Thesis for the degree of Philosophiae Doctor

Trondheim, May 2015

Norwegian University of Science and Technology

**NTNU**
Norwegian University of Science and Technology

Thesis for the degree of Philosophiae Doctor

To all those who have believed in me.

# Preface

This thesis is submitted in partial fulfillment of the requirements for the degree of philosophiae doctor (PhD) at the Norwegian University of Science and Technology, NTNU. The work for this thesis has been carried out at the Department of Mathematical Sciences in the period from November 2010 to December 2014. It has been funded by the Norwegian Research Centre for Offshore Wind Technology (NOWITECH) and the Research Council of Norway. The financial funding is greatly acknowledged.

First of all I would like to thank my supervisor Trond Kvamsdal for his guidance and support during the period I have worked with this thesis. In particular I am grateful for his continued positive attitude and that he has introduced me to the international research community through many conferences around the world. I would also like to thank Runar Holdahl (now at Statoil), Arne Morten Kvarving, Knut Morten Okstad and Adil Rasheed, all excellent researchers at SINTEF ICT, who all have been of great assistance and inspiration to me, and also contributed to the papers included in this thesis. Particularly I would like to thank Adil for the tremendous support and motivation he has given me during the last seven months. Fellow researchers Mukesh Kumar and Kjetil André Johannessen also deserve thanks.

I am grateful that I was allowed through the NOWITECH Mobility Programme to stay at the Fraunhofer Institute for Wind Energy and Energy System Technology in Oldenburg, Germany for four months from April to July 2013. Being part of the CFD group of Bernhard Stoevesandt was a great pleasure for both me and my girlfriend Silje, and provided a huge boost for my work on turbulence modelling.

During the work with this thesis I have been partly on leave from my employer IKM Ocean Design, but still held a 25% position there. Being able to keep contact with the industry has been important for me, and the flexibility shown has been invaluable.

Lastly I would like to thank my familiy and especially my girlfriend Silje Aunehaugen for the continued support and encouragement she has shown through the past four years. This thesis would not have seen the light without the understanding and patience she has shown, and I think she is about as happy as me when it now is finalized.

# Contents

# Introduction

## 1.1 Background for offshore wind

The energy market is changing. With an increased focus on generating electricity from renewable sources, together with serious nuclear power incidents and stagnation in oil and gas, wind power has been identified as a power source that can be utilized in most parts of the world. However, onshore based wind farms have traditionally been controversial due to noise and visual impact issues. In order to overcome such show-stoppers offshore wind has emerged as an attractive alternative. Offshore wind conditions are often better and more stable than onshore, and transportation and access for maintenance can be handled by sea eliminating the need for road transport. Also, offshore wind turbines can be much larger than their onshore counterparts.

Many countries have in recent years increased their wind production, often as a consequence of ambitious goals for investments and development of offshore wind power. By the end of 2013 there were 117.3 GW of installed wind power in the European Union (EU) [50], of which 110.7 GW were onshore and 6.6 GW were offshore. Of the total offshore capacity 1.6 GW were installed during 2013 with similar prospects for the following years. During the first half of 2014 781 MW of increased capacity have been installed for a total of 224 wind turbines [49]. This increases the total number of installed offshore wind turbines in the EU to around 2300. The average size of the wind turbines are now 4 MW [48]. Such a turbine typically has a rotor diameter of around 130 m.

In the US there were, by the end of 2013, around 61.1 GW of total installed wind power, of which almost nothing was installed offshore [67]. China had a total installed capacity of around 91.4 GW. The capacity of Chinese offshore wind power

amounts to 428.6 MW. China in particular has huge plans to increase the installed capacity.

Bigger wind turbines exist and are under testing. These include the SeaTitan 10 MW wind turbine with a rotor diameter of 190 m [4], the Areva 8 MW wind turbine with a rotor diameter of 180 m [7] and the MHI Vestas 8 MW wind turbine with a rotor diameter of 164 m [110].

## 1.2   Current wind turbine analysis techniques

Onshore wind is becoming a mature industry with well-established calculation and analysis techniques [103]. These techniques are not necessarily directly transferable to analyses of offshore wind turbines. In particular there is a greater need for dynamic analyses of offshore wind turbines as the structures are much larger.

The significant increase in wind turbine sizes has required a more sophisticated toolbox of simulation techniques [69]. The wind turbines of the early 1980s had rotor diameters of $10 - 15$ m, while new offshore wind turbines today can have rotor diameters of around 130 m. From simple design rules of thumb, via static finite element analysis, to fully dynamic finite element analysis, the larger wind turbine sizes have increased the demand for more involving and accurate analysis methods [70]. Prediction of wind turbine blade aerodynamic loads requires determination of the wind loads on the structure and calculation of the structural response. This can be done through an aeroelastic model or, as we will focus on here, fluid-structure interaction (FSI).

There are four main methods of predicting the aerodynamic loads on a wind turbine [70]. Firstly, we have the blade element momentum (BEM) method, as introduced in [62]. This method is quite fast and therefore well-suited in an engineering design phase. However, the method is dependent on detailed airfoil data in terms of lift and drag curves as functions of the angle of attack $\alpha$ and the Reynolds number, $Re$. The method assumes that all sections along the blade can be treated independently. Secondly, there are the 3D inviscid aerodynamic models. These include the lifting line, panel and vortex models and allow a more detailed description of the 3D flow around a wind turbine. The methods, however, neglect viscous effects. Thirdly, we have the generalized actuator disc models that are well-suited for analyzing rotor performance. They can be combined with blade element theory or Navier-Stokes simulations. Popular aeroelastic codes simulating the response of wind turbines include FAST [114], HAWC2 [47] and Ashes [127]. Lastly, Navier-Stokes simulations of wind turbines can include more physics and provide more insight than the other methods at a significantly higher cost. Such computational fluid dynamics (CFD) simulations have gained much popularity in

the recent decade, both due to increased computational power and improved computational methods. However, simulations in 3D can be very challenging [70]. Still, CFD is the method of choice in this thesis, as it can provide valuable insight in itself as well as produce valuable input for other methods. For instance, CFD simulations can provide spanwise distributions of force coefficients and sectional pressure distributions along the blade span. Aspects of turbulence will be discussed later.

In order to do full elastic computations of wind turbine rotors the codes for predicting aerodynamic loads should be coupled to a structural code. When it comes to structural modeling of wind turbines there are two main approaches [70]. The first is to use the method of virtual work applied on modal shape functions. This reduces the total number of degrees-of-freedom in the system and thus reduces the computational cost. The second is to use the finite element method applying non-linear beam theory [124]. This is the most commonly used approach today.

## 1.3    Isogeometric analysis

When doing advanced numerical simulations it is important not only to focus on the computational costs. The overall simulation efficiency must also be kept in mind. This includes the time consumption related to modeling, analysis and interpretation of results. Investigations have shown that the lack of interoperability between using modern computer aided design (CAD) systems and classical finite element analysis is a major bottleneck [40]. In fact, it is estimated that 80% of the overall analysis time is used to prepare geometries, meshes and input for finite element analysis.

In order to address the major bottleneck isogeometric analysis (IGA) was introduced in 2005 [86]. This concept is characterized by using splines, i.e. B-splines or non-rational uniform B-splines (NURBS), as basis functions in the finite element analysis as well as in the CAD system. In turn, this opens up for exact geometric modeling, which can be of utmost importance when it comes to modeling aerodynamically shaped objects like airfoils. Traditional finite element meshes are only approximations of the real geometries, e.g. consider the number of element necessary to mesh a cylinder surface accurately. Furthermore, isogeometric analysis gives better accuracy per degree-of-freedom than more traditional methods.

## 1.4    Computational fluid dynamics (CFD)

### 1.4.1    General CFD

There are several technologies available for simulating fluid flow, and a comprehensive overview of many different methods can be found in [97]. Among others

we have finite elements [29], finite volumes [13], finite differences [8] and spectral elements [33]. Popular finite element codes include the commercial COMSOL Multiphysics [39] and the freely available FEniCS [102] and deal.II [12]. When it comes to finite volume codes the commercial codes ANSYS CFX [5], ANSYS Fluent [6] and StarCCM+ [36] are widely used. Also the freely available finite volume code OpenFoam [115] is in active use by many applied research groups.

This thesis is focused on a new development in finite element methods, the isogeometric finite element method as introduced in [86], and explained in the previous section.

Our main equations of interest will be the incompressible Navier-Stokes equations, which are a mathematical description of subsonic, viscous flow. They can be written as

$$\rho\frac{\partial \boldsymbol{u}}{\partial t} + \rho\left(\boldsymbol{u}\cdot\nabla\right)\boldsymbol{u} - \nabla\cdot\boldsymbol{\sigma}\left(\boldsymbol{u},p\right) = \rho\boldsymbol{f} \quad \text{in } \Omega$$
$$\nabla\cdot\boldsymbol{u} = 0 \quad \text{in } \Omega. \tag{1.1}$$

We require $\Omega \in \mathbb{R}^d$, $d = 2,3$ to a suitable, sufficiently regular and open domain. Furthermore, we define $\rho$ to be the constant fluid density, $p$ to be the pressure, $\boldsymbol{u}$ to be the fluid velocity vector and $\boldsymbol{f}$ to be a volumetric body force. The Cauchy stress tensor can be written as

$$\boldsymbol{\sigma}(\boldsymbol{u},p) = -p\boldsymbol{I} + 2\mu\boldsymbol{\epsilon}(\boldsymbol{u}),$$

where $\boldsymbol{I}$ is the identity tensor, $\mu$ the dynamic viscosity and the strain rate $\boldsymbol{\epsilon}$ is defined as

$$\boldsymbol{\epsilon}(\boldsymbol{u}) = \frac{1}{2}\left(\nabla\boldsymbol{u} + (\nabla\boldsymbol{u})^T\right).$$

When solving the Navier-Stokes equations one can either choose to solve for both the velocity and pressure unknowns simultaneously. This gives a so-called coupled approach. Another approach is employed in splitting or projection methods. Here, the velocity and pressure are decoupled. This thesis is mainly concerned with projection methods, but a coupled solver is used for comparison purposes in Paper II.

As projection methods involve solution of several decoupled systems of parabolic or elliptic equations at each time step, they can be more efficient that fully coupled formulations. The decoupled systems can be solved by standard Krylov subspace methods like the conjugate gradient method [76, 119] or GMRES [120] with efficient preconditioners like multigrid [75] or domain decomposition [128]. Some

results for iterative solvers applied to isogeometric finite elements can be found in [38]. However, projection methods are plagued by the fact that high-order methods are hard to design and analyze due to the additional unphysical boundary conditions introduced.

There are several projection methods available and a recent review is given in [65]. Initial developments were done by Chorin [37] and Temam [141]. These methods or schemes are commonly divided into two main groups: pressure-correction schemes and velocity-correction schemes. In pressure-correction schemes the pressure is either ignored or treated explicitly in a separate step before it is corrected by projection of a temporary velocity found in the separate step. Velocity-correction schemes on the other hand switch the roles of velocity and pressure. Other splitting schemes also exist, and the reader is referred to [65].

It is well-known that equal order approximations can suffer from spurious pressure oscillations as they do not satisfy the Ladyzhenskaya-Brezzi-Babuska (LBB) condition [30]. In order to avoid this one has to choose velocity and pressure approximations of inequal order or introduce some kind of stabilization. The most common form of remedy is to use different discretizations for the velocity and pressure spaces in order to make the approximation LBB stable.

A general reference to the performance of the methods is [64]. Investigations in [147] indicate that the Chorin-based incremental pressure correction technique is among the most efficient and accurate methods. In this work we employ the incremental pressure correction scheme in both standard and rotational forms as described in [65]. As only equal order approximations are used we will for some problems employ Minev stabilization as described in [112] in order to avoid spurious node-to-node pressure oscillations.

Flows at high Reynolds numbers around objects like airfoils and cylinders are mostly turbulent. Due to the high computational cost of explicit resolution of all scales using Direct Numerical Simulation (DNS), turbulence modeling is required. There are two main approaches when it comes to modeling turbulence, Reynolds-Averaged Navier-Stokes (RANS) or Large Eddy Simulation (LES) models. In models employing RANS all scales are modeled. In LES on the other hand only, the small isotropic scales are modeled while the larger energy-containing scales are resolved.

RANS models are very popular due to their speed, particularly in applied communities, and as such there many models available. For the last 20 years many people have expected LES to replace RANS modelling, but due to the computational expenses involved this has not happened [132]. Common to all RANS

models is the time-averaging that introduces new unknowns through the Reynolds stress tensor. These new unknowns require additional equations to be solved, and this is remedied through the various turbulence models. All these turbulence models rely on the Boussinesq assumption that turbulent eddies can be modeled through an eddy viscosity [125].

RANS models are commonly divided into three classes; algebraic or zero-equation models, one-equation models and two-equation models. Algebraic models do not solve any additional transport equation, but calculates the eddy viscosity $\nu_t$ directly. The most popular of these is the Baldwin-Lomax model [10]. The one-equation models on the other hand solve one transport equation in order to determine the turbulent viscosity. One of the most popular one-equation models is the Spalart-Allmaras turbulence model presented in [133] with some updates and modifications in [3]. It is specifically tuned for aerodynamically shaped objects, and is considered to be both robust and stable. Another popular one-equation model is the Baldwin-Barth model [11]. Many of the commercial CFD codes offer some of the two-equation RANS models, which solve two equations for computing the turbulent quantities. Important and popular methods include the $k - \epsilon$ model [89, 99, 100], the $k - \omega$ model [155, 154] and the $k - \omega\ SST$ model [108]. In these models $k$ is the turbulent kinetic energy, $\epsilon$ is the turbulent dissipation and $\omega$ is the specific dissipation. For further details the reader is referred to the references.

LES models use an eddy viscosity to model the interaction between the small unresolved scales with the larger scales [121, 14]. Variational multi-scale modelling (VMS) is a certain subclass of LES. The variational multi-scale model was introduced by Hughes [85] and further developed in [32, 16]. In this model the use of eddy viscosities is abandoned and subgrid velocity and pressure are modelled. Instead of eddy viscosities this model derives the modeling terms from a weak formulation of the incompressible Navier-Stokes equations [14].

Combinations of RANS and LES models are denoted detached eddy simulation (DES) models [134, 137, 131]. These models can be easier than LES to apply, particularly in the boundary layer, as a RANS model is applied there. There are also other alternatives to computing turbulence, e.g through the General Galerkin (G2) framework, see [77, 78, 79]. These models circumvent introduction and modeling of the Reynolds stresses in the averaged Navier-Stokes equations and are known as adaptive DES/LES models.

Isogeometry has been applied for pure CFD simulations for many years now. It started in [26] with turbulence modeling. Particular good results for isogeometry were achieved in [2], where the increased continuity of basis functions gave improved results. Notable results for isogeometric VMS can be found in [19] and for

isogeometric LES in [14].

### 1.4.2   CFD and wind turbines

The general CFD codes mentioned in the previous subsection are also commonly used for wind turbine analyses. Also, there are some known in-house CFD codes like Ellipsys2D/3D [46].

The first major use of CFD for wind turbines was in the prediction of 2D airfoil characteristics for wind turbine blade design [138]. Such simulations can be compared with the many wind tunnel experiments of airfoils available in the literature [55]. During code development these results can be applied in the code verification process. For NACA airfoils [1] is a very good reference. Comparisons with experiments have been done in this thesis, and the reader is referred to Paper I and Paper II. CFD simulations have some benefits compared to wind tunnel experiments [55]. Firsty, CFD is for instance infinitely scalable and provides field, not point, data [138]. Secondly, CFD simulations can be very useful in a planning phase and offer better interpretation of the actual physics [70].

Simulations in 2D have a number of drawbacks. Modelling of the transition to turbulence in the boundary layer is one of them. Stall operation can thus be difficult to simulate. However, several methods are available to predict the onset of transition. The currently most used one is the $\gamma - Re_{\theta,t}$ model, originally published in [109] and with further developments in [98]. This model has also has been adapted for use with the Spalart-Allmaras turbulence model in [105]. Transition modelling is not used in the simulations presented in this thesis.

To overcome some of the difficulties with two-dimensional simulations, simulations in three spatial dimensions are a natural extension. However, the computational expense is increased significantly [138]. Additionally, one must consider whether the increased complexity of 3D simulations gives added value compared to much cheaper 2D simulations [129].

## 1.5   Fluid-structure interaction (FSI)

### 1.5.1   General FSI

For many practical applications pure computational fluid dynamics is not adequate. Structural aspects need to be considered and often together with mutual interaction of the fluid. Such problems are denoted fluid-structure interaction (FSI) problems. These problems can often be computationally demanding due to complex geometries and complicated interaction effects [28].

There are two main groups of methods for fluid-structure interaction [9]. These are

coupled or monolithic methods [63, 150, 84, 87] and partitioned or staggered methods [56, 57, 117, 54], which are most commonly used. Partitioned methods can be further divided into loosely and strongly coupled methods. In loosely-coupled approaches the fluid and structure equations are integrated once and independently at each time step. Often a so-called Dirichlet-Neumann coupling is employed [9]. This involves Dirichlet conditions at the interface for the fluid problem, corresponding to continuity of the velocities, and Neumann conditions at the interface for the structural problem, corresponding to continuity of the stresses. Initial applications for fluid-structure interactions were in aeroelastics where the fluid density, $\rho_f$, was significantly less than the structural density $\rho_s$, i.e. $\rho_s >> \rho_f$ [51, 116]. For each time step only one or a couple of iterations are necessary for convergence. When the fluid density is increased, tighter coupling is required which results in more subiterations for each time step. This is evidence of the added mass effect [148, 113]. The method now becomes a strongly-coupled partitioned method as the computations for the fluid and structure are repeated at each time step until a given convergence criterion is reached. The computational cost is thus higher, but the approach is required for achieving energy conservation at the fluid-structure interface [51, 146]. In cases where the fluid density and the structural density are of the same order convergence is much slower and can even fail [101]. Strongly-coupled approaches are also called implicitly partitioned approaches [123, 136, 153].

However, partitioned methods can suffer from instability and inaccuracy issues [152]. In order to overcome convergence issues for partitioned methods relaxation can be introduced. This has a stabilizing effect with the drawback that convergence can be very slow [35]. Measures such as dynamic relaxation exist [94] that to some extent speed up the convergence. Robust Krylov methods, as presented in [111, 60], or interface Newton-Raphson methods, as in [42], are other alternatives. Overviews are given in [59, 149]. These approaches can be more robust and computationally cheaper than employing subiterations.

Coupled methods on the other hand involve development of a solver that solves the fluid and structural equations simultaneously [23]. This involves more coding as the complete non-linear system of fluid and structural equations are discretized identically in space and time and solved simultaneously [68]. Coupled methods are often considered to be more robust [71].

Benefits of partitioned methods include that existing fluid and structure solvers can be used, i.e. software modularity is maintained. Often these solvers have reached a high level of maturity and can as such be well suited for the application in question. Different discretizations can be used for each subproblem. For instance a finite volume discretization can be employed for the fluid flow problem and a finite element discretization for the structural problem [92]. One great advantage of

partitioned approaches is that the coupling is limited to the fluid-structure interface only. Aspects of efficient implementation can be found in [106, 93]. Even though there are huge benefits of combining solvers within the same framework [63], there also exist several frameworks available that can be used to couple existing codes. These include preCICE [31] and MpCCI [90].

An important aspect of fluid-structure interaction is how deformation of the computational meshes shall be handled. One common approach is to use the arbitrary Lagrangian-Eulerian framework [44, 58, 61, 45, 130]. For fluid one typically uses an Eulerian formulation, while a Lagrangian formulation is commonly used for the structure [151, 104]. Mesh movement algorithms thus also becomes an issue [96, 135].

For some cases where the deformations are small compared to the displacements and rotation of the centre of gravity the structure can be considered a rigid body [122, 107]. Such cases are denoted fluid-rigid body interaction and are a special subclass of fluid-structure interaction problems. This approach is commonly employed to simulate vortex-induced vibrations [139, 140].

When it comes to benchmark cases for FSI flow past a fixed cylinder with flexible bar attached by Turek and Hron [142, 144, 143] has become an industry standard for low Reynolds numbers. This case is a purely numerical test case, and is investigated in Paper III. For turbulent flows a similar case with both experimental and numerical data for comparison has been published recently [41].

Isogeometric fluid-structure interaction has been an active research area ever since isogeometry was introduced to the research community in 2005. Notable results include [26, 15, 17].

### 1.5.2   FSI and wind turbines

Fluid-structure interaction is one of the most challenging problems in computational mechanics these days. Although it has attracted interest from many theoretical researchers, it is applied daily in as vastly different fields as submarine risers [73], biomechanics [15, 18], bridge engineering [88, 95] and not to say the least, airfoils and wind turbines.

The first relevant results for wind turbine application were presented for aerolastics [117, 52, 53, 91]. Along with the political momentum renewable energy and wind turbines have gained in recent, applied research for these applications are increasingly more commonly seen.

Some of the first results for airfoil and wind turbines had simplified structural models as in [66, 43]. Such models are still relevant, and recently there has been

investigation of airfoils with self-adaptive camber [145], which are relevant for the active research area involving so-called smart wind turbine blades.

In recent years there has been much progress in simulating complete wind turbines [20, 21, 81, 22, 80, 82, 24, 25]. Of particular interest is that these full machine simulations are done using isogeometric methods. Very recent results also include validation against full-scale experiments [83]. Another example of wind turbine FSI is [34], where a beam model is used for the blade. Also, there are results available for multiscale simulations of wind turbines [118].

## 1.6   Summary

Based on the discussion above the main goal of this thesis is to apply isogeometric analysis for developing effective methods for doing computations relevant for offshore wind applications. CFD analyses of wind turbine blade sections at realistic flow conditions and high Reynolds numbers will thus be carried out and analysed. In order to keep the computational cost as low as possible we will focus on development of a CFD solver based on a Chorin splitting technique [37, 65, 112] with application of the Spalart-Allmaras RANS turbulence model [133]. However, comparisons based on solution quality and computational cost will be done with a VMS solver based on [16]. Two-dimensional CFD analyses allow us to determine lift, drag and pressure coefficients of airfoil sections. These can be used as input for other methods for full wind turbine analysis, or in a process of airfoil shape optimization.

Secondly, this thesis makes some investigations for low Reynolds number fluid-structure interaction simulations. This is done in order to determine whether the coupling of isogeometric fluid and structural solvers can give any advantages. This is done for a 2D benchmark case [142, 143] which can be interpreted as an approximation of a flexible turbine blade. The Chorin-based fluid solver is used for these simulations as well.

Reliable results from two-dimensional CFD analyses open up new possibilities for wind turbine blade analysis. Previously, the so-called strip-theory approach has been applied for studying vortex-induced vibrations of subsea risers [72, 73, 74, 126, 27]. By coupling several such two-dimensional sections through a beam element, it will be possible to carry out analyses of wind turbine blades. Thus both the CFD and FSI results in this thesis can be used as pillars for developing such a strip-theory or semi-3D approach for wind turbine blade application.

## 1.7    Summary of papers

The thesis consists of an introduction to the field of wind turbines, computational fluid dynamics, fluid-structure interaction and isogeometry along with three papers that are either published, conditionally accepted or submitted to international peer-reviewed journals.

### 1.7.1    Paper I: *Simulation of airflow past a 2D NACA0015 airfoil using an isogeometric incompressible Navier-Stokes solver with the Spalart-Allmaras turbulence model*

The first paper presents our incompressible Navier-Stokes solver and results from simulations of air flow past a fixed 2D NACA0015 airfoil at high Reynolds number ($Re = 2.5 \times 10^6$) using an isogeometric finite element methodology with linear, quadratic and cubic spline elements. The fluid solver is based on a Chorin projection method and employs the Spalart-Allmaras turbulence model, the first development of its kind in an isogeometric finite element framework. The obtained results from the simulations are compared with two sets of experimental results available in the literature, with emphasis on determining the effect of using higher order spline elements in the analysis. Our results indicate that there is little to be gained for using quadratic and cubic spline elements for this type of simulations.

### 1.7.2    Paper II: *Implementation and comparison of three isogeometric Navier-Stokes solvers applied to simulation of flow past a fixed 2D NACA0012 airfoil at high Reynolds number*

The second paper presents the implementation of three different Navier-Stokes solvers in an isogeometric finite element framework. The first two solvers are the Chorin projection method and a coupled formulation, both with the Spalart–Allmaras turbulence model, and the third solver is the Variational Multiscale (VMS) method. All solvers are applied to simulate flow past a two-dimensional NACA0012 airfoil at a high Reynolds number ($Re = 3 \times 10^6$) for four different angles of attack. The predicted flow characteristics are compared and the effects of increasing the order of the spline elements on the accuracy of prediction and computational efficiency is evaluated. Up to an angle of attack of $16°$, where flow separation takes place, all three solvers predict similar results in good agreement with each other and with available experimental results. However, a big spread in lift and drag coefficients is observed in the stall regime. The paper also shows that for linear spline elements all three solvers are computationally similar. For quadratic spline elements the Chorin solver compares favorably to the other two.

### 1.7.3    Paper III: *Numerical benchmarking of fluid-structure interaction: An isogeometric finite element approach*

In the third paper a Chorin-based Navier-Stokes solver is applied to a well-known benchmark problem for fluid-structure interaction at $Re = 100$ for flow past a circular cylinder with an attached flexible bar. Several aspects are investigated. Firstly, the impact of linear, quadratic and cubic spline elements are evaluated. Secondly, the impact of the mesh stiffness on the results are investigated along with four metrics of mesh quality and variation in total computational time. All results for lift, drag and displacements are compared with published benchmark results. Our simulations indicate that quadratic and cubic spline elements give better estimation of lift, drag and displacements than linear spline elements.

# Bibliography

[1] I. H. Abbott and A. E. von Doenhoff. *Theory of wing sections*. Dover Publishing, 1959.

[2] I. Akkerman, Y. Bazilevs, V.M. Calo, T.J.R. Hughes, and S. Hulshoff. The role of continuity in residual-based variational multiscale modeling of turbulence. *Computational Mechanics*, 41(3):371–378, 2008.

[3] S. R. Allmaras, F. T. Johnson, and P. R. Spalart. Modifications and clarifications for the implementation of the Spalart-Allmaras turbulence model. In *Proceedings of the 7th International Conference on Computational Fluid Dynamics, ICCFD7*, 2012.

[4] AMSC. Seatitan 10 MW wind turbine. `http://www.amsc.com/documents/seatitan-10-mw-wind-turbine-data-sheet/`, 2014. Accessed 18.12.2014.

[5] ANSYS. ANSYS CFX web page. `http://www.ansys.com/Products/Simulation+Technology/Fluid+Dynamics/Fluid+Dynamics+Products/ANSYS+CFX`, 2014. Accessed 18.12.2014.

[6] ANSYS. ANSYS Fluent web page. `http://www.ansys.com/Products/Simulation+Technology/Fluid+Dynamics/Fluid+Dynamics+Products/ANSYS+Fluent`, 2014. Accessed 18.12.2014.

[7] Areva. Main features of the Areva 8 MW wind turbine. `http://www.areva.com/EN/operations-4430/areva-offshore-wind-innovative-technology.html`, 2014. Accessed 18.12.2014.

[8] O. Axelsson. *Encyclopedia of Computational Mechanics*, chapter Finite Difference Methods, pages 7–54. John Wiley, Nijmegen, the Netherlands, 2004.

[9] S. Badia, A. Quaini, and A. Quarteroni. Modular vs. non-modular preconditioners for fluid-structure systems with large added-mass effect. *Computer Methods in Applied Mechanics and Engineering*, 197(49-50):4216–4232, 2008.

[10] B. Baldwin and H. Lomax. Thin-layer approximation and algebraic model for separated turbulent flows. In *16th Aerospace Sciences Meeting*, number 1978-257. AIAA, 1978.

[11] B. S. Baldwin and T. J. Barth. A one-equation turbulence transport model for high Reynolds number wall-bounded flows. Technical Memorandum NASA TM-102847, National Aeronautics and Space Administration, August 1990.

[12] W. Bangerth, R. Hartmann, and G. Kanschat. deal.II – a general purpose object oriented finite element library. *ACM Transactions on Mathematical Software*, 33(4):24/1–24/27, 2007.

[13] T. Barth and M. Ohlberger. *Encyclopedia of Computational Mechanics*, chapter Finite Volume Methods: Foundation and Analysis, pages 439–473. John Wiley, 2004.

[14] Y. Bazilevs and I. Akkerman. Large eddy simulation of turbulent Taylor-Couette flow using isogeometric analysis and the residual-based variational multiscale method. *Journal of Computational Physics*, 229(9):3402–3414, 2010.

[15] Y. Bazilevs, V.M. Calo, Y. Zhang, and T.J.R. Hughes. Isogeometric fluid-structure interaction analysis with applications to arterial blood flow. *Computational Mechanics*, 38(4-5):310–322, 2006.

[16] Y. Bazilevs, V. M. Calo, J. A. Cottrell, T. J. R. Hughes, A. Reali, and G. Scovazzi. Variational multiscale residual-based turbulence modeling for large eddy simulation of incompressible flows. *Computer Methods in Applied Mechanics and Engineering*, 197:173–201, 2007.

[17] Y. Bazilevs, V.M. Calo, T.J.R. Hughes, and Y. Zhang. Isogeometric fluid-structure interaction: Theory, algorithms, and computations. *Computational Mechanics*, 43(1):3–37, 2008.

[18] Y. Bazilevs, M.-C. Hsu, Y. Zhang, W. Wang, T. Kvamsdal, S. Hentschel, and J.G. Isaksen. Computational vascular fluid-structure interaction: Methodology and application to cerebral aneurysms. *Biomechanics and Modeling in Mechanobiology*, 9(4):481–498, 2010.

[19] Y. Bazilevs, C. Michler, V.M. Calo, and T.J.R. Hughes. Isogeometric variational multiscale modeling of wall-bounded turbulent flows with weakly enforced boundary conditions on unstretched meshes. *Computer Methods in Applied Mechanics and Engineering*, 199(13-16):780–790, 2010.

[20] Y. Bazilevs, M.-C. Hsu, I. Akkerman, S. Wright, K. Takizawa, B. Henicke, T. Spielman, and T.E. Tezduyar. 3D simulation of wind turbine rotors at full

scale. Part I: Geometry modeling and aerodynamics. *International Journal for Numerical Methods in Fluids*, 65(1-3):207–235, 2011.

[21] Y. Bazilevs, M.-C. Hsu, J. Kiendl, R. Wüchner, and K.-U. Bletzinger. 3D simulation of wind turbine rotors at full scale. Part II: Fluid-structure interaction modeling with composite blades. *International Journal for Numerical Methods in Fluids*, 65(1-3):236–253, 2011.

[22] Y. Bazilevs, M.-C. Hsu, and M.A. Scott. Isogeometric fluid-structure interaction analysis with emphasis on non-matching discretizations, and with application to wind turbines. *Computer Methods in Applied Mechanics and Engineering*, 249-252:28–41, 2012.

[23] Y. Bazilevs, K. Takizawa, and T.E. Tezduyar. *Computational Fluid-Structure Interaction: Methods and Applications*. Wiley Series in Computational Mechanics. Wiley, 2013. ISBN 9780470978771.

[24] Y. Bazilevs, A. Korobenko, X. Deng, and J. Yan. Novel structural modeling and mesh moving techniques for advanced fluid-structure interaction simulation of wind turbines. *International Journal for Numerical Methods in Engineering*, 2014. Article in press.

[25] Y. Bazilevs, K. Takizawa, T.E. Tezduyar, M.-C. Hsu, N. Kostov, and S. McIntyre. Aerodynamic and FSI analysis of wind turbines with the ALE-VMS and ST-VMS methods. *Archives of Computational Methods in Engineering*, 2014. Article in press.

[26] Yuri Bazilevs. *Isogeometric Analysis of Turbulence and Fluid-Structure Interaction*. PhD thesis, The University of Texas at Austin, 2006.

[27] P.W. Bearman, J.R. Chaplin, E. Fontaine, J.M.R. Graham, K. Herfjord, A. Lima, J.R. Meneghini, K.W. Schulz, and R.H.J. Willden. Comparison of CFD predictions of multi-mode vortex-induced vibrations of a tension riser with laboratory measurements. In *Proceedings of the 6th International Symposium on FSI, AE & FIV (2006 ASME Pressure Vessels and Piping Division Conference)*, volume 9, pages 147–156. ASME, 2006. PVP2006-ICPVT-11-93177.

[28] F.-K. Benra, H.J. Dohmen, J. Pei, S. Schuster, and B. Wan. A comparison of one-way and two-way coupling methods for numerical analysis of fluid-structure interactions. *Journal of Applied Mathematics*, 2011, 2011.

[29] S. C. Brenner and C. Carstensen. *Encyclopedia of Computational Mechanics*, chapter Finite Element Methods, pages 73–118. John Wiley, 2004.

[30] F. Brezzi. On the existence, uniqueness and approximation of saddle-point problems arising from Lagrangian multipliers. *Rev. Francaise Automat. Informat. Recherche Operationelle Ser Rouge*, 8, 1974.

[31] H.-J. Bungartz, J. Benk, B. Gatzhammer, M. Mehl, and T. Neckel. Partitioned simulation of fluid-structure interaction on Cartesian grids. In H.-J. Bungartz, M. Mehl, and M. Schäfer, editors, *Fluid Structure Interaction II*, volume 73 of *Lecture Notes in Computational Science and Engineering*, pages 255–284. Springer Berlin Heidelberg, 2010. ISBN 978-3-642-14205-5.

[32] V.M. Calo. *Residual-based Multiscale Turbulence Modeling: Finite Volume Simulation of Bypass Transistion*. PhD thesis, Stanford University, 2004.

[33] C. Canuto and A. Quarteroni. *Encyclopedia of Computational Mechanics*, chapter Spectral Methods, pages 141–155. John Wiley, 2004.

[34] M. Carrion, R. Steijl, G. N. Barakos, S. Gomez-Iradi, and X. Munduate. Coupled CFD/CSD method for wind turbines. In *Proceedings of WCCM XI / ECCM V / ECFD VI*, July 2014.

[35] P. Causin, J.F. Gerbeau, and F. Nobile. Added-mass effect in the design of partitioned algorithms for fluid-structure problems. *Computer Methods in Applied Mechanics and Engineering*, 194(42-44):4506–4527, 2005.

[36] CD-adapco. Star-CCM+ web page. `http://www.cd-adapco.com/products/star-ccm`, 2014. Accessed 18.12.2014.

[37] A. J. Chorin. Numerical solution of the Navier-Stokes equations. *Mathematics of Computation*, 22:745–762, 1968.

[38] N. Collier, L. Dalcin, D. Pardo, and V.M. Calo. The cost of continuity: Performance of iterative solvers on isogeometric finite elements. *SIAM Journal on Scientific Computing*, 35(2):A767–A784, 2013.

[39] COMSOL Inc. COMSOL Multiphysics web page. `http://www.comsol.com`, 2014. Accessed 18.12.2014.

[40] J.A. Cottrell, T.J.R. Hughes, and Y. Bazilevs. *Isogeometric analysis: Toward integration of CAD and FEA*. Wiley, Chichester, 2009.

[41] G. De Nayer, M. Breuer, and A. Kalmbach. Fluid-structure interaction in turbulent flows: LES predictions and PIV measurements. In J. Eberhardsteiner, editor, *European Congress on Computational Methods in Applied Sciences and Engineering (ECCOMAS 2012)*, 2012.

[42] J. Degroote, R. Haelterman, S. Annerel, P. Bruggeman, and J. Vierendeels. Performance of partitioned procedures in fluid-structure interaction. *Computers and Structures*, 88(7-8):446–457, 2010.

[43] I. Dobrev and F. Massouh. Fluid-structure interaction in the case of a wind turbine rotor. In *18ème Congrès Français de Mécanique*, 2007.

[44] J. Donea, S. Giuliani, and J.P. Halleux. An arbitrary Lagrangian-Eulerian finite element method for transient dynamic fluid-structure interactions. *Computer Methods in Applied Mechanics and Engineering*, 33(1-3):689–723, 1982.

[45] J. Donea, A. Huerta, J.-Ph. Ponthot, and A. Rodriguez-Ferran. *Encyclopedia of Computational Mechanics*, chapter Arbitrary Lagrangian-Eulerian Methods. John Wiley, Chichester, West Sussex, 2004.

[46] DTU Energy. EllipSys2D/3D web page. `http://www.risoecampus.dtu.dk/Research/sustainable_energy/wind_energy/projects/numwind/EllipSys.aspx?sc_lang=en`, 2014. Accessed 18.12.2014.

[47] DTU Energy. HAWC2 web page. `http://www.hawc2.dk/`, 2014. Accessed 18.12.2014.

[48] EWEA. The European offshore wind energy - key trends and statistics 2013. Technical report, European Wind Energy Association, 2014.

[49] EWEA. The European offshore wind energy - key trends and statistics 1st half 2014. Technical report, European Wind Energy Association, 2014.

[50] EWEA. Wind in power - 2013 European statistics. Technical report, European Wind Energy Association, 2014.

[51] C. Farhat and M. Lesoinne. Two efficient staggered algorithms for the serial and parallel solution of three-dimensional nonlinear transient aeroelastic problems. *Computer Methods in Applied Mechanics and Engineering*, 182 (3-4):499–515, 2000.

[52] C. Farhat, M. Lesoinne, P. Stern, and S. Lanteri. High performance solution of three-dimensional nonlinear aeroelastic problems via parallel partitioned algorithms: Methodology and preliminary results. *Advances in Engineering Software*, 28(1):43–61, 1997.

[53] C. Farhat, K.G. van der Zee, and P. Geuzaine. Provably second-order time-accurate loosely-coupled solution algorithms for transient nonlinear computational aeroelasticity. *Computer Methods in Applied Mechanics and Engineering*, 195(17-18):1973–2001, 2006.

[54] C. Farhat, A. Rallu, K. Wang, and T. Belytschko. Robust and provably second-order explicit-explicit and implicit-explicit staggered time-integrators for highly non-linear compressible fluid-structure interaction problems. *International Journal for Numerical Methods in Engineering*, 84(1):73–107, 2010.

[55] D. Favier. *The Role of Wind Tunnel Experiments in CFD Validation*. John Wiley & Sons, Ltd, 2010. ISBN 9780470686652.

[56] C.A. Felippa and K.C. Park. Staggered transient analysis procedures for coupled mechanical systems: Formulation. *Computer Methods in Applied Mechanics and Engineering*, 24(1):61–111, 1980.

[57] C.A. Felippa, K.C. Park, and C. Farhat. Partitioned analysis of coupled mechanical systems. *Computer Methods in Applied Mechanics and Engineering*, 190(24-25):3247–3270, 2001.

[58] L. Formaggia and F. Nobile. Stability analysis for the arbitrary lagrangian eulerian formulation with finite elements. *East-West Journal of Numerical Mathematics*, 7(2):105–131, 1999.

[59] T. Gallinger and K.-U. Bletzinger. Comparison of algorithms for strongly coupled partitionned fluid-structure interaction - efficiency versus simplicity. In J. Pereira, A. Sequeira, and J.M. Pereira, editors, *Proceedings of the V European conference on computational fluid dynamics ECCOMAS CFD*, pages 1–20, 2010.

[60] J.-F. Gerbeau, M. Vidrascu, and P. Frey. Fluid-structure interaction in blood flows on geometries based on medical imaging. *Computers and Structures*, 83(2-3):155–165, 2005.

[61] P. Geuzaine, C. Grandmont, and C. Farhat. Design and analysis of ALE schemes with provable second-order time-accuracy for inviscid and viscous flow simulations. *Journal of Computational Physics*, 191(1):206–227, 2003.

[62] H. Glauert. Airplane propellers. In *Aerodynamic Theory*, pages 169–360. Springer Berlin Heidelberg, 1935.

[63] C.J. Greenshields and H.G. Weller. A unified formulation for continuum mechanics applied to fluid-structure interaction in flexible tubes. *International Journal for Numerical Methods in Engineering*, 64(12):1575–1593, 2005.

[64] P.M. Gresho and R.L. Sani. *Incompressible Flow and the Finite Element Method, Isothermal Laminar Flow*. Incompressible Flow and the Finite Element Method. John Wiley & Sons, 2000. ISBN 9780471492504.

[65] J.L. Guermond, P. Minev, and J. Shen. An overview of projection methods for incompressible flows. *Computer Methods in Applied Mechanics and Engineering*, 195(44-47):6011–6045, 2006.

[66] O. Guerri, A. Hamdouni, and A. Sakout. Fluid structure interaction of wind turbine airfoils. *Wind Engineering*, 32(6):539–557, 2008.

[67] GWEC. Global wind report - annual market update 2013. Technical report, Global Wind Energy Council, 2014.

[68] C. Habchi, S. Russeil, D. Bougeard, J.-L. Harion, T. Lemenand, A. Ghanem, D.D. Valle, and H. Peerhossaini. Partitioned solver for strongly coupled fluid-structure interaction. *Computers and Fluids*, 71:306–319, 2013.

[69] M.O.L. Hansen and H. Aagaard Madsen. Review paper on wind turbine aerodynamics. *Journal of Fluids Engineering, Transactions of the ASME*, 133(11), 2011.

[70] M.O.L. Hansen, J.N. Sørensen, S. Voutsinas, N. Sørensen, and H.Aa. Madsen. State of the art in wind turbine aerodynamics and aeroelasticity. *Progress in Aerospace Sciences*, 42(4):285–330, 2006.

[71] M. Heil, A.L. Hazel, and J. Boyle. Solvers for large-displacement fluid-structure interaction problems: Segregated versus monolithic approaches. *Computational Mechanics*, 43(1):91–101, 2008.

[72] K. Herfjord, T. Holmås, and K. Randa. A parallel approach for numerical solution of vortex induced vibrations of very long risers. In S. Idelsohn, E. Oñate, and E. Dvorkin, editors, *Computational Mechanics - New Trends and Applications*. CIMNE, 1998.

[73] K. Herfjord, S. O. Drange, and T. Kvamsdal. Assessment of vortex-induced vibrations on deepwater risers by considering fluid-structure interaction. *Journal of Offshore Mechanics and Arctic Engineering*, 121(4):207–212, November 1999.

[74] K. Herfjord, G. Olsen, T. Kvamsdal, and K. M. Okstad. Fluid–Structure Interaction in the case of Two Independent Cylinders in Vortex Induced Vibrations (VIV). *International Journal of Applied Mechanics and Engineering*, 7:65–83, 2002.

[75] M.A. Heroux, R.A. Bartlett, V.E. Howle, R.J. Hoekstra, J.J. Hu, T.G. Kolda, R.B. Lehoucq, K.R. Long, R.P. Pawlowski, E.T. Phipps, A.G. Salinger, H.K. Thornquist, R.S. Tuminaro, J.M. Willenbring, A. Williams, and K.S. Stanley. An overview of the Trilinos project. *ACM Transactions on Mathematical Software*, 31(3):397–423, 2005.

[76] M. R. Hestenes and E. Stiefel. Methods of Conjugate Gradients for Solving Linear Systems. *Journal of Research of the National Bureau of Standards*, 49:409–436, December 1952.

[77] J. Hoffman and C. Johnson. A new approach to computational turbulence modeling. *Computer Methods in Applied Mechanics and Engineering*, 195 (23-24):2865–2880, 2006.

[78] J. Hoffman and C. Johnson. *Computational Turbulent Incompressible Flow: Applied Mathematics Body and Soul*, volume Vol 4. Springer-Verlag Publishing, 2007.

[79] J. Hoffman, J. Jansson, R.V. de Abreu, N.C. Degirmenci, N. Jansson, K. Müller, M. Nazarov, and J.H. Spühler. Unicorn: Parallel adaptive finite element simulation of turbulent flow and fluid-structure interaction for deforming domains and complex geometry. *Computers and Fluids*, 80(1): 310–319, 2013.

[80] M.-C. Hsu and Y. Bazilevs. Fluid-structure interaction modeling of wind turbines: Simulating the full machine. *Computational Mechanics*, 50(6): 821–833, 2012.

[81] M.-C. Hsu, I. Akkerman, and Y. Bazilevs. High-performance computing of wind turbine aerodynamics using isogeometric analysis. *Computers and Fluids*, 49(1):93–100, 2011.

[82] M.-C. Hsu, I. Akkerman, and Y. Bazilevs. Wind turbine aerodynamics using ALE-VMS: Validation and the role of weakly enforced boundary conditions. *Computational Mechanics*, 50(4):499–511, 2012.

[83] M.-C. Hsu, I. Akkerman, and Y. Bazilevs. Finite element simulation of wind turbine aerodynamics: Validation study using NREL Phase VI experiment. *Wind Energy*, 17(3):461–481, 2014.

[84] B. Hübner, E. Walhorn, and D. Dinkler. A monolithic approach to fluid-structure interaction using space-time finite elements. *Computer Methods in Applied Mechanics and Engineering*, 193(23-26):2087–2104, 2004.

[85] T.J.R. Hughes, L. Mazzei, and K.E. Jansen. Large eddy simulation and the variational multiscale method. *Computing and Visualization in Science*, 3 (1-2):47–59, 2000.

[86] T.J.R. Hughes, J.A. Cottrell, and Y. Bazilevs. Isogeometric analysis: CAD, finite elements, NURBS, exact geometry and mesh refinement. *Computer Methods in Applied Mechanics and Engineering*, 194(39-41):4135–4195, 2005.

[87] D. Ishihara and S. Yoshimura. A monolithic approach for interaction of incompressible viscous fluid and an elastic body based on fluid pressure Poisson equation. *International Journal for Numerical Methods in Engineering*, 64(2):167–203, 2005.

[88] C. B. Jenssen and T. Kvamsdal. Computational methods for FSI-simulalations of slender bridges on high performance computers. In T. Kvamsdal, editor, *Computational Methods for Fluid-Structure Interactions*, pages 31–40. Tapir Publisher, Trondheim, 1999.

[89] W.P. Jones and B.E. Launder. The prediction of laminarization with a two-equation model of turbulence. *International Journal of Heat and Mass Transfer*, 15(2):301–314, 1972.

[90] W. Joppich and M. Kürschner. MpCCI - a tool for the simulation of coupled applications. *Concurrency Computation Practice and Experience*, 18(2): 183–192, 2006.

[91] R. Kamakoti and W. Shyy. Fluid-structure interaction for aeroelastic applications. *Progress in Aerospace Sciences*, 40(8):535–558, 2004.

[92] C. Kassiotis, A. Ibrahimbegovic, R. Niekamp, and H.G. Matthies. Nonlinear fluid-structure interaction problem. Part I: Implicit partitioned algorithm, nonlinear stability proof and validation examples. *Computational Mechanics*, 47(3):305–323, 2011.

[93] C. Kassiotis, A. Ibrahimbegovic, R. Niekamp, and H.G. Matthies. Nonlinear fluid-structure interaction problem. Part II: Space discretization, implementation aspects, nested parallelization and application examples. *Computational Mechanics*, 47(3):335–357, 2011.

[94] U. Küttler and W.A. Wall. Fixed-point fluid-structure interaction solvers with dynamic relaxation. *Computational Mechanics*, 43(1):61–72, 2008.

[95] T. Kvamsdal, C. B. Jenssen, K. M. Okstad, and J. Amundsen. Fluid-structure interactions for structural design. In T. Kvamsdal, editor, *Computational Methods for Fluid-Structure Interactions*, pages 211–238. Tapir Publisher, Trondheim, 1999.

[96] T. Kvamsdal, K. M. Okstad, K. Sørli, and P. Pegon. Two-level adaptive mesh movement algorithms for FSI-computations. In T. Kvamsdal, editor, *Computational Methods for Fluid-Structure Interactions*, pages 121–132. Tapir Publisher, Trondheim, 1999.

[97] H.P. Langtangen, K.-A. Mardal, and R. Winther. Numerical methods for incompressible viscous flow. *Advances in Water Resources*, 25(8-12):1125–1146, 2002.

[98] R.B. Langtry and F.R. Menter. Correlation-based transition modeling for unstructured parallelized computational fluid dynamics codes. *AIAA Journal*, 47(12):2894–2906, 2009.

[99] B.E. Launder and B.I. Sharma. Application of the energy-dissipation model of turbulence to the calculation of flow near a spinning disc. *Letters in Heat and Mass Transfer*, 1(2):131–137, 1974.

[100] B.E. Launder and D.B. Spalding. The numerical computation of turbulent flows. *Computer Methods in Applied Mechanics and Engineering*, 3(2): 269–289, 1974.

[101] P. Le Tallec and J. Mouro. Fluid structure interaction with large structural displacements. *Computer Methods in Applied Mechanics and Engineering*, 190(24-25):3039–3067, 2001.

[102] A. Logg, K.-A. Mardal, and G. N. Wells. *Automated Solution of Differential Equations by the Finite Element Method*. Springer, 2012. ISBN 978-3-642-23098-1.

[103] J.F. Manwell, J.G. McGowan, and A.L. Rogers. *Wind energy explained: Theory, design and application*. Wiley, Chichester, 2nd edition, 2009.

[104] H.G. Matthies and J. Steindorf. Partitioned but strongly coupled iteration schemes for nonlinear fluid-structure interaction. *Computers and Structures*, 80(27-30):1991–1999, 2002.

[105] S. Medida and J. Baeder. Application of the correlation-based $\gamma - Re_{\theta t}$ transition model to the Spalart-Allmaras turbulence model. In *Fluid Dynamics and Co-located Conferences*. American Institute of Aeronautics and Astronautics, June 2011.

[106] M. Mehl, M. Brenk, H.-J. Bungartz, K. Daubner, I.L. Muntean, and T. Neckel. An Eulerian approach for partitioned fluid-structure simulations on Cartesian grids. *Computational Mechanics*, 43(1):115–124, 2008.

[107] P.A. Mendes and F.A. Branco. Analysis of fluid-structure interaction by an arbitrary Lagrangian-Eulerian finite element formulation. *International Journal for Numerical Methods in Fluids*, 30(7):897–919, 1999.

[108] F.R. Menter. Two-equation eddy-viscosity turbulence models for engineering applications. *AIAA Journal*, 32(8):1598–1605, August 1994.

[109] F.R. Menter, R.B. Langtry, S.R. Likki, Y.B. Suzen, P.G. Huang, and S. Volker. A correlation-based transition model using local variables - Part I: Model formulation. *Journal of Turbomachinery*, 128(3):413–422, 2006.

[110] MHI Vestas. Vestas 8 MW wind turbine. `http://www.mhivestasoffshore.com/Products-and-services/The-Turbines/V164`, 2014. Accessed 18.12.2014.

[111] C. Michler, E.H. van Brummelen, and R. de Borst. An interface Newton-Krylov solver for fluid-structure interaction. *International Journal for Numerical Methods in Fluids*, 47(10-11):1189–1195, 2005.

[112] P.D. Minev. A stabilized incremental projection scheme for the incompressible Navier-Stokes equations. *International Journal for Numerical Methods in Fluids*, 36(4):441–464, 2001.

[113] H.J.P. Morand and R. Ohayon. *Fluid-Structure Interaction: Applied Numerical Methods*. Wiley-Masson Series Research in Applied Mathematics. Wiley, 1995. ISBN 9780471944591.

[114] National Renewable Energy Laboratory. NWTC Information Portal (FAST). `https://nwtc.nrel.gov/FAST`, 2014. Accessed 18.12.2014.

[115] OpenFOAM. OpenFOAM web page. `http://www.openfoam.com`, 2014. Accessed 18.12.2014.

[116] S. Piperno. Explicit/implicit fluid/structure staggered procedures with a structural predictor and fluid subcycling for 2D inviscid aeroelastic simulations. *International Journal for Numerical Methods in Fluids*, 25(10): 1207–1226, 1997.

[117] S. Piperno, C. Farhat, and B. Larrouturou. Partitioned procedures for the transient solution of coupled aroelastic problems Part I: Model problem, theory and two-dimensional application. *Computer Methods in Applied Mechanics and Engineering*, 124(1-2):79–112, 1995.

[118] A. Rasheed, R. Holdahl, T. Kvamsdal, and E. Åkervik. A comprehensive simulation methodology for fluid-structure interaction of offshore wind turbines. *Energy Procedia*, 53(0):135 – 145, 2014.

[119] Y. Saad. *Iterative Methods for Sparse Linear Systems*. Society for Industrial and Applied Mathematics, Philadelphia, PA, USA, 2nd edition, 2003. ISBN 0898715342.

[120] Y. Saad and M. Schultz. Gmres: A generalized minimal residual algorithm for solving nonsymmetric linear systems. *SIAM Journal on Scientific and Statistical Computing*, 7(3):856–869, 1986.

[121] P. Sagaut. *Large Eddy Simulation for Incompressible Flows: An Introduction*. Scientific Computation. Springer, 2006. ISBN 9783540263449.

[122] J. Sarrate, A. Huerta, and J. Donea. Arbitrary Lagrangian-Eulerian formulation for fluid-rigid body interaction. *Computer Methods in Applied Mechanics and Engineering*, 190(24-25):3171–3188, March 2001.

[123] M. Schäfer, M. Heck, and S. Yigit. An implicit partitioned method for the numerical simulation of fluid-structure interaction. In H.-J. Bungartz and M. Schäfer, editors, *Fluid-Structure Interaction*, volume 53 of *Lecture Notes in Computational Science and Engineering*, pages 171–194. Springer Berlin Heidelberg, 2006. ISBN 978-3-540-34595-4.

[124] J. G Schepers and J. Heijdra. Verification of european wind turbine design codes, VEWTDC - final report. Technical Report ECN-C-01-055, ECN, May 2002.

[125] F. G. Schmitt. About Boussinesq's turbulent viscosity hypothesis: Historical remarks and a direct evaluation of its validity. *Comptes Rendus Mécanique*, 335(9-10):617–627, October 2007.

[126] K.W. Schulz and T.S. Meling. Multi-strip numerical analysis for flexible riser response. In *Proceedings of OMAE04, the 23rd International Conference on Offshore Mechanics and Arctic Engineering*, volume 1 A, pages 379–384, 2004.

[127] Simis AS. Ashes web page. `http://www.ashes.no/`, 2014. Accessed 18.12.2014.

[128] B. Smith, P. Bjørstad, and W. Gropp. *Domain Decomposition: Parallel Multilevel Methods for Elliptic Partial Differential Equations*. Cambridge University Press, 2004. ISBN 9780521602860.

[129] N.N. Sørensen, A. Bechmann, and F. Zahle. 3D CFD computations of transitional flows using DES and a correlation based transition model. *Wind Energy*, 14(1):77–90, 2011.

[130] M. Souli and D.J. Benson. *Arbitrary Lagrangian Eulerian and Fluid-Structure Interaction: Numerical Simulation*. ISTE. Wiley, 2010. ISBN 9781848211315.

[131] P.R. Spalart. Detached-eddy simulation. *Annual Review of Fluid Mechanics*, 41:181–202, 2009.

[132] P.R. Spalart. Reflections on RANS modelling. *Notes on Numerical Fluid Mechanics and Multidisciplinary Design*, 111:7–24, 2010.

[133] P.R. Spalart and S.R. Allmaras. One-equation turbulence model for aerodynamic flows. *Recherche aerospatiale*, 1:5–21, 1994.

[134] P.R. Spalart, W.-H Jou, M. Stretlets, and S. R. Allmaras. Comments on the feasibility of LES for wings and on the hybrid RANS/LES approach. In *Advances in DNS/LES, Proceedings of the First AFOSR International Conference on DNS/LES*, 1997.

[135] K. Stein, T.E. Tezduyar, and R. Benney. Automatic mesh update with the solid-extension mesh moving technique. *Computer Methods in Applied Mechanics and Engineering*, 193(21-22):2019–2032, 2004.

[136] D.C. Sternel, M. Schäfer, M. Heck, and S. Yigit. Efficiency and accuracy of fluid-structure interaction simulations using an implicit partitioned approach. *Computational Mechanics*, 43(1):103–113, 2008.

[137] M. Strelets. Detached eddy simulation of massively separated flows. 2001.

[138] J. Sumner, C.S. Watters, and C. Masson. CFD in wind energy: The virtual, multiscale wind tunnel. *Energies*, 3(5):989–1013, 2010.

[139] N. Takashi. ALE finite element computations of fluid-structure interaction problems. *Computer Methods in Applied Mechanics and Engineering*, 112 (1-4):291–308, 1994.

[140] N. Takashi and T.J.R. Hughes. An arbitrary Lagrangian-Eulerian finite element method for interaction of fluid and a rigid body. *Computer Methods in Applied Mechanics and Engineering*, 95(1):115–138, 1992.

[141] R. Temam. Sur l'approximation de la solution des equations de navier-stokes par la methode des pas fractionnaires (ii). *Archive for Rational Mechanics and Analysis*, 33(5):377–385, 1969.

[142] S. Turek and J. Hron. Proposal for numerical benchmarking of fluid-structure interaction between an elastic object and laminar incompressible flow. Technical report, University of Dortmund, 2006.

[143] S. Turek, J. Hron, M. Madlik, M. Razzaq, H. Wobker, and J.F. Acker. Numerical simulation and benchmarking of a monolithic multigrid solver for fluid-structure interaction problems with application to hemodynamics. *Lecture Notes in Computational Science and Engineering*, 73 LNCSE:193–220, 2010.

[144] S. Turek, J. Hron, M. Razzaq, H. Wobker, and M. Schaefer. Numerical benchmarking of fluid-structure interaction: A comparison of different discretization and solution approaches. *Lecture Notes in Computational Science and Engineering*, 73 LNCSE:413–424, 2010.

[145] S. Türk, H. Spiegelberg, M. Schäfer, C. Tropea, and D. C. Sternel. Numerical investigation of an airfoil with self-adaptive camber. In *Proceedings of WCCM XI / ECCM V / ECFD VI*, 2014.

[146] J.-M. Vaassen, P. De Vincenzo, C. Hirsch, and B. Leonard. Strong coupling algorithm to solve fluid-structure-interaction problems with a staggered approach. In *ESA Special Publication*, volume 692 of *ESA Special Publication*, August 2011.

[147] K. Valen-Sendstad, A. Logg, K.-A. Mardal, H. Narayanan, and M. Mortensen. *A Comparison of Some Common Finite Element Schemes for the Incompressible Navier-Stokes Equations*, volume 84 of *Lecture Notes in Computational Science and Engineering*, chapter 21, pages 395–418. Springer, 2012. ISBN 978-3-642-23098-1.

[148] E.H. van Brummelen. Added mass effects of compressible and incompressible flows in fluid-structure interaction. *Journal of Applied Mechanics, Transactions ASME*, 76(2):1–7, 2009.

[149] E.H. van Brummelen. Partitioned iterative solution methods for fluid-structure interaction. *International Journal for Numerical Methods in Fluids*, 65(1-3):3–27, 2011.

[150] E. Walhorn, A. Kölke, B. Hübner, and D. Dinkler. Fluid-structure coupling within a monolithic model involving free surface flows. *Computers and Structures*, 83(25-26):2100–2111, 2005.

[151] W. A. Wall and E. Ramm. Fluid-structure interaction based upon a stabilized (ALE) finite element method. In S.R. Idelsohn, E. Oñate, and E.N. Dvorkin, editors, *Computational Mechanics - New Trends and Applications*, Barcelona, Spain, 1998. CIMNE.

[152] W.A. Wall, D.P. Mok, and E. Ramm. Iterative substructering schemes for fluid structure interaction. *Lecture Notes in Applied and Computational Mechanics*, 12:349–360, 2003.

[153] W.A. Wall, S. Genkinger, and E. Ramm. A strong coupling partitioned approach for fluid-structure interaction with free surfaces. *Computers and Fluids*, 36(1):169–183, 2007.

[154] D. C. Wilcox. Formulation of the $k - \omega$ turbulence model revisited. *AIAA Journal*, 46(11):2823–2838, November 2008. ISSN 0001-1452. doi: 10. 2514/1.36541.

[155] David C. Wilcox. *Turbulence modeling for CFD*. DCW Industries, Inc., third edition, November 2006.

# Paper I

# Paper I

## Simulation of airflow past a 2D NACA0015 airfoil using an isogeometric incompressible Navier-Stokes solver with the Spalart-Allmaras turbulence model

Knut Nordanger, Runar Holdahl, Arne Morten Kvarving, Trond Kvamsdal and Adil Rasheed

# Paper I

# Simulation of airflow past a 2D NACA0015 airfoil using an isogeometric incompressible Navier-Stokes solver with the Spalart-Allmaras turbulence model

Knut Nordanger[a,*], Runar Holdahl[b], Trond Kvamsdal[a,b], Arne Morten Kvarving[b], Adil Rasheed[b]

[a]*Department of Mathematical Sciences, Norwegian University of Science and Technology, NO-7491 Trondheim, Norway*
[b]*SINTEF ICT, Department of Applied Mathematics, Postboks 4760 Sluppen, NO-7465 Trondheim, Norway*

## Abstract

The work presented in this paper concerns the efforts of conducting a computational fluid dynamics (CFD) simulation of air flow past a fixed 2D NACA0015 airfoil at high Reynolds number ($Re = 2.5 \times 10^6$) using an isogeometric finite element methodology with linear, quadratic and cubic spline elements. Flow simulations at such high Reynolds numbers require turbulence models or very high resolution. The present work employs the Spalart-Allmaras turbulence model combined with a Navier-Stokes solver based on a Chorin projection method, the first development of its kind in an isogeometric finite element framework. The obtained results from the simulations are compared with two sets of experimental results available in the literature.

*Keywords:* Isogeometric analysis, NACA0015 airfoil, Chorin projection method, Spalart-Allmaras

## 1. Introduction

Wind power has gained political momentum in recent years owing to its relatively lesser environmental conflicts, greater efficiency and favorable wind conditions. The European Union (EU), for example, has a slogan $20 - 20 - 20$, which implies that by 2020 20 % of the EU's energy should come from renewable sources, greenhouse gas emissions should decrease by 20 % and energy efficiency should increase by 20 %. By that time it is expected that 40 GW of the offshore wind power capacity would have already been installed [1]. In 2013 alone, around 11100 MW of wind power infrastructures, both onshore and offshore, were installed in the EU [2]. Meanwhile, an increasing number of wind turbines have been and will be installed in both the United States (US) and China.

---

*Corresponding author
*Email addresses:* knut.nordanger@math.ntnu.no (Knut Nordanger), runar.holdahl@sintef.no (Runar Holdahl), trond.kvamsdal@math.ntnu.no (Trond Kvamsdal), arne.morten.kvarving@sintef.no (Arne Morten Kvarving), adil.rasheed@sintef.no (Adil Rasheed)

Offshore wind energy compared to its onshore counterpart appears more attractive due to its lesser visual impact and lesser issues related to land acquisition. Relatively more convenient accessibility to open sea allows for the installation of larger and larger turbines capable of producing much more power resulting in far lesser number of turbines per wind farm to produce the same amount of power. However, the large size of the turbines and the harsh meteorological conditions offshore come with new design challenges, not appropriately addressed by the traditional engineering methods/tools [3]. One such problem is related to the dynamic loading and unloading of turbine blades and structures. Fluid-structure interaction (FSI) simulation tools are being developed to address the issue and have already become a reality for wind turbines ([4] and [5]) and bridges [6, 7, 8, 9]. However, such detailed 3D simulations are still computationally demanding and not suitable for performing sensitivity analysis for optimum blade design.

To strike a balance between accuracy and computational efficiency, inspiration can be taken from a strip theory approach which was used to simulate vortex-induced vibration of offshore risers and submerged pipelines in [8], [10] and [11]. In the approach, a series of 2D computational fluid dynamics (CFD) simulations were conducted to predict the flow characteristics around the riser and then the forces were transferred to the structure solver for finite element analysis using non-linear beam elements. The reliability of this method depends on the accuracy of the 2D simulations and hence as a starting point we investigate an approach based on isogeometric analysis which emerged in 2005 [12], and offers integration of analysis and CAD geometry [13] through the use of the same basis functions. This results in advantages such as better accuracy per degree-of-freedom and exact geometric representation.

Wind turbines have for many years been an active research field, and in recent years isogeometric wind turbine simulation results have been published by Bazilevs and others [14, 15, 4]. However, little has been published, barring some work like [16] and recently [17], on flow past a fixed airfoil. Moreover, most of the simulations in a wind engineering context using isogeometric analysis have been limited to Variational Multiscale (VMS) approach for modeling turbulence. Although the approach has a more sound basis for simulating turbulent flows, their applicability is somewhat constrained by their computationally expensive nature, i.e. need for doing 3D flow simulations.

A remedy in order to enable the use of 2D flow simulations is to use Reynolds-Averaged Navier-Stokes (RANS) equations with one-equation Spalart-Allmaras (SA) turbulence closure which has been specially developed and optimized for simulating 2D flow around airfoils [18]. Furthermore, based on a study by Valen-Sendstad et al. ([19]), that investigated the performance of six different solvers for incompressible flow, we have chosen to use a Chorin projection method (incremental pressure correction) as this was found to be the most efficient and accurate. This is further enhanced by applying Minev stabilization for equal order elements [20]. We believe that the first step towards the use of strip theory is to develop and demonstrate a CFD solver based on splines (to improve geometric representation), with Chorin projection method (for efficiency) and Spalart Allmaras turbulence model (optimized for 2D flow around airfoils). The main contribution of this work is to demonstrate the seamless integration of geometry modeling, meshing and analysis tools using linear, quadratic and cubic spline elements and the achievable accuracy to simulate flow around a two-

2

dimensional NACA0015 airfoil.

## 2. Theory

A code intended for a task like sensitivity analysis / shape optimization requires it to be convenient to use and easy to make several runs by changing the input parameters. This requires a seamless integration of the geometry modeler, mesh generator and CFD solver. In this section we present a description of the NACA airfoils, governing equations of flow and turbulence modeling, their discretization, implementation of boundary conditions as well as equations used to compute the aerodynamic coefficients presented in the result section.

### 2.1. Introduction to 4-digit NACA airfoil

The family of symmetric NACA airfoils is denoted by NACA00XX where the last two digits give the ratio between the maximum thickness of the airfoil $t$ and the chord length $c$. The shape of all NACA00XX airfoils is given by the analytical formula [21]

$$y_t = 5tc \left[ 0.2969 \sqrt{\frac{x}{c}} - 0.1260 \left( \frac{x}{c} \right) - 0.3516 \left( \frac{x}{c} \right)^2 + 0.2843 \left( \frac{x}{c} \right)^3 - 0.1015 \left( \frac{x}{c} \right)^4 \right]$$
(1)

where $y_t$ is the distance from the centerline, $t$ the maximum thickness from the centerline, $c$ the chord length and $x$ the position along the chord from 0 to $c$. In order to have a closed curve and thickness $y_t = 0$ at $x = c$ one of the coefficients has to be modified as they do not sum to zero. We choose to modify the last coefficient (i.e. the coefficient in front of the highest order term) to $-0.1036$ as this gives the smallest perturbation of the surface curve. Sometimes the blade profile is given in the form of coordinate data at discrete points along the surface. No matter how the data is obtained it is used to get a spline representation following the approach described in Section 2.5.3.

### 2.2. Fluid solver

This section describes the fluid solver through the governing equations, the isogeometric finite element approximation, the projection method employed and the boundary conditions.

### 2.2.1. Governing equations

Viscous airflow at low Mach numbers is mathematically described by the incompressible Navier-Stokes equations. These equations can be written as

$$\frac{\partial \boldsymbol{u}}{\partial t} + \rho \left( \boldsymbol{u} \cdot \nabla \right) \boldsymbol{u} - \nabla \cdot \boldsymbol{\sigma} \left( \boldsymbol{u}, p \right) = \rho \boldsymbol{f} \quad \text{in } \Omega$$

$$\nabla \cdot \boldsymbol{u} = 0 \quad \text{in } \Omega.$$

Here, $\Omega \in \mathbb{R}^d$, $d = 2, 3$, is a suitable, sufficiently regular and open domain, $\rho$ is the constant fluid density, $p$ is the pressure, $\boldsymbol{u}$ is the fluid velocity vector and $\boldsymbol{f}$ is a volumetric body force. The Cauchy stress tensor can be written as

$$\boldsymbol{\sigma}(\boldsymbol{u}, p) = -p\boldsymbol{I} + 2\mu\boldsymbol{\epsilon}(\boldsymbol{u}),$$

where $\boldsymbol{I}$ is the identity tensor and $\mu$ is the dynamic viscosity and the strain rate $\boldsymbol{\epsilon}$ is defined as

$$\boldsymbol{\epsilon}(\boldsymbol{u}) = \frac{1}{2} \left( \nabla \boldsymbol{u} + (\nabla \boldsymbol{u})^T \right).$$

Furthermore, we define $\partial\Omega = \Gamma = \Gamma_D \cup \Gamma_N \cup \Gamma_M$ where $\Gamma_D$ are the boundaries with Dirichlet conditions, $\Gamma_N$ the boundaries with Neumann conditions $\Gamma_M$ the boundaries with mixed conditions. Mixed boundary conditions are used in situations where the normal velocity components are given, usually zero, together with the tangential stresses can model symmetry planes and slip or friction conditions.

The variational formulation is expressed as: Find $(\boldsymbol{u}, p) \in \boldsymbol{U} \times Q$ such that

$$\left( \rho \frac{\partial \boldsymbol{u}}{\partial t}, \boldsymbol{v} \right) + c(\boldsymbol{u}; \boldsymbol{u}, \boldsymbol{v}) + b(p, \boldsymbol{v}) + a(\boldsymbol{u}, \boldsymbol{u}) + b(q, \boldsymbol{u}) = f(\boldsymbol{v}) \quad (\boldsymbol{v}, q) \in \boldsymbol{V} \times Q. \tag{2}$$

Here, we have defined the spaces

$$\boldsymbol{U} = \boldsymbol{H}^1_{\Gamma_D, \Gamma_M^\perp}(\Omega) = \left\{ \boldsymbol{v} \in \boldsymbol{H}^1(\Omega) \mid \boldsymbol{v} = \boldsymbol{u_D} \text{ on } \Gamma_D \text{ and } \boldsymbol{v} \cdot \boldsymbol{n} = u_\perp \text{ on } \Gamma_M \right\}$$
$$\boldsymbol{V} = \boldsymbol{H}^1_{\Gamma_D, \Gamma_M^\perp;0}(\Omega) = \left\{ \boldsymbol{v} \in \boldsymbol{H}^1(\Omega) \mid \boldsymbol{v} = 0 \text{ on } \Gamma_D \text{ and } \boldsymbol{v} \cdot \boldsymbol{n} = 0 \text{ on } \Gamma_M \right\}$$
$$Q = L^2(\Omega),$$

where $\boldsymbol{u_D}$ and $u_\perp$ both are given functions and $\boldsymbol{n}$ is the unit outer normal on $\Gamma$, and the forms

$$a(\boldsymbol{u}, \boldsymbol{v}) = 2 \int_\Omega \mu \boldsymbol{\epsilon}(\boldsymbol{u}) : \boldsymbol{\epsilon}(\boldsymbol{v}) \, \mathrm{d}\boldsymbol{x}$$
$$b(q, \boldsymbol{v}) = - \int_\Omega (\nabla \cdot \boldsymbol{v}) q \, \mathrm{d}\boldsymbol{x}$$
$$c(\boldsymbol{w}; \boldsymbol{u}, \boldsymbol{v}) = \int_\Omega \rho(\boldsymbol{w} \cdot \nabla) \boldsymbol{u} \cdot \boldsymbol{v} \, \mathrm{d}\boldsymbol{x}$$
$$f(\boldsymbol{v}) = \int_\Omega \rho \boldsymbol{f} \cdot \boldsymbol{v} \, \mathrm{d}\boldsymbol{x} + \int_{\Gamma_N} \boldsymbol{t} \cdot \boldsymbol{v} \, \mathrm{d}\boldsymbol{s},$$

where $\boldsymbol{t} = \boldsymbol{\sigma} \cdot \boldsymbol{n}$ is the traction vector on $\Gamma$. Here $\boldsymbol{U}$ and $\boldsymbol{V}$ are the velocity trial and test function spaces, respectively, whereas $Q$ is the corresponding function spaces for the trial and test pressure variables. The velocity trial function space $\boldsymbol{H}^1_{\Gamma_D, \Gamma_M^\perp}(\Omega)$ has the same regularity as the classical Hilbert space $\boldsymbol{H}^1(\Omega)$ inside the domain $\Omega$, but restricted to fulfill the imposed Dirichlet conditions along $\Gamma_D$ as well as mixed boundary conditions, see Section 2.2.4 along $\Gamma_M^\perp$. The velocity test function space $\boldsymbol{H}^1_{\Gamma_D, \Gamma_M^\perp;0}(\Omega)$ is similar to the velocity trial space, but have homogeneous Dirichlet conditions along $\Gamma_D$ and $\Gamma_M^\perp$.

### 2.2.2. Isogeometric finite element approximation

The isogeometric finite element method approximates the solution by using a spline basis of polynomial order $p$ and regularity $C^{p-1}$, whereas $C^0$ Lagrange polynomials of low order (typical $p = 1$ or $p = 2$) are used in traditional finite

element formulations. Our approach is based on a conforming finite element approximation, i.e.

$$\boldsymbol{U}_h \subset \boldsymbol{U}, \quad \boldsymbol{V}_h \subset \boldsymbol{V}, \quad Q_h \subset Q.$$

The discrete approximation spaces $\boldsymbol{U}_h$, $\boldsymbol{V}_h$, $Q_h$ are chosen as the isogeometric finite element spaces. This gives the semi-discrete formulation of the variational problem stated in Eq. (2): Find $(\boldsymbol{u}_h, p_h) \in \boldsymbol{U}_h \times Q_h$ such that

$$\left( \rho \frac{\partial \boldsymbol{u}_h}{\partial t}, \boldsymbol{v}_h \right) + c(\boldsymbol{u}_h; \boldsymbol{u}_h, \boldsymbol{v}_h) + a(\boldsymbol{u}_h, \boldsymbol{u}_h) + b(p, \boldsymbol{v}_h) + b(q, \boldsymbol{u}_h) = f(\boldsymbol{v}_h)$$

for all $(\boldsymbol{v}_h, q_h) \in \boldsymbol{V}_h \times Q_h$.

Herein, we have developed a block-structured B-spline isogeometric finite element approximation of the Navier-Stokes equations described above. To construct a B-spline basis for a domain $\Omega$ which is subdivided into a number of patches (a patch is equivalent to a block) $\Omega_e$ such that $\Omega = \cup_{e=1}^{N} \Omega_e$ we associate for each patch a knot-vector in each coordinate direction

$$\Xi_k^e = \left\{ \xi_{1,k}^e, \xi_{2,k}^e, \ldots, \xi_{n_k^e + p_k^e + 1}^e \right\}$$

for $k = 1, \ldots, d$. The B-spline basis for patch $\Omega_e$ on the parametric domain $\hat{\Omega} = (0,1)^d$ is written as $\hat{\boldsymbol{\mathcal{S}}}_{\boldsymbol{\alpha}^e}^{\boldsymbol{p}^e}$ where the multi-indices $\boldsymbol{\alpha}^e = (\alpha_1^e, \ldots, \alpha_d^e)$ and $\boldsymbol{p}^e = (p_1^e, \ldots, p_d^e)$ denote the regularity and order for the basis in each coordinate direction, respectively. The corresponding basis for the physical domain $\Omega_e$ can be expressed using the coordinate mapping $\phi_e : \hat{\Omega} \to \Omega_e$ as

$$\boldsymbol{\mathcal{S}}_{\boldsymbol{\alpha}^e}^{\boldsymbol{p}^e} = \left\{ v_h \mid v_h \circ \boldsymbol{\phi}_e \in \hat{\boldsymbol{\mathcal{S}}}_{\boldsymbol{\alpha}^e}^{\boldsymbol{p}^e} \right\}.$$

If the variational formulation allows a discontinuous approximation the spline finite element basis for the domain $\Omega$ can be defined as

$$\boldsymbol{\mathcal{S}}_h = \left\{ v_h \mid v_{h|\Omega_e} \in \boldsymbol{\mathcal{S}}_{\boldsymbol{\alpha}^e}^{\boldsymbol{p}^e} \right\}.$$

If we assume that the knot-vectors and geometrical mapping $\boldsymbol{\phi}_e$ for all the patches are consistent on common edges and faces we can define a continuous basis

$$\boldsymbol{\mathcal{S}_h} = \left\{ v_h \in C(\Omega) \mid v_{h|\Omega_e} \in \boldsymbol{\mathcal{S}}_{\boldsymbol{\alpha}^e}^{\boldsymbol{p}^e} \right\}.$$

### 2.2.3. Projection method

In order to solve the mixed variational problem given above the following inf-sup condition

$$\inf_{q_h \in Q_h, q_h \neq 0} \sup_{\boldsymbol{v}_h \in \boldsymbol{V}_h, \boldsymbol{v}_h \neq 0} \frac{b(q_h, \boldsymbol{v}_h)}{\|q_h\|_{L^2(\Omega)} \|\boldsymbol{v}_h\|_{\boldsymbol{H}^1(\Omega)}} \geq C > 0.$$

needs to be satisfied in order to avoid spurious pressure modes [22]. This imposes restrictions on the choices of $\boldsymbol{V}_h$ and $Q_h$.

Traditionally a mixed finite element method with different approximation spaces for pressure and velocity is required. In this work we use a pressure

correction projection scheme which allows for equal order approximation of the velocity and pressure. This is based on the work pioneered by Chorin [23] and Temam [24] in the late 1960s. However, the present implementation is inspired by the review article [25] which also accommodates significant progress regarding theoretical and implementational issues for projection schemes in recent years, and the work on pressure stabilization by Minev as presented in [20].

For the chosen projection method one only needs to solve decoupled problems of elliptic equations at each time step instead of the full coupling of the velocity and pressure [25]. Thus standard Krylov subspace methods like the conjugate gradient (CG) method and Generalized Minimal RESidual method (GMRES) can be used to solve the linear systems. For these methods we also can employ efficient preconditioners. Drawbacks of the projection methods include a inherited splitting error and extra numerical boundary conditions for the pressure. This reduces the convergence order of the numerical approximation.

In order to avoid the inconsistent pressure boundary condition present in many splitting schemes one may choose a rotational formulation for the incremental pressure correction scheme as proposed in [26]. The resulting splitting error is now only due to an inaccurate slip condition imposed on the velocity. The rotational form of the Chorin splitting scheme is of order 2 for the velocity and order 3/2 for the pressure, both in the $L^2$-norm, [27]. However, in some of our numerical tests we observed pressure oscillations when we used equal order approximation. Thus, in order to get a stable solution with our equal order approximation we herein chose to employ Minev stabilization as given in [20] to avoid node-to-node pressure oscillations.

The standard incremental pressure correction scheme is given by

1. Velocity prediction step

$$\frac{\rho}{2\Delta t}\left(3\tilde{\boldsymbol{u}}^{n+1} - 4\boldsymbol{u}^n + \boldsymbol{u}^{n-1}\right) + \rho\left(2\boldsymbol{u}^n - \boldsymbol{u}^{n-1}\right)\cdot\nabla\tilde{\boldsymbol{u}}^{n+1}$$
$$-\nabla\cdot\boldsymbol{\sigma}\left(\tilde{\boldsymbol{u}}^{n+1}, p^n\right) = \rho\boldsymbol{f}^{n+1},$$
$$\tilde{\boldsymbol{u}}^{n+1} = 0 \text{ on } \Gamma.$$

2. Pressure correction step

$$\frac{\rho}{2\Delta t}\left(3\boldsymbol{u}^{n+1} - 3\tilde{\boldsymbol{u}}^{n+1}\right) + \nabla\left(p^{n+1} - p^n\right) = 0,$$
$$\nabla\cdot\boldsymbol{u}^{n+1} = 0,$$
$$\boldsymbol{u}^{n+1}\cdot\boldsymbol{n} = 0 \text{ on } \Gamma.$$

However, to get a stable solution without pressure oscillations for an equal order approximation Minev [20] modified the pressure correction step and solved it in two successive steps

2.a Stabilized pressure correction (Galerkin formulation)

$$\left(\nabla\left[(1+\hat{\sigma})p^{n+1} - p^n\right], \nabla q\right) = -\frac{3}{2}\left(\nabla\cdot\tilde{\boldsymbol{u}}^{n+1}, q\right)$$
$$+ \hat{\sigma}\left(\nabla\cdot(-2\boldsymbol{u}^n + \frac{1}{2}\boldsymbol{u}^{n-1}), q\right)$$
$$- \frac{\hat{\sigma}}{2}\int_{\partial\Omega}\left(3\tilde{\boldsymbol{u}}^{n+1} - 4\tilde{\boldsymbol{u}}^n + \boldsymbol{u}^{n-1}\right)\cdot\boldsymbol{n}q\,\mathrm{d}s \quad q \in Q_h.$$

6

Here, $\hat{\sigma}$ is the stabilization parameter which is set equal to the time step in all simulations.

2.b Velocity correction

$$\frac{3}{2}\left(\boldsymbol{u}^{n+1} + \tilde{\boldsymbol{u}}^{n+1}\right) + \nabla\left(p^{n+1} - p^n\right) = 0$$

with boundary conditions as given in the problem formulation.

To summarize: Our algorithm implemented in IFEM is as follows:

1. Velocity prediction step
   Find $\tilde{\boldsymbol{u}}^{n+1}$ using the velocities $\boldsymbol{u}^n$ and $\boldsymbol{u}^{n-1}$ and the pressure $p^n$ computed at earlier time steps.

2.a Stabilized pressure correction (Galerkin formulation)
   Find $p^{n+1}$ using the predicted velocity $\tilde{\boldsymbol{u}}^{n+1}$ and the velocities $\boldsymbol{u}^n$, $\boldsymbol{u}^{n-1}$ and the pressure $p^n$ computed at earlier time steps.

2.b Velocity correction
   Find $\boldsymbol{u}^{n+1}$ using the predicted velocity $\tilde{\boldsymbol{u}}^{n+1}$, the updated pressure $p^{n+1}$ and the pressure $p^n$ computed at the previous time step.

The standard incremental pressure correction scheme is of order 2 for the velocity and order 1 for the pressure, both in the $L^2$-norm, [25]. As stated in [20], this is not changed when employing Minev stabilization.

**Remark**

The Pressure Poisson Equation (PPE) in Step 2.a implies that the proper discrete space $Q_h$ for the pressure trial and test functions has to fulfill $Q_h \subset L^2(\Omega) \cap H^1(\Omega)$. Furthermore, in PPE we employ a homogeneous Dirichlet condition for the pressure at the outflow boundary and homogeneous Neumann conditions, i.e. $\nabla p^{n+1} \cdot \boldsymbol{n}$ along the other boundaries.

*2.2.4. Boundary conditions*

Several boundary conditions can be applied for the Navier-Stokes equations. We assume that $\Gamma \subset \partial\Omega$ is a subset of the boundary of the domain. The Dirichlet and Neumann conditions can be written as

$$\boldsymbol{u} = \boldsymbol{g} \text{ on } \Gamma \text{ (Dirichlet conditions)}$$
$$\boldsymbol{\sigma} \cdot \boldsymbol{n} = \boldsymbol{h} \text{ on } \Gamma \text{ (Neumann conditions)},$$

where $\boldsymbol{g} = \boldsymbol{g}(\boldsymbol{x}, t)$ and $\boldsymbol{h} = \boldsymbol{h}(x, t)$ are given functions and $\boldsymbol{n}$ denotes the unit outer normal vector on $\partial\Omega$. Since only the gradient of the pressure is present in the Navier-Stokes equations and the Dirichlet condition does not involve any pressure information, the pressure can only be determined up to a constant if a Neumann condition is prescribed everywhere on the boundary. To fix the pressure level and have a well-defined problem a homogeneous pressure condition can be imposed on the outflow boundary. Furthermore, from the continuity condition we derive the following compatibility condition

$$\int_\Omega \nabla \cdot \boldsymbol{u} \, \mathrm{d}x = \int_{\partial\Omega} \boldsymbol{u} \cdot \boldsymbol{n} \, \mathrm{d}s = \int_{\partial\Omega} \boldsymbol{g} \cdot \boldsymbol{n} \, \mathrm{d}s = 0,$$

i.e. the boundary condition must impose a zero mean flux on the boundary to satisfy mass conservation.

We now assume that the boundary $\Gamma$ can be decomposed into three disjoint segments $\partial\Omega = \partial\Omega_{\text{in}} \cup \partial\Omega_{\text{out}} \cup \partial\Omega_{\text{c}}$ with

$$\partial\Omega_{\text{in}} = \{\boldsymbol{x} \in \Gamma \mid \boldsymbol{u} \cdot \boldsymbol{n} < 0\}, \quad \text{(inflow boundary)}$$
$$\partial\Omega_{\text{out}} = \{\boldsymbol{x} \in \Gamma \mid \boldsymbol{u} \cdot \boldsymbol{n} > 0\}, \quad \text{(outflow boundary)}$$
$$\partial\Omega_{\text{c}} = \{\boldsymbol{x} \in \Gamma \mid \boldsymbol{u} \cdot \boldsymbol{n} = 0\}, \quad \text{(characteristic boundary)}$$

On the inflow part of the boundary, i.e. on $\partial\Omega_{\text{in}}$, it is most natural to impose a Dirichlet condition. On outlet boundaries, i.e. on $\partial\Omega_{\text{out}}$, the Neumann condition is the preferred choice.

Mixed boundary conditions are also possible for the Navier-Stokes equations. A slip boundary condition can be written as

$$\boldsymbol{u} \cdot \boldsymbol{n} = 0 \text{ on } \Gamma,$$
$$\boldsymbol{n} \cdot \boldsymbol{\sigma} \cdot (\boldsymbol{I} - \boldsymbol{n} \otimes \boldsymbol{n}) = \boldsymbol{h} \text{ on } \Gamma,$$

where $\boldsymbol{I} - \boldsymbol{n} \otimes \boldsymbol{n}$ span the tangent plane to the boundary $\partial\Omega$ in $\mathbb{R}^d$. This corresponds to a Dirichlet condition for the normal direction and a Neumann condition in the tangential plane.

### 2.3. Turbulence modeling

High Reynolds number flows are dominated by turbulence which can be fully resolved using Direct Numerical Simulation (DNS) or partially resolved using Large Eddy Simulation (LES). In LES the larger scales in the flow are resolved while the smaller scales are assumed to be isotropic and modeled using different kinds of subgrid scale parametrization. However, the computationally expensive nature of DNS and LES prohibits their usage as a design tool. It is one of the reason that RANS models are still widely used. In the RANS model turbulence is not resolved but modeled. The mesh resolution and quality requirements for this class of models are also less stringent than the ones required in DNS or LES. In this work we employ the Spalart-Allmaras turbulence model [18] which has been optimized to simulate 2D flow around aerodynamically shaped bodies like an airfoil.

### 2.3.1. The Spalart–Allmaras turbulence model

The Spalart-Allmaras turbulence model is a one-equation model for a modified turbulent kinematic viscosity $\tilde{\nu}$ [18]. We employ the standard model presented in [18] along with the negative Spalart-Allmaras model presented in [28]. The formulation of the model is the transport equation

$$\frac{\mathrm{D}\tilde{\nu}}{\mathrm{D}t} = P - D + \frac{1}{\sigma} \left[ \nabla \cdot ((\nu + \tilde{\nu})\nabla\tilde{\nu}) + c_{b2} (\nabla\tilde{\nu})^2 \right],$$

where $\nu = \mu/\rho$ is the laminar kinematic viscosity, $\boldsymbol{u}$ is the fluid velocity and $d$ is the distance from a given point to the closest solid wall. Furthermore, the production and wall destruction terms read

$$P = c_{b1}(1 - f_{t2})\tilde{S}\tilde{\nu}, \qquad D = \left(c_{w1}f_w - \frac{c_{b1}}{\kappa^2}f_{t2}\right)\left[\frac{\tilde{\nu}}{d}\right]^2.$$

The laminar suppression term $f_{t2}$ is defined as

$$f_{t2} = c_{t3} \exp\left(-c_{t4}\chi^2\right),$$

with $c_{t3} = 1.2$ and $c_{t4} = 0.5$. From the modified viscosity $\tilde{\nu}$ the eddy viscosity can be computed as

$$\nu_t = \tilde{\nu} f_{v1}, \quad f_{v1} = \frac{\chi^3}{\chi^3 + c_{v1}^3}, \quad \chi \equiv \frac{\tilde{\nu}}{\nu}.$$

Modifications of the original model for the modified vorticity were published in [28]. The modified vorticity $\tilde{S}$ is now given by

$$\overline{S} = \frac{\tilde{\nu}}{\kappa^2 \cdot d^2} f_{v2}, \quad f_{v2} = 1 - \frac{\chi}{1 + \chi f_{v1}},$$

where $S$ represents the magnitude of the vorticity and $d$ the distance to the closest wall, and

$$\tilde{S} = \begin{cases} S + \overline{S} & : \overline{S} \geq -c_{v2}S \\ S + \frac{S\left(c_{v2}^2 S + c_{v3}\overline{S}\right)}{(c_{v3} - 2c_{v2})S - \overline{S}} & : \overline{S} < -c_{v2}S \end{cases}$$

with $c_{v2} = 0.7$ and $c_{v3} = 0.9$. The new modified vorticity $\tilde{S}$ does not have the possibility of becoming negative and thus avoids a possible problem of disrupting other Spalart-Allmaras functions. Furthermore we have for the destruction term

$$f_w = g \left[\frac{1 + c_{w3}^6}{g^6 + c_{w3}^3}\right]^{1/6}$$

$$g = r + c_{w2}(r^6 - r)$$

$$r = \frac{\tilde{\nu}}{\tilde{S}\kappa^2 d^2}.$$

In the original work [18] the following values are given for the other constants appearing in the model

$$c_{b1} = 0.1355, \quad c_{b_2} = 0.622, \quad c_{w_2} = 0.3, \quad c_{w_3} = 2,$$
$$\sigma_{\tilde{\nu}} = 2/3, \quad c_{\tilde{v}_1} = 7.1, \quad k = 0.41.$$

However, in cases with under-resolved grids and for some transient states, the produced $\tilde{\nu}$ solution is negative. A typical choice is then to clip the negative $\tilde{\nu}$ value, but we employ the negative Spalart-Allmaras model, presented in [28], which reads

$$\frac{D\tilde{\nu}}{Dt} = P_n - D_n + \frac{1}{\sigma}\nabla \cdot \left[(\nu + \tilde{\nu}f_n)\nabla\tilde{\nu}\right] + \frac{c_{b2}}{\sigma}\left(\nabla\tilde{\nu}\right)^2,$$

where $P_n$ is the production, $D_n$ is the wall destruction and $f_n(\chi)$ is diffusion coefficient modification. The diffusion coefficient modification is given as

$$f_n = \frac{c_{n1} + \chi^3}{c_{n1} - \chi^3},$$

where $c_{n1} = 16$. Furthermore we have

$$P_n = c_{b1}(1 - c_{t3})S\tilde{\nu}, \qquad D_n = -c_{w1}\left[\frac{\nu}{d}\right]^2,$$

where $S$ is the vorticity. The negative model always produces zero eddy viscosity, $\nu_t$.

### 2.3.2. Numerical discretization of the Spalart–Allmaras turbulence model

The Spalart–Allmaras turbulence model is also discretized using spline finite elements. If we let $\tilde{\nu}_h$ denote numerical approximation of the modified viscosity and define a suitable test function $\phi_h \in \mathcal{V}_h$, the method is given as

$$\mathcal{B}^G(\tilde{\nu}_h, \phi_h) = 0, \quad \phi_h \in \mathcal{V}_h^0,$$

where

$$\mathcal{B}^G(\tilde{\nu}_h, \phi_h) = \left( \frac{\partial \tilde{\nu}_h}{\partial t}, \phi_h \right) + c(\boldsymbol{u}_h; \tilde{\nu}_h, \phi_h) + a(\tilde{\nu}_h, \phi_h)$$
$$- s_1(\tilde{\nu}_h, \phi_h) - s_2(\tilde{\nu}_h; \tilde{\nu}_h, \phi_h) + s_3(\tilde{\nu}_h; \tilde{\nu}_h, \phi_h),$$

and with

$$(\tilde{\nu}, \phi) = \int_\Omega \tilde{\nu} \phi \, \mathrm{d}\boldsymbol{x},$$
$$c(\boldsymbol{u}; \tilde{\nu}, \phi) = (\boldsymbol{u} \cdot \nabla \tilde{\nu}, \phi),$$
$$a(\tilde{\nu}, \phi) = \left( \frac{(\nu + \tilde{\nu})}{\sigma} \nabla \tilde{\nu} \cdot \nabla \phi \right)$$
$$s_1(\tilde{\nu}, \phi) = (c_{b1}(1 - f_{t2}) \tilde{S} \tilde{\nu}, \phi),$$
$$s_2(\tilde{\nu}, \phi) = \left( \frac{c_{b2}}{\sigma} |\nabla \tilde{\nu}|^2, \phi \right),$$
$$s_3(\tilde{\nu}, \phi) = \left( \left( c_{w1} f_w - \frac{c_{b1}}{\kappa} f_{t2} \right) \left[ \frac{\tilde{\nu}}{d} \right]^2, \phi \right).$$

The negative Spalart-Allmaras model is discretized similarly.

For the temporal discretization we have used a semi-implicit Euler scheme, where the value of $\tilde{\nu}$ is evaluated at the previous time step $n$, i.e. $\tilde{\nu}^n$ is used, in some of the terms to get a linear problem for the new solution $\tilde{\nu}^{n+1}$. More precisely, if $\Delta t$ is the time step, then the time integration scheme reads

$$\left( \frac{\tilde{\nu}^{n+1} - \tilde{\nu}^n}{\Delta t}, \phi \right) + c(\boldsymbol{u}; \tilde{\nu}^{n+1}, \phi) + a(\tilde{\nu}^n; \tilde{\nu}^{n+1}, \phi) = s_1(\tilde{\nu}^{n+1}, \phi)$$
$$+ s_2(\tilde{\nu}^{n+1}, \phi) - s_3(\tilde{\nu}^{n+1}, \phi).$$

Here the convective term, the diffusion term and all three source terms are treated semi-implicitly. All the coefficients depending on $\tilde{\nu}$ are evaluated at time level $n$.

### 2.3.3. Boundary conditions for the Spalart-Allmaras Model

The Spalart-Allmaras model assumes that the mesh is sufficiently refined close to the wall surfaces with the non-dimensional wall distance $y^+ \sim 1$. The non-dimensional wall distance $y^+$ is defined in terms of the friction velocity $u_*$ as

$$y^+ = \frac{u_*}{\nu} \quad \text{with} \quad u_* = \sqrt{\frac{\tau_w}{\rho}}$$

where the wall shear stress $\tau_w$ is given by

$$\tau_w = \mu \left[ \frac{\partial \boldsymbol{u}}{\partial \boldsymbol{n}} \right]_{y=0} = \mu \left[ \nabla \boldsymbol{u} \cdot \boldsymbol{n} \right]_{y=0}.$$

Close to the wall the flow is laminar so $\tilde{\nu}$ is set to zero. On the inflow boundaries $\tilde{\nu}_{\text{in}} = 5\nu$ is used, whilst a homogeneous Neumann boundary condition is applied on the outflow boundaries and symmetry planes.

$$\frac{\partial \tilde{\nu}}{\partial \boldsymbol{n}} = \nabla \tilde{\nu} \cdot \boldsymbol{n} = 0.$$

*2.4. Aerodynamic coefficients*

The quantities of interest in numerical simulations of flow past an airfoil are the aerodynamic coefficients for a given angle of attack $\alpha$ and a given Reynolds number $Re$. The Reynolds number is defined as

$$Re = \frac{u_\infty c}{\nu},$$

where $u_\infty$ is the the constant inflow velocity, $c$ is the chord length and $\nu = \mu/\rho$ is the kinematic viscosity. The three coefficients are the drag coefficient $C_D$, the lift coefficient $C_L$ and the pressure coefficient $C_P$ defined as

$$C_D = \frac{F_x}{\frac{1}{2}\rho u_\infty^2 cl}, \quad C_L = \frac{F_y}{\frac{1}{2}\rho u_\infty^2 cl}, \quad C_P = \frac{p - p_\infty}{\frac{1}{2}\rho u_\infty^2}.$$

The quantities $F_x$ and $F_y$ are the horizontal and vertical force components acting on the airfoil respectively, $\rho$ is the density of the fluid, $l$ is the length in the spanwise direction and $p_\infty$ is the ambient pressure. The force components are computed as

$$F = [F_x, F_y]^T = \int_{\Gamma_w} \boldsymbol{\sigma} \cdot \boldsymbol{n} \, \mathrm{d}\boldsymbol{s},$$

where $\Gamma_w$ is the airfoil surface.

*2.5. Mesh generation*

Generation of a high quality block-structured mesh can often be a challenge with respect to partitioning the computational domain into 2D quadrilaterals which are not too skewed or distorted. Several other aspects are also relevant. First of all one would like to avoid distorted elements and abrupt change in the element size. Such cases can lead to unwanted grid effects. Secondly, we would like to have smaller elements at parts of the boundary with high curvature and close to solid walls in order to capture boundary layers.

*2.5.1. Block-structured mesh generation*

A bottom-up approach is often preferred for constructing a block-structured mesh. For two-dimensional problems the procedure can be described as

1. Define the corner nodes for the blocks.
2. Connect the corners to form the edges.
3. Refine the edges with a suitable grading.
4. Connect the edges to form surfaces.

To define the grading of the mesh a geometrical factor $r$ can be defined as the ratio of the element size of two consecutive elements, i.e. if $\{\boldsymbol{x}_i\}_{i=1}^m$ are the points on the edge or curve and $\Delta s_i = \|\boldsymbol{x}_i - \boldsymbol{x}_{i-1}\|_2$ defines the cell size, then

$$r = \Delta s_i / \Delta s_{i-1},$$

for $i = 2, \ldots, m$. To impose a smooth change in element size, we typically have that $0.8 < r < 1.2$, and for sharp boundary layers we may even use $0.9 < r < 1.1$ to capture the rapid change in the solution.

### 2.5.2. Spline curves

In this section we define spline curves, which form the foundation of the mesh generation, as in [13]. Assume that we have a knot-vector

$$\Xi = \{0 = \xi_1, \xi_2, \dots, \xi_{n+p+1} = 1\}.$$

and a set of control points $\boldsymbol{C} = \{\boldsymbol{c}_1, \dots, \boldsymbol{c}_n\}$ which defines the spline curve

$$\boldsymbol{c}(\xi) = \sum_{i=1}^{n} \boldsymbol{c}_i B_{i,p}(\xi),$$

where $\{B_i\}_{i=1}^{n}$ are the basis functions. The parameter $p$ is the polynomial order of the spline curve, and each knot $\xi_i$ may be repeated several times, but the knot-span should be non-decreasing

$$\xi_1 \le \xi_2 \le \cdots \le \xi_{n+p+1}.$$

For $p = 0$ the basis functions are piecewise constants

$$B_{i,0}(\xi) = \begin{cases} 1, & \xi_i \le \xi < \xi_{i+1}, \\ 0 & \text{otherwise.} \end{cases}$$

The higher order B-spline basis functions are defined as a linear combination of splines of lower order using the *Cox-de Boor recursion formula*

$$B_{i,p}(\xi) = \frac{\xi - \xi_i}{\xi_{i+p} - \xi_i} B_{i,p-1}(\xi) + \frac{\xi_{i+p+1} - \xi}{\xi_{i+p+1} - \xi_{i+1}} B_{i+1,p-1}(\xi). \tag{3}$$

We restrict our attention to *open* knot-vectors, i.e. splines that are interpolatory at the end points, and then the first and last knots are repeated $p + 1$ times. Furthermore, if the spline is $C^{p-1}$ continuous then all the internal knots have multiplicity one and the knot-vector can be written as

$$\Xi = \{\underbrace{\xi_1, \dots, \xi_1}_{p+1}, \xi_2, \dots, \xi_{m-1}, \underbrace{\xi_m, \dots \xi_m}_{p+1}\},$$

where the number of unique knots is given by $q = n - p + 1$. The corresponding knot-vector without repeated knots is

$$\bar{\Xi} = \{\bar{\xi}_1, \bar{\xi}_2, \dots, \bar{\xi}_q\}.$$

### 2.5.3. Cubic spline interpolation

The mesh generation process is dependent on standard cubic spline interpolation [29]. The starting point is a set of $m$ points $\{\boldsymbol{x}_i\}_{i=1}^{m}$ that we want to approximate by a cubic spline curve $\boldsymbol{c}(\xi)$ such that

- $\boldsymbol{c}(\tilde{\xi}_i) = \boldsymbol{x}_i$ for $\tilde{\xi}_i \in [0, 1]$.

- $\boldsymbol{c}(\xi) \in \boldsymbol{C}^2([0, 1])$.

The points $\{\tilde{\xi}_i\}_{i=1}^q$ where the spline curve interpolates the data are called the *Greville points*. Two extra conditions are needed to uniquely define the interpolation. We use either Hermitian $(\boldsymbol{c}'(0) = \boldsymbol{t}_0, \boldsymbol{c}'(1) = \boldsymbol{t}_1)$ or natural boundary conditions $(\boldsymbol{c}''(0) = \boldsymbol{c}''(1) = 0)$, where $\boldsymbol{t}_0$ and $\boldsymbol{t}_1$ are the tangent vectors of the spline curve at the endpoints. This leads to an $n \times n$ linear system with $n = m + 2$, which can be solved for the unknown control points $\{\boldsymbol{c}_i\}_{i=1}^n$. The interpolation is not uniquely defined since the parametrization can be different.

Cubic spline interpolation is used for the airfoil as given in Equation (1). The entire mesh is made for polynomial order $p = 3$, and only lowered to orders $p = 1$ and $p = 2$ once all patches and refinements have been completed.

### 2.5.4. Surface generation

For surface generation we employ the concept of Coons patches [30]. Given four boundary curves $\boldsymbol{u}_0(\xi)$, $\boldsymbol{u}_1(\xi)$, $\boldsymbol{w}_0(\eta)$, $\boldsymbol{w}_1(\eta)$ as given in Figure 1. These



Figure 1: Boundary curves for Coons surface patch.

curves have normalized knot vectors and are connected such that $\boldsymbol{u}_0(\xi_1) = \boldsymbol{w}_0(0)$, $\boldsymbol{u}_0(1) = \boldsymbol{w}_1(0)$, $\boldsymbol{u}_1(1) = \boldsymbol{w}_1(1)$, $\boldsymbol{u}_1(0) = \boldsymbol{w}_0(1)$, thus forming a closed loop. By defining the surfaces

$$S_1(\xi, \eta) = (1 - \eta)\boldsymbol{u}_0(\xi) + \eta\boldsymbol{u}_1(\xi)$$
$$S_2(\xi, \eta) = (1 - \eta)\boldsymbol{w}_0(\eta) + \xi\boldsymbol{w}_1(\eta)$$
$$S_3(\xi, \eta) = (1 - \xi)(1 - \eta)\boldsymbol{u}_0(0) + \xi(1 - \eta)\boldsymbol{u}_0(1) + \eta(1 - \xi)\boldsymbol{u}_1(0) + \xi\eta\boldsymbol{u}_1(1)$$

the Coons surface paths is given by

$$S_c(\xi, \eta) = S_1(\xi, \eta) + S_2(\xi, \eta) - S_3(\xi, \eta).$$

The Coons surface patch approach is a quick and easy way of building the surfaces. Being able to define the geometry through the boundary curves of each surface or patch is a great advantage.

## 3. Simulations Setup

A high quality mesh is a prerequisite for a reliable simulation of flow around an aerodynamically shaped body like an airfoil. Here we describe the meshes used for our 2D simulations and the basis for the choice of domain size and time step. Other test cases are also defined.

### 3.1. Mesh description

The meshes are denoted by B followed by an identifying number indicating the level of refinement, i.e. B0 is the coarsest mesh and B2 the finest mesh in our simulations. The meshes are constructed with polynomials of orders 1, 2 and 3, and are intended for use with the Spalart-Allmaras model without any law-of-the-wall parametrization. Each mesh consists of 128 patches, which gives huge flexibility in the number of processors the simulations can be run on. The simulations in this paper are run on 12, 16, 24, 32 or 64 cores. IFEM is parallelized through a domain decomposition approach [31] where each sub-domain consist of one or more patches. The code uses the PETSc [32] for the parallel matrix classes and for the solution of the resulting linear system. The use of PETSc also gives access to iterative (Krylov-type) solution methods and state-of-the-art advanced preconditioners such as algebraic multigrid [33] and additive Schwarz [34]. When it comes to refinement, a basic template given in Figure 2 is used as a starting point. The figure also shows four refinement edges (marked by bold lines) which are used in the mesh generation.
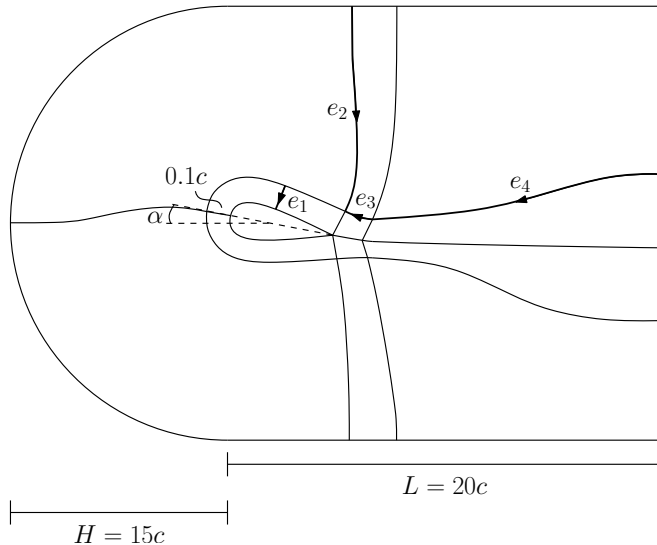


Figure 2: NACA0015: Basic block structure and definition of refinement edges for fixed NACA0015 airfoil with angle of attack $\alpha$.

Important refinement parameters for the meshes are presented in Table 1, whilst the grading factors for the different meshes are illustrated in Figure 3. The resulting number of element and degrees-of-freedom are listed in Table 2. Figure 4 shows the B0 mesh for $\alpha = 6°$ and $p = 2$.

In order to evaluate the quality of the meshes we use in our simulations we apply some well-known mesh metrics. The scaled Jacobian mesh metric, described in [35], is shown in Figure 5 for the coarsest grid B0. As can be seen in the figure the scaled Jacobian is positive for all elements, meaning that there should be no unphysical results due to intersecting grid lines. The stretch mesh

Table 1: NACA0015: Detailed refinement information about simulation meshes B0, B1 and B2. Edge grading factor is given by $r$, and $n_{\text{pts}}$ is the number of points along the airfoil surface whilst $n$ is the number of inserted knots along the given edge.

| Mesh | | B0 | B1 | B2 |
|---|---|---|---|---|
| Airfoil | $n_{\text{pts}}$ | 103 | 127 | 173 |
| | $r$ | 0.96 | 0.96 | 0.97 |
| $e_1$ | $r$ | 0.81 | 0.89 | 0.92 |
| | $n$ | 36 | 60 | 80 |
| $e_2$ | $r$ | 0.88 | 0.92 | 0.94 |
| | $n$ | 35 | 55 | 75 |
| $e_3$ | $r$ | 0.9 | 0.91 | 0.93 |
| | $n$ | 12 | 18 | 24 |
| $e_4$ | $r$ | 0.89 | 0.92 | 0.94 |
| | $n$ | 35 | 50 | 65 |
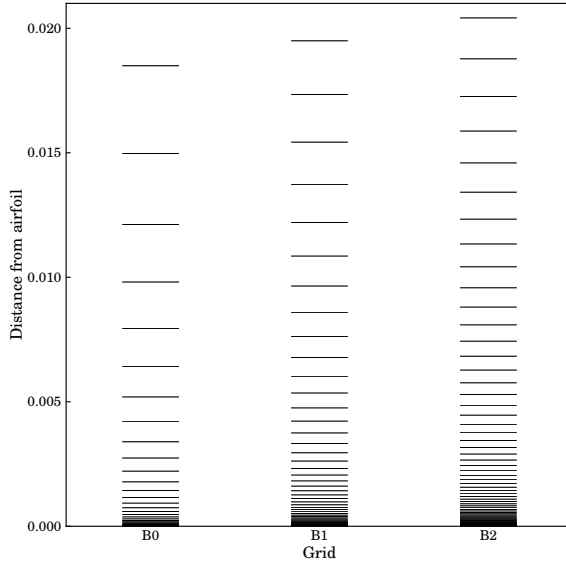


Figure 3: NACA0015: Grading factor illustration (zoomed) of the innermost patches close to the airfoil for the different meshes.

metric is shown in Figure 6. The IFEM solver is able to handle large element aspect ratios.

Table 2: NACA0015: Number of elements and degrees-of-freedom for simulation meshes B0, B1 and B2 and polynomial orders $p = 1, 2, 3$.

| Mesh | $p$ | $n_{\mathrm{el}}$ | $n_{\mathrm{dof}}$ |
|------|-----|-------|-------|
|      | 1   | 22046 | 67116 |
| B0   | 2   | 22046 | 78222 |
|      | 3   | 22046 | 90096 |
|      | 1   | 45864 | 138909 |
| B1   | 2   | 45864 | 155319 |
|      | 3   | 45864 | 172497 |
|      | 1   | 82582 | 249522 |
| B2   | 2   | 82582 | 271380 |
|      | 3   | 82582 | 294006 |



(a) NACA0015: Mesh B0, $p = 2$.

(b) NACA0015: Closeup view of mesh B0, $p = 2$.
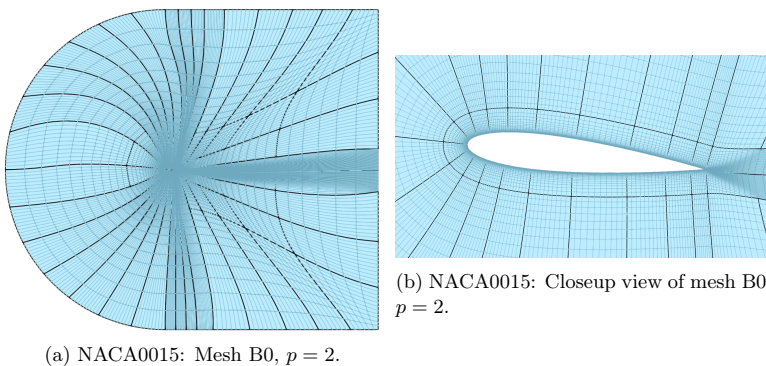
Figure 4: NACA0015: Grid B0 for $\alpha = 6°$. Patch boundaries in black.

## 3.2. Physical parameters and boundary conditions

All simulations are based on a fluid density of $\rho = 1.205$ kg/m$^3$, dynamic viscosity $\mu = 1.8208 \times 10^{-5}$ kg/(m s) and inflow velocity $u_\infty = 37.775$ m/s giving a Reynolds number of $Re = 2.5 \times 10^6$. An inlet boundary condition is imposed on the curved surface, a wall boundary condition is imposed on the airfoil surface, a slip condition is applied on the lateral boundaries while a homogeneous Neumann condition is used for the outflow.

## 3.3. Determination of the domain size

In the simulation of the kind presented in the paper one expects the aerodynamic coefficients of the airfoil to be independent of the location of the boundaries. Sensitivity studies were conducted to identify the domain extent. Basically the dimensions $L$ and $H$ (Figure 2) were varied and simulations for five different domain extents (B1, K0, K1, K2, K3) were conducted to compute the drag and lift coefficients. The specifications of the domain set-ups are given in Table 3. In all the five setups the airfoil is discretized using $n = 127$ points along the surface with a grading factor of $r = 0.96$ towards both the trailing and the
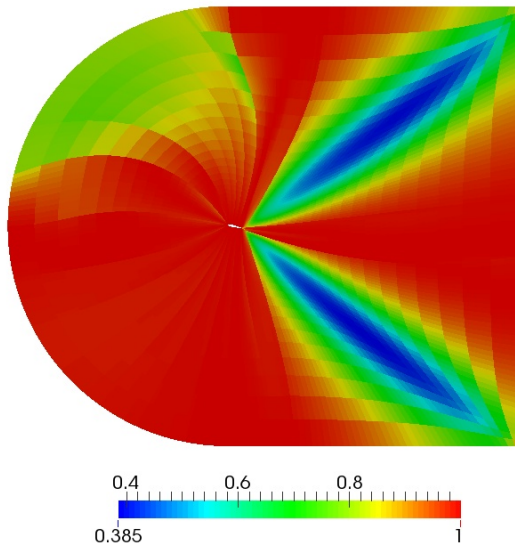
Figure 5: NACA0015: Scaled Jacobian mesh metric for grid B0 at 12° angle of attack.
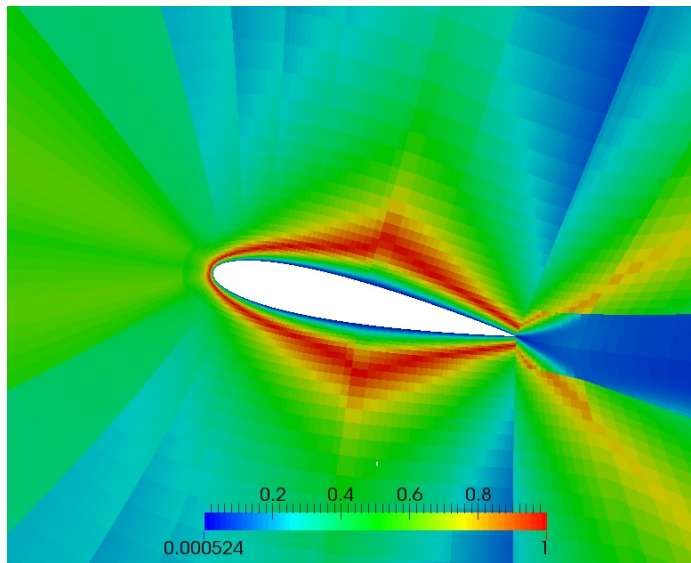


Figure 6: NACA0015: Stretch mesh metric for grid B0 at 12° angle of attack.

leading edges. All the simulations were conducted for an angle of attack $\alpha = 6^o$, order $p = 1$ and until a non-dimensional time $t = 50$. The results for drag and

17

lift coefficients are shown in Table 4. The sixth and the seventh column in the table shows the percentage error in $C_L$ and $C_D$ associated with the changes in the domain size with respect to B1. The percentage change in any case is less than 2.5% which should be acceptable for all practical purposes. We thus fix the B1 domain configuration for subsequent analysis. The chosen domain setup is shown in Figure 7.
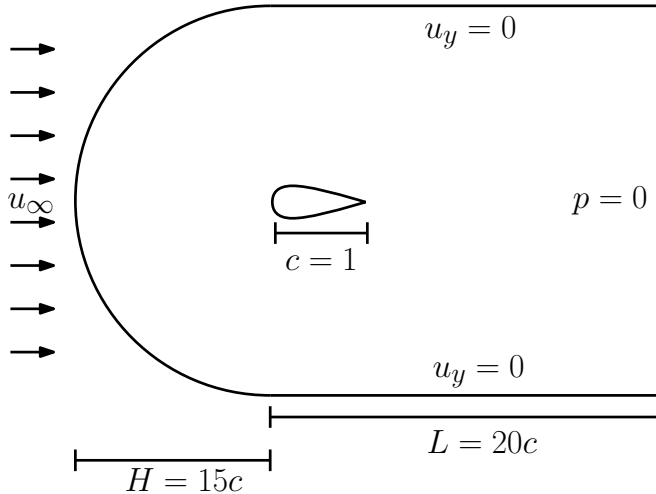


Figure 7: NACA0015: Computational domain for fixed NACA0015 airfoil.

Table 3: NACA0015: Details of mesh and domain size. Edge grading factor is given by $r$, whilst $n$ is the number of inserted knots.

| Grid | | B1 | K0 | K1 | K2 | K3 |
|------|---|------|------|------|------|------|
| $H$ | | $15c$ | $15c$ | $15c$ | $10c$ | $20c$ |
| $L$ | | $20c$ | $15c$ | $30c$ | $20c$ | $20c$ |
| $n_{el}$ | | 45864 | 44694 | 47736 | 43120 | 47824 |
| $n_{dof}$ | | 138909 | 135384 | 144549 | 130656 | 144804 |
| $e_1$ | $r$ | 0.89 | 0.89 | 0.89 | 0.89 | 0.89 |
| | $n$ | 60 | 60 | 60 | 60 | 60 |
| $e_2$ | $r$ | 0.92 | 0.92 | 0.92 | 0.92 | 0.92 |
| | $n$ | 55 | 55 | 55 | 48 | 60 |
| $e_3$ | $r$ | 0.91 | 0.91 | 0.91 | 0.91 | 0.91 |
| | $n$ | 18 | 18 | 18 | 18 | 18 |
| $e_4$ | $r$ | 0.92 | 0.92 | 0.925 | 0.92 | 0.92 |
| | $n$ | 50 | 45 | 58 | 50 | 50 |

Based on the small variations in the lift and drag coefficient a problem area size of $H = 15c$ and $L = 20c$ is chosen.

18

Table 4: NACA0015: Results for flow past a NACA0015 airfoil at $\alpha = 12°$ with $p = 1$.

| Grid | $p$ | $\Delta t$ | $\alpha = 12°$ | | $\frac{|C_L - C_{L,B1}|}{C_{L,B1}}$ [%] | $\frac{|C_D - C_{D,B1}|}{C_{D,B1}}$ [%] |
| | | | $C_L$ | $C_D$ | | |
|---|---|---|---|---|---|---|
| B1 | 1 | 0.0005 | 1.21490 | 0.02352 | - | - |
| K0 | 1 | 0.0005 | 1.20620 | 0.02407 | 0.72 | 2.31 |
| K1 | 1 | 0.0005 | 1.21041 | 0.02317 | 0.37 | 1.49 |
| K2 | 1 | 0.0005 | 1.21011 | 0.02387 | 0.39 | 1.46 |
| K3 | 1 | 0.0005 | 1.20820 | 0.02355 | 0.55 | 0.10 |

### 3.4. Time step determination

In order to determine a sufficiently small time step several simulations were run on the finest grid, B2, with a sufficiently small time step $\Delta t = 0.0005$ or $\Delta t = 0.00035$ and spline elements of order $p = 1$, $p = 2$ and $p = 3$ for three angles of attack. All simulations were run to non-dimensional time $t = 75$, equaling 150000 or approximately 214000 time steps. The results are shown in Table 5. As all simulations converge it can be safely concluded that the Courant-Friedrichs-Lewy (CFL) condition, which is necessary for stability, is satisfied. All subsequent simulations were therefore conducted with time step given in Table 5.

Table 5: NACA0015: Results for grid B2 in determination of the time step $\Delta t$.

| | Grid | $p$ | $\alpha$ [°] | $\Delta t$ | $C_L$ | $C_D$ |
|---|---|---|---|---|---|---|
| IFEM (SA) | B2 | 1 | 0 | 0.0005 | $-0.00016$ | 0.01041 |
| IFEM (SA) | B2 | 1 | 6 | 0.0005 | 0.64573 | 0.01299 |
| IFEM (SA) | B2 | 1 | 12 | 0.0005 | 1.21902 | 0.02286 |
| IFEM (SA) | B2 | 2 | 0 | 0.0005 | 0.00001 | 0.01046 |
| IFEM (SA) | B2 | 2 | 6 | 0.0005 | 0.63758 | 0.01298 |
| IFEM (SA) | B2 | 2 | 12 | 0.0005 | 1.20819 | 0.02276 |
| IFEM (SA) | B2 | 3 | 0 | 0.0005 | $-0.00003$ | 0.01047 |
| IFEM (SA) | B2 | 3 | 6 | 0.0005 | 0.63409 | 0.01301 |
| IFEM (SA) | B2 | 3 | 12 | 0.00035 | 1.20745 | 0.02187 |

### 3.5. Simulation length

In order to determine the lift and drag parameters it is crucial that the simulations are run until a quasi steady-state situation is achieved. This is monitored through the cumulative lift and drag coefficients. A time history plot of the cumulative mean of the lift and drag coefficients for grid B0, $p = 2$, $\alpha = 12°$ and $\Delta t = 0.0005$ is shown in Figure 8.

Based on these results, the calculations of the lift and drag coefficients are based on the time interval between 70 and 75 ($\approx 10000$ time steps).

### 3.6. Definition of test cases

Once the domain size, time steps and simulation length are established further simulations were conducted for three mesh setups B0, B1, B2 with linear,
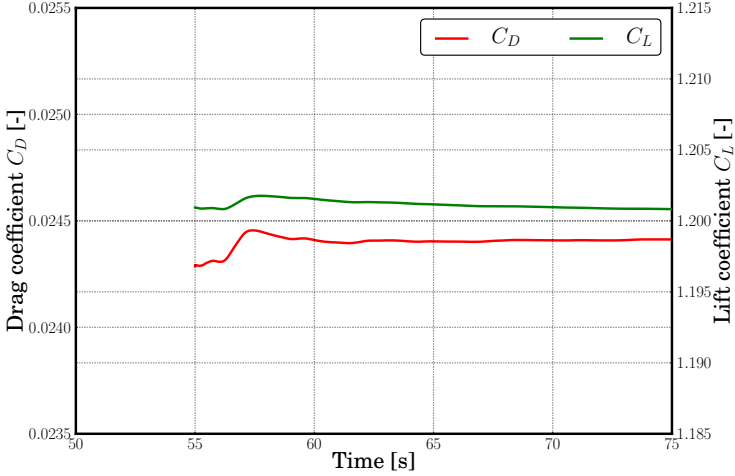
Figure 8: NACA0015: Cumulative mean of $C_L$ and $C_D$ at $\alpha = 12°$ for grid B0, $p = 2$, $\Delta t = 0.0005$.

quadratic and cubic spline elements with a time step as given in Table 5. All inputs, including boundary conditions, are identical for all the cases with an angle of attack $\alpha = 0°, 6°, 12°$. Thus a total of 27 cases are investigated.

## 4. Results and discussion

Results from the 27 different cases discussed in the previous section are now compared against two sets of experimental ([36],[37]) results. While the results in [37] come from the experiments conducted at the same Reynolds number as in this paper, the results in [36] were obtained from wind tunnel experiments conducted at lower Reynolds numbers and then extended to higher ones. In the following subsections we present and discuss our 2D simulation results for different angles of attack $\alpha$.

### 4.1. Results for $\alpha = 0°$

An angle of attack of $\alpha = 0°$ corresponds to a situation where the flow is expected to be statistically symmetric and absence of any flow separation. Experimental values of nearly zero lift therefore does not come as a surprise. The pressure field in Figure 21a computed by numerical simulation is symmetric about the chord line which implies that the pressure integrated over the top surface and bottom surface will be equal in magnitude and opposite in direction resulting in a net zero lift. Also the flow impinges on the leading edge resulting in a relatively high pressure zone on this side of the flow and hence a positive drag coefficient.

20

### 4.1.1. Lift and drag coefficients for $\alpha = 0°$

Lift and drag coefficients for $\alpha = 0°$ are shown in Table 6 along with experimental results available in the literature. The results are also presented in Figure 9. Lift coefficients are predicted very well in our simulations and compare well to the two sets of experimental results. Drag coefficients on the other hand are overpredicted. This is as expected due to the use of the Spalart-Allmaras turbulence model which assumes fully turbulent flow. However, drag coefficients seem to be better approximated for $p = 1$ than for $p = 2$ and $p = 3$, whilst lift coefficients seem to be better approximated with increasing spline element order $p$.

### 4.1.2. Surface pressure plots for $\alpha = 0°$

The surface pressure coefficients for mesh B2 and $p = 1, 2, 3$ computed using IFEM are compared against experimental results from [37] in Figure 10. Figures 11 and 12 give a zoomed-in view of the $C_p$ plot towards the leading and trailing edges respectively. The comparisons for $p = 1$, $p = 2$ and $p = 3$ are in good agreement.

### 4.2. Results for $\alpha = 6°$

As the angle of attack increases to $\alpha = 6°$ the flow becomes asymmetric. Figure 21b shows that a relatively large surface area now tries to obstruct the flow resulting in the development of high pressure zone on the bottom-leading side of the airfoil. The asymmetric distribution of the pressure on the airfoil results not only in a net upward lift but also a positive drag force. The experiments confirm the results.

### 4.2.1. Lift and drag coefficients for $\alpha = 6°$

For $\alpha = 6°$, lift and drag coefficients are shown in Table 7 along with experimental results available in the literature. The results are also presented in Figure 13. The drag coefficients seem to be somewhat higher than the experimental results. This overprediction is again due to the Spalart-Allmaras turbulence model assuming fully turbulent flow. Again, drag coefficients for

Table 6: NACA0015: Lift and drag coefficients for flow past a fixed NACA0015 airfoil at $\alpha = 0°$ and $Re = 2.5 \times 10^6$.

|  | Grid | $p$ | $\Delta t$ | $C_L$ | $C_D$ |
|---|---|---|---|---|---|
| IFEM (SA) | B0 | 1 | 0.0005 | $-0.00009$ | 0.01031 |
| IFEM (SA) | B0 | 2 | 0.0005 | 0.00001 | 0.01047 |
| IFEM (SA) | B0 | 3 | 0.0005 | $-0.00005$ | 0.01054 |
| IFEM (SA) | B1 | 1 | 0.0005 | 0.00007 | 0.01040 |
| IFEM (SA) | B1 | 2 | 0.0005 | 0.00020 | 0.01045 |
| IFEM (SA) | B1 | 3 | 0.0005 | 0.00000 | 0.01049 |
| IFEM (SA) | B2 | 1 | 0.0005 | $-0.00016$ | 0.01041 |
| IFEM (SA) | B2 | 2 | 0.0005 | 0.00001 | 0.01046 |
| IFEM (SA) | B2 | 3 | 0.0005 | $-0.00003$ | 0.01047 |
| Exp: McAlister et al. [37] |  |  |  | -0.01 - 0.00 | 0.00 |
| Exp: Sheldal et al. [36] |  |  |  | 0.000 | 0.0070 |
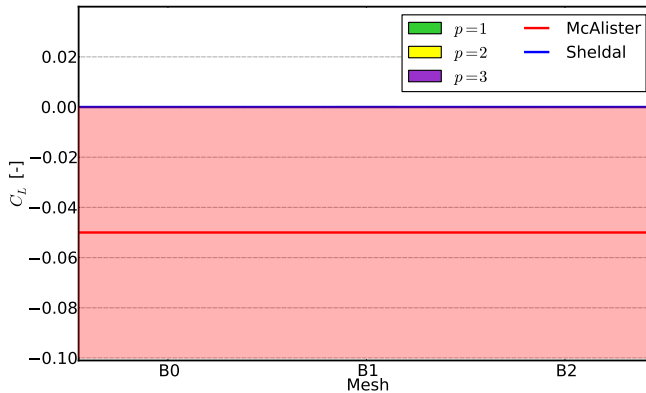
(a) Lift coefficients ($\alpha = 0°$).
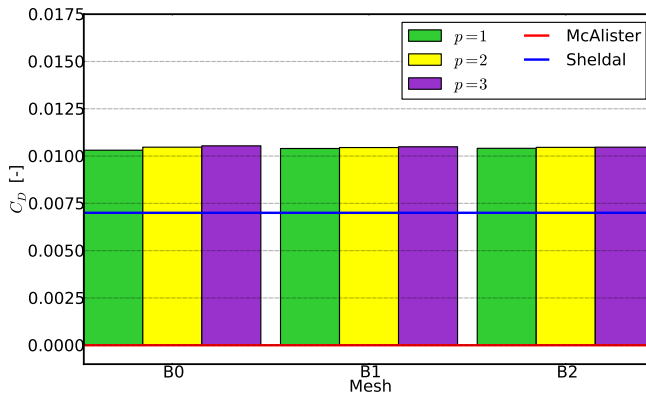


(b) Drag coefficients ($\alpha = 0°$).

Figure 9: NACA0015: Lift and drag coefficients for flow past a fixed NACA0015 airfoil at $\alpha = 0°$ and $Re = 2.5 \times 10^6$.

$p = 2$ and $p = 3$ are higher than for $p = 1$. The lift coefficients obtained for all three grids are closer to the experiments in [36] than in [37]. Lift coefficients obtained with $p = 1$ are lower than for $p = 2$ and $p = 3$.

*4.2.2. Surface pressure plots for $\alpha = 6°$*

Surface pressure coefficient plots for IFEM runs with the Spalart-Allmaras turbulence model are presented in Figure 14 for grid B2, alongside comparisons with surface pressure distributions from experiments in [37]. Figure 15 and 16 once again gives a zoomed in view of the $C_p$ plot towards the leading and trailing edges respectively. In this case, even for sufficiently fine mesh the coefficients are not accurately predicted towards both the edges. There are only minor differences in the $C_p$-curves for different polynomial orders.
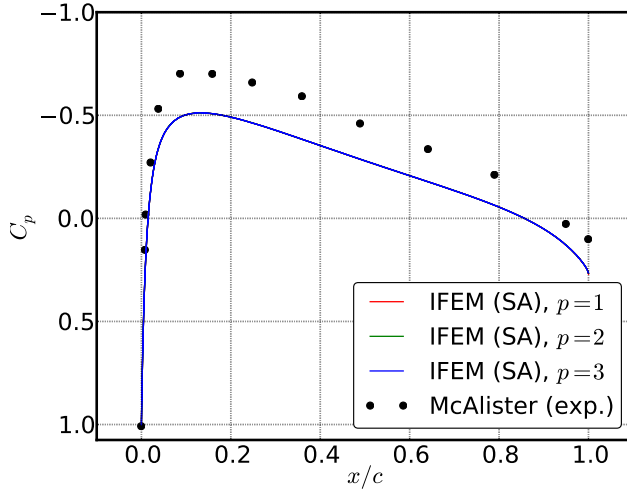
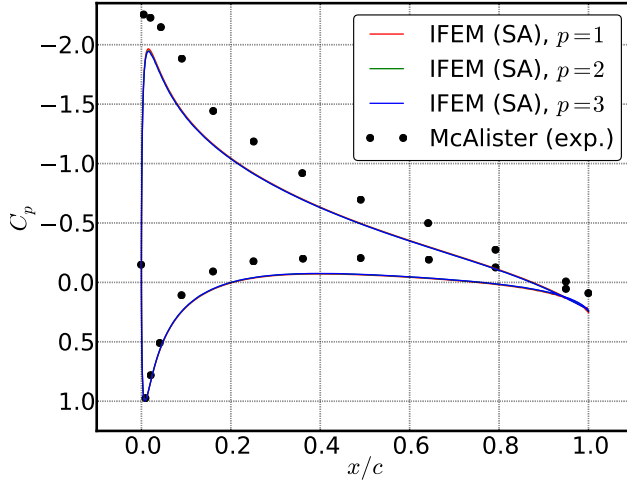Figure 10: NACA0015: Surface pressure plot for $\alpha = 0°$. Simulation run for grid B2 with $p = 1$, $p = 2$ and $p = 3$, $\Delta t = 0.0005$.
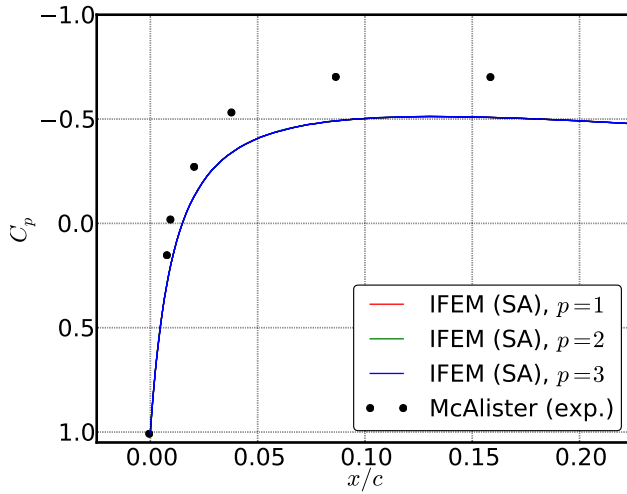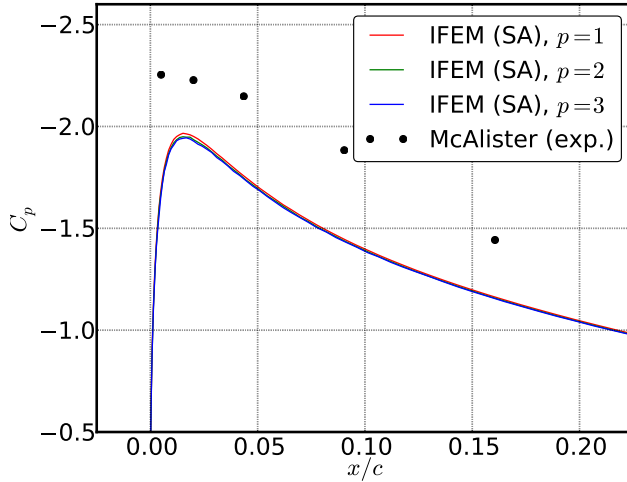


Figure 11: NACA0015: Surface pressure plot of leading edge for $\alpha = 0°$. Simulation run for grid B2 with $p = 1$, $p = 2$ and $p = 3$, $\Delta t = 0.0005$.
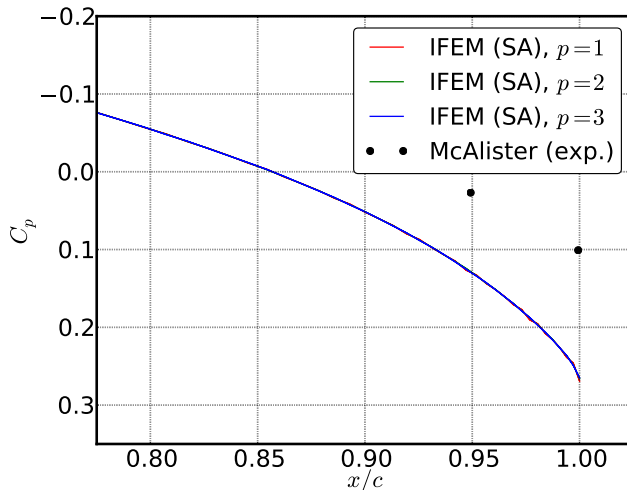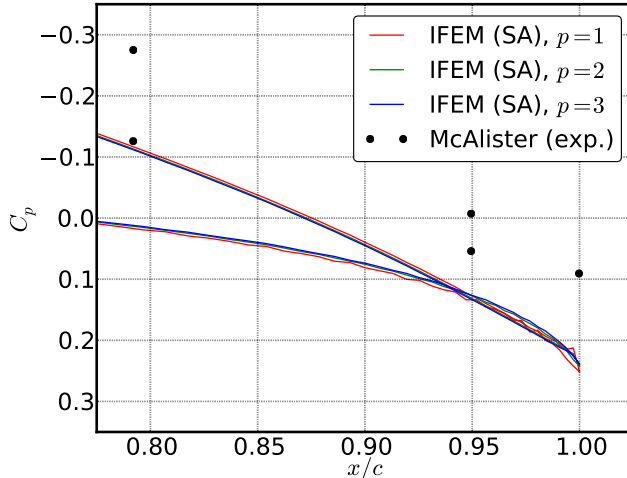
Figure 12: NACA0015: Surface pressure plot of trailing edge for $\alpha = 0°$. Simulation run for grid B2 with $p = 1$, $p = 2$ and $p = 3$, $\Delta t = 0.0005$.
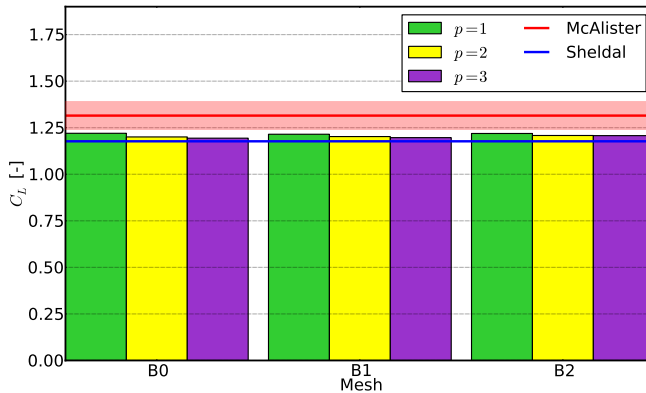
Table 7: NACA0015: Lift and drag coefficients for flow past a fixed NACA0015 airfoil at $\alpha = 6°$ and $Re = 2.5 \times 10^6$.

|  | Grid | $p$ | $\Delta t$ | $C_L$ | $C_D$ |
|---|---|---|---|---|---|
| IFEM (SA) | B0 | 1 | 0.0005 | 0.66101 | 0.01315 |
| IFEM (SA) | B0 | 2 | 0.0005 | 0.64599 | 0.01323 |
| IFEM (SA) | B0 | 3 | 0.0005 | 0.64000 | 0.01330 |
| IFEM (SA) | B1 | 1 | 0.0005 | 0.64732 | 0.01306 |
| IFEM (SA) | B1 | 2 | 0.0005 | 0.63829 | 0.01310 |
| IFEM (SA) | B1 | 3 | 0.0005 | 0.63419 | 0.01311 |
| IFEM (SA) | B2 | 1 | 0.0005 | 0.64573 | 0.01299 |
| IFEM (SA) | B2 | 2 | 0.0005 | 0.63758 | 0.01298 |
| IFEM (SA) | B2 | 3 | 0.0005 | 0.63409 | 0.01301 |
| Exp: McAlister et al. [37] |  |  |  | 0.69 - 0.71 | 0.01 |
| Exp: Sheldal et al. [36] |  |  |  | 0.660 | 0.0089 |

*4.3. Results for $\alpha = 12°$*

As the angle of attack is further increased to $\alpha = 12°$ more of the bottom surface of the airfoil is exposed to the incident flow and hence higher pressure. Contrary to that, the top surface is shielded from the incident flow and hence relatively much lower pressure is experienced. As in the previous case it results in positive lift and drag forces albeit much bigger in magnitude. Once again the prediction is confirmed by experimental observations.

24
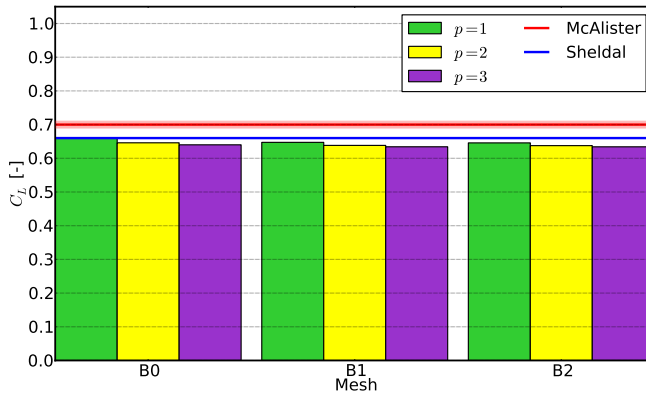
(a) Lift coefficients ($\alpha = 6°$).
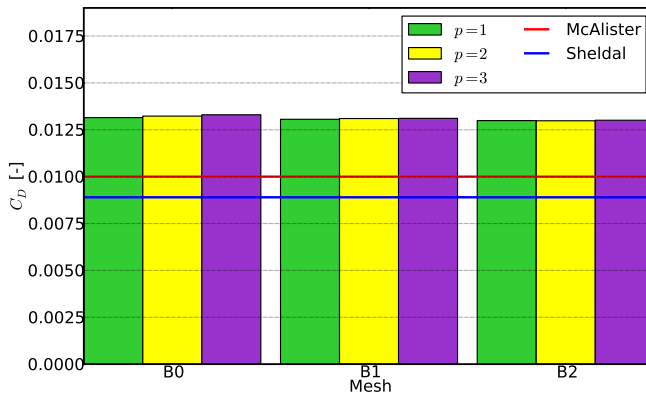


(b) Drag coefficients ($\alpha = 6°$).

Figure 13: NACA0015: Lift and drag coefficients for flow past a fixed NACA0015 airfoil at $\alpha = 6°$ and $Re = 2.5 \times 10^6$.

### 4.3.1. Lift and drag coefficients for $\alpha = 12°$

Lift and drag coefficients for $\alpha = 12°$ are shown in Table 8 along with experimental results available in the literature. The results are also presented in Figure 17. The drag coefficients are once again overpredicted compared to the experimental results. For the lift coefficients the differences between $p = 1$ on the one hand and $p = 2$ and $p = 3$ on the other are more pronounced than for lower angles of attack. Lift coefficients are in between the experimental results in [36] and [37] and thus show reasonable agreement.

### 4.3.2. Surface pressure plots for $\alpha = 12°$

Surface pressure coefficient plots for IFEM run with the Spalart-Allmaras turbulence model are presented in Figure 18, alongside comparisons with surface pressure distributions from experiments in [37].

As for the two lower angles of attack, there are only minor differences in the prediction of pressure coefficients along the whole airfoil when using spline



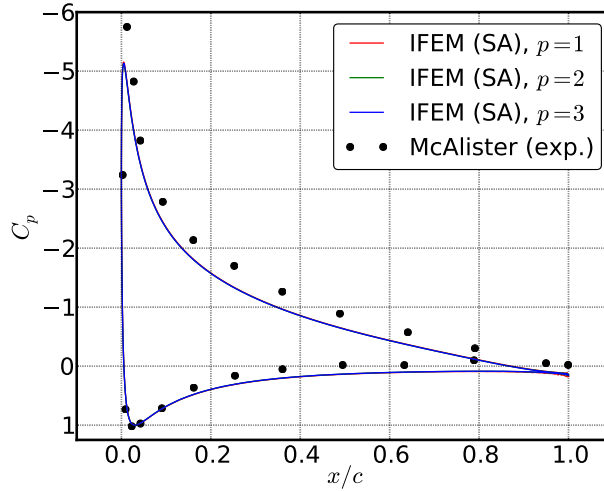Figure 14: NACA0015: Surface pressure plot for $\alpha = 6°$. Simulation run for grid B2 with $p = 1$, $p = 2$ and $p = 3$, $\Delta t = 0.0005$.



Figure 15: NACA0015: Surface pressure plot of leading edge for $\alpha = 6°$. Simulation run for grid B2 with $p = 1$, $p = 2$ and $p = 3$, $\Delta t = 0.0005$.
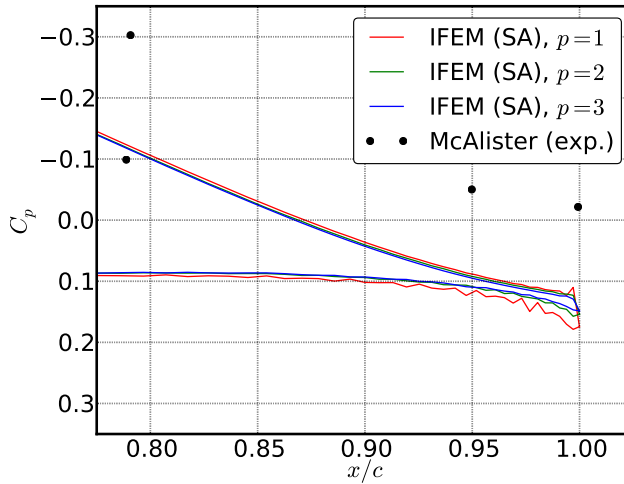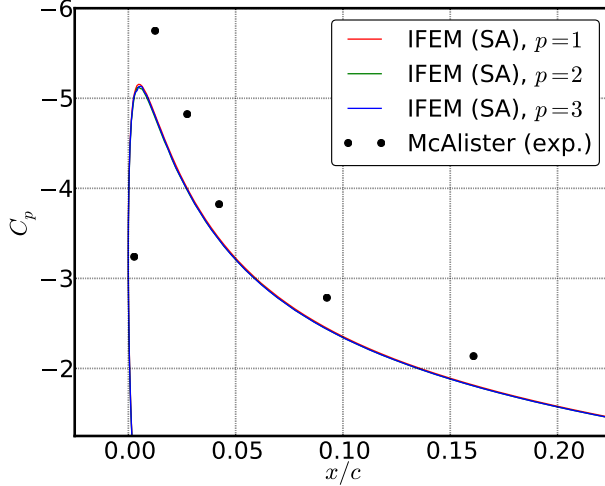
Figure 16: NACA0015: Surface pressure plot of trailing edge for $\alpha = 6°$. Simulation run for grid B2 with $p = 1$, $p = 2$ and $p = 3$, $\Delta t = 0.0005$.

Table 8: NACA0015: Lift and drag coefficients for flow past a fixed NACA0015 airfoil at $\alpha = 12°$ and $Re = 2.5 \times 10^6$.

|  | Grid | $p$ | $\Delta t$ | $C_L$ | $C_D$ |
|---|---|---|---|---|---|
| IFEM (SA) | B0 | 1 | 0.0005 | 1.22001 | 0.02446 |
| IFEM (SA) | B0 | 2 | 0.0005 | 1.20042 | 0.02443 |
| IFEM (SA) | B0 | 3 | 0.0005 | 1.19376 | 0.02451 |
| IFEM (SA) | B1 | 1 | 0.0005 | 1.21490 | 0.02352 |
| IFEM (SA) | B1 | 2 | 0.0005 | 1.20243 | 0.02344 |
| IFEM (SA) | B1 | 3 | 0.0005 | 1.19667 | 0.02343 |
| IFEM (SA) | B2 | 1 | 0.0005 | 1.21902 | 0.02286 |
| IFEM (SA) | B2 | 2 | 0.0005 | 1.20819 | 0.02276 |
| IFEM (SA) | B2 | 3 | 0.00035 | 1.20745 | 0.02187 |
| Exp: McAlister et al. [37] |  |  |  | 1.24 - 1.39 | 0.03 - 0.06 |
| Exp: Sheldal et al. [36] |  |  |  | 1.177 | 0.0157 |

elements of order polynomial order $p = 1, 2, 3$.

### 4.4. Low Re investigations

As all results presented so far have shown only little or no improvement for the surface pressure distributions with increasing spline element order, we make some additional investigations at a low Reynolds number, $Re = 250$. This is done for two grids. The first is B0 as presented earlier, with a distance to the first knotline designed for $y^+ = 1$ at $Re = 2.5 \times 10^6$ The other is B3, much coarser than grids B0-B2 and designed for $Re = 250$, with 10890 elements. Distance

(a) Lift coefficients ($\alpha = 12°$).
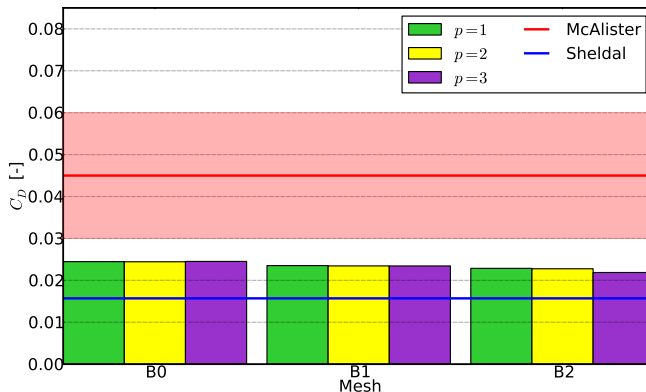


(b) Drag coefficients ($\alpha = 12°$).

Figure 17: NACA0015: Lift and drag coefficients for flow past a fixed NACA0015 airfoil at $\alpha = 12°$ and $Re = 2.5 \times 10^6$.

to the first knotline for B3 is $0.2/\sqrt{(Re)}$, and all investigations are carried out at an angle of attack $\alpha = 12°$. The resulting surface pressure distributions are shown in Figure 22. From the figure is it clear that polynomial order has an impact only for grid B3, not for grid B0 which is designed to resolve the boundary layer for $Re = 2.5 \times 10^6$. The significant difference is between linear elements on the one side and quadratic and cubic elements on the other.

## 5. Conclusions

The major contribution of this work has been the demonstration of the usage of a Navier-Stokes solver based on an isogeometric finite element method using a Chorin projection method and Spalart-Allmaras turbulence model to simulate high Reynolds number flow ($Re = 2.5 \times 10^6$) around the NACA0015 airfoil

for three different angles of attack. Also, another original contribution is the design of meshes for isogeometric computation of airfoil flows. Most significant



Figure 18: NACA0015: Surface pressure plot for $\alpha = 12°$. Simulation run for grid B2 with $p = 1$, $p = 2$ and $p = 3$, $\Delta t = 0.0005$ for $p = 1, 2$, $\Delta t = 0.00035$ for $p = 3$.



Figure 19: NACA0015: Surface pressure plot of trailing edge for $\alpha = 12°$. Simulation run for grid B2 with $p = 1$, $p = 2$ and $p = 3$, $\Delta t = 0.0005$ for $p = 1, 2$, $\Delta t = 0.00035$ for $p = 3$.

Figure 20: NACA0015: Surface pressure plot of leading edge for $\alpha = 12°$. Simulation run for grid B2 with $p = 1$, $p = 2$ and $p = 3$, $\Delta t = 0.0005$ for $p = 1, 2$, $\Delta t = 0.00035$ for $p = 3$.

concluding remarks are enumerated as follows:

- The solver presented computes lift, drag and pressure coefficients which are in reasonable agreement with the experimental observations. The pressure coefficients were underpredicted for all the angles of attack.

- The work also investigates in detail and comes up with a choice of domain size, mesh resolution, time step and simulation length for the flow investigated.

- It gets increasingly more difficult numerically to predict drag, lift and pressure coefficients with increasing angle of attack.

- There is very little benefit evident from the usage of higher order splines, particularly for prediction of $C_p$.

- It appears that the gain in numerical accuracy is more than offset by the modeling error associated with RANS-based turbulence modeling approach. This is perhaps the reason no improvement in accuracy was observed when the simulations were conducted with high Reynolds number and Spalart-Allmaras turbulence model. On the contrary, at low Reynolds number when no turbulence model was activated, the added value due to higher order splines was observed for the coarse mesh. This explanation can be taken to argue in favor of a turbulence resolving approach in comparison to a turbulence modeling approach.

- The numerical results have been compared to experimental observations which can itself have errors associated with them which have not been
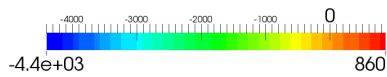
30
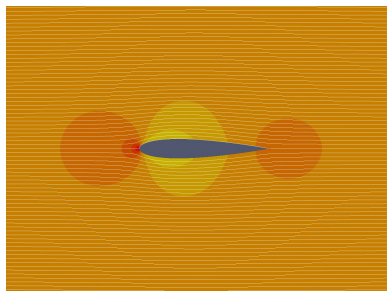
(a) $\alpha = 0°$
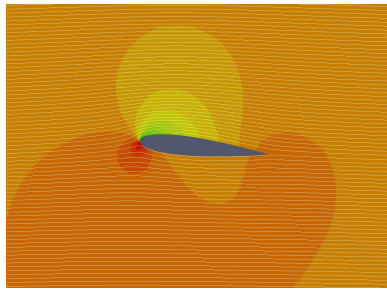


(b) $\alpha = 6°$
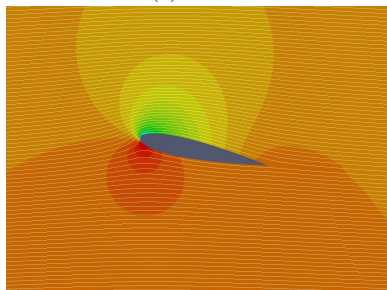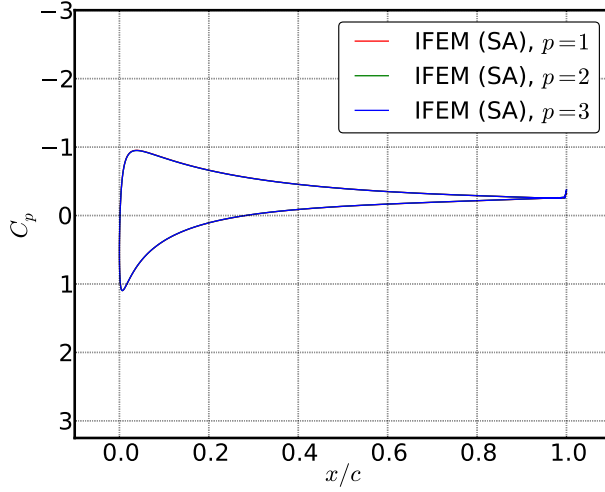


(c) $\alpha = 12°$



(d) Common legend

Figure 21: NACA0015: Pressure contours with streamlines around the airfoil for different angles of attack.

taken into account while a comparison is being made. There is definitely a need for more accurate experiments with quantified uncertainties and errors.

- In spite of some shortfalls the results from our study give a promising

(a) Grid B0, $Re = 250$, $\alpha = 12°$
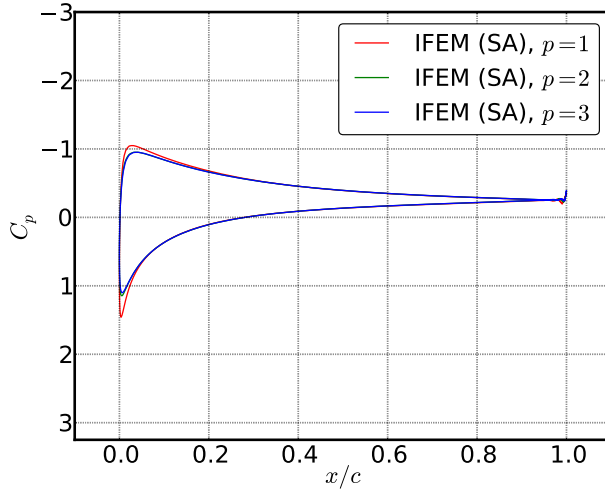


(b) Grid B3, $Re = 250$, $\alpha = 12°$

Figure 22: NACA0015: Surface pressure distributions for $Re = 250$.

outlook for further work towards fluid-structure interaction simulations of wind turbine blades using the developed isogeometric finite element Navier-Stokes solver IFEM. The possibility to use RANS-based turbulence

model in addition to VMS and LES can make the methodology attractive to a wider community, many of whom will be interested in quick results. In particular, 2D airfoil sections as studied here can be coupled through a beam element in a strip theory approach as in [10] and [8].

However, flow around an airfoil, particularly at higher angles of attack, is characterized by three-dimensional flow phenomena like vorticity fluctuation and vortex stretching. A combination of a RANS approach and two-dimensional simulations suppresses all the three-dimensional flow phenomena. Even in three-dimensional flow simulations, owing to the diffusive nature of any RANS model, these phenomena will remain unresolved. An LES or VMS approach will be more suited to accurately model such flow. Weak enforcement of boundary conditions, such as in [38], appears a promising proposition as it is computationally less demanding and stable compared to the more conventional approach.

## 6. Acknowledgment

## References

[1] EWEA, Wind in our sails, Tech. rep., European Wind Energy Association (2011).

[2] EWEA, Wind in power - 2013 European statistics, Tech. rep., European Wind Energy Association (2014).

[3] M. Hansen, J. Sørensen, S. Voutsinas, N. Sørensen, H. Madsen, State of the art in wind turbine aerodynamics and aeroelasticity, Progress in Aerospace Sciences 42 (4) (2006) 285–330.

[4] M.-C. Hsu, Y. Bazilevs, Fluid-structure interaction modeling of wind turbines: Simulating the full machine, Computational Mechanics 50 (6) (2012) 821–833.

[5] Y. Bazilevs, M.-C. Hsu, J. Kiendl, R. Wüchner, K.-U. Bletzinger, 3D simulation of wind turbine rotors at full scale. Part II: Fluid-structure interaction modeling with composite blades, International Journal for Numerical Methods in Fluids 65 (1-3) (2011) 236–253.

[6] C. B. Jenssen, T. Kvamsdal, K. M. Okstad, J. Amundsen, Parallel methods for fluid-structure interaction, in: B. Kågström, J. Dongarra, E. Elmroth, J. Waśniewski (Eds.), Applied Parallel Computing Large Scale Scientific and Industrial Problems, Vol. 1541 of Lecture Notes in Computer Science, Springer Berlin Heidelberg, 1998, pp. 263–274.

[7] C. B. Jenssen, T. Kvamsdal, Computational methods for FSI-simulalations of slender bridges on high performance computers, in: T. Kvamsdal (Ed.), Computational Methods for Fluid-Structure Interactions, Tapir Publisher, Trondheim, 1999, pp. 31–40.

[8] T. Kvamsdal, C. B. Jenssen, K. M. Okstad, J. Amundsen, Fluid-structure interactions for structural design, in: T. Kvamsdal (Ed.), Computational Methods for Fluid-Structure Interactions, Tapir Publisher, Trondheim, 1999, pp. 211–238.

[9] I. Enevoldsen, C. Pederson, S. Hansen, L. Thorbek, T. Kvamsdal, Computational wind simulations for cable-supported bridges, in: A. Larsen (Ed.), Wind Engineering into the 21st Century, Vol. 2, Balkema, Rotterdam, The Netherlands, 1999, pp. 1265–1270.

[10] K. Herfjord, S. O. Drange, T. Kvamsdal, Assessment of vortex-induced vibrations on deepwater risers by considering fluid-structure interaction, Journal of Offshore Mechanics and Arctic Engineering 121 (4) (1999) 207–212.

[11] K. Herfjord, G. Olsen, T. Kvamsdal, K. M. Okstad, Fluid–Structure Interaction in the case of Two Independent Cylinders in Vortex Induced Vibrations (VIV), International Journal of Applied Mechanics and Engineering 7 (2002) 65–83.

[12] T. Hughes, J. Cottrell, Y. Bazilevs, Isogeometric analysis: CAD, finite elements, NURBS, exact geometry and mesh refinement, Computer Methods in Applied Mechanics and Engineering 194 (39-41) (2005) 4135–4195.

[13] J. A. Cottrell, T. J. Hughes, Y. Bazilevs, Isogeometric analysis: toward integration of CAD and FEA, Wiley, Chichester, 2009.

[14] Y. Bazilevs, M.-C. Hsu, I. Akkerman, S. Wright, K. Takizawa, B. Henicke, T. Spielman, T. Tezduyar, 3D simulation of wind turbine rotors at full scale. Part I: Geometry modeling and aerodynamics, International Journal for Numerical Methods in Fluids 65 (1-3) (2011) 207–235.

[15] Y. Bazilevs, M.-C. Hsu, M. Scott, Isogeometric fluid-structure interaction analysis with emphasis on non-matching discretizations, and with application to wind turbines, Computer Methods in Applied Mechanics and Engineering 249-252 (2012) 28–41.

[16] K. Takizawa, D. Montes, S. McIntyre, T. Tezduyar, Space-time VMS methods for modeling of incompressible flows at high Reynolds numbers, Mathematical Models and Methods in Applied Sciences 23 (2) (2013) 223–248.

[17] K. Nordanger, R. Holdahl, A. M. Kvarving, A. Rasheed, T. Kvamsdal, Implementation and comparison of three isogeometric Navier-Stokes solvers applied to simulation of flow past a fixed 2D NACA0012 airfoil at high Reynolds number, Computer Methods in Applied Mechanics and Engineering 284 (2015) 664–688.

[18] P. Spalart, S. Allmaras, One-equation turbulence model for aerodynamic flows, Recherche aerospatiale 1 (1994) 5–21.

[19] K. Valen-Sendstad, A. Logg, K.-A. Mardal, H. Narayanan, M. Mortensen, A Comparison of Some Common Finite Element Schemes for the Incompressible Navier-Stokes Equations, Vol. 84 of Lecture Notes in Computational Science and Engineering, Springer, 2012, Ch. 21, pp. 395–418.

[20] P. Minev, A stabilized incremental projection scheme for the incompressible Navier-Stokes equations, International Journal for Numerical Methods in Fluids 36 (4) (2001) 441–464.

[21] E. N. Jacobs, K. E. Ward, R. M. Pinkerton, The characteristics of 78 related airfoil sections from tests in the variable-density wind tunnel, Tech. rep., National Advisory Committee for Aeronautics (1933).

[22] F. Brezzi, On the existence, uniqueness and approximation of saddle-point problems arising from Lagrangian multipliers, Rev. Francaise Automat. Informat. Recherche Operationelle Ser Rouge 8.

[23] A. J. Chorin, Numerical solution of the Navier-Stokes equations, Mathematics of Computation 22 (1968) 745–762.

[24] R. Temam, Sur l'approximation de la solution des equations de navier-stokes par la methode des pas fractionnaires (ii), Archive for Rational Mechanics and Analysis 33 (5) (1969) 377–385.

[25] J. Guermond, P. Minev, J. Shen, An overview of projection methods for incompressible flows, Computer Methods in Applied Mechanics and Engineering 195 (44-47) (2006) 6011–6045.

[26] L. Timmermans, P. Minev, F. Van De Vosse, An approximate projection scheme for incompressible flow using spectral elements, International Journal for Numerical Methods in Fluids 22 (7) (1996) 673–688.

[27] J. Guermond, J. Shen, On the error estimates for the rotational pressure-correction projection methods, Mathematics of Computation 73 (248) (2004) 1719–1737.

[28] S. R. Allmaras, F. T. Johnson, P. R. Spalart, Modifications and clarifications for the implementation of the Spalart-Allmaras turbulence model, in: ICCFD7 Proceedings, 2012.

[29] R. Bartels, J. Beatty, B. Barsky, An Introduction to Splines for Use in Computer Graphics and Geometric Modeling, Morgan Kaufmann Series in Computer Graphics and Geometric Modeling, Morgan Kaufmann, 1987.

[30] S. A. Coons, Surfaces for computer-aided design of space forms, Tech. Rep. MAC-TR-41, Cambridge, MA, USA (1967).

[31] B. Smith, P. Bjørstad, W. Gropp, Domain Decomposition: Parallel Multilevel Methods for Elliptic Partial Differential Equations, Cambridge University Press, 2004.

[32] S. Balay, S. Abhyankar, M. F. Adams, J. Brown, P. Brune, K. Buschelman, V. Eijkhout, W. D. Gropp, D. Kaushik, M. G. Knepley, L. C. McInnes, K. Rupp, B. F. Smith, H. Zhang, PETSc Web page, `http://www.mcs.anl.gov/petsc` (2014).

[33] M. Heroux, R. Bartlett, V. Howle, R. Hoekstra, J. Hu, T. Kolda, R. Lehoucq, K. Long, R. Pawlowski, E. Phipps, A. Salinger, H. Thornquist, R. Tuminaro, J. Willenbring, A. Williams, K. Stanley, An overview of the Trilinos project, ACM Transactions on Mathematical Software 31 (3) (2005) 397–423.

[34] Y. Saad, Iterative Methods for Sparse Linear Systems, 2nd Edition, Society for Industrial and Applied Mathematics, Philadelphia, PA, USA, 2003.

[35] P. Knupp, Achieving finite element mesh quality via optimization of the Jacobian matrix norm and associated quantities. Part II - A framework for volume mesh optimization and the condition number of the Jacobian matrix, International Journal for Numerical Methods in Engineering 48 (8) (2000) 1165–1185.

[36] R. E. Sheldal, P. C. Klimas, Aerodynamic characteristics of seven symmetrical airfoil sections through 180-degree angle of attack for use in aerodynamic analysis of vertical axis wind turbines, Tech. Rep. SAND80-2114, Sandia National Laboratories (March 1981).

[37] K. W. McAlister, R. K. Takahashi, NACA 0015 wing pressure and trailing vortex measurements, NASA Technical Paper 3151, National Aeronautics and Space Administration, aVSCOM technical report 91-A-003 (1991).

[38] Y. Bazilevs, T. Hughes, Weak imposition of Dirichlet boundary conditions in fluid mechanics, Computers and Fluids 36 (1) (2007) 12–26.

# Paper II

## Implementation and comparison of three isogeometric Navier-Stokes solvers applied to simulation of flow past a fixed 2D NACA0012 airfoil at high Reynolds number

Knut Nordanger, Runar Holdahl, Arne Morten Kvarving, Adil Rasheed and Trond Kvamsdal

# Paper II

# Implementation and comparison of three isogeometric Navier–Stokes solvers applied to simulation of flow past a fixed 2D NACA0012 airfoil at high Reynolds number

Knut Nordanger[a],[*], Runar Holdahl[b], Arne Morten Kvarving[b], Adil Rasheed[b], Trond Kvamsdal[a],[b]

[a] *Department of Mathematical Sciences, Norwegian University of Science and Technology, NO-7491 Trondheim, Norway*
[b] *SINTEF ICT, Department of Applied Mathematics, Postboks 4760 Sluppen, NO-7465 Trondheim, Norway*

---

**Highlights**

- Comparison of three isogeometric, incompressible Navier–Stokes solvers.
- Simulations of flow around a NACA0012 airfoil at $Re = 3 \times 10^6$.
- Lift, drag and pressure coefficients compared to experiments and simulations.
- Increasing the element order from 1 to 2 generally improves the results.
- For $p = 2$ the Chorin solver is faster than the VMS and coupled formulation solvers.

---

**Abstract**

Implementation of three different Navier–Stokes solvers in an isogeometric finite element framework is presented in this paper. The three solvers *Chorin projection method* and *Coupled formulation*, both with the Spalart–Allmaras turbulence model, and *Variational Multiscale (VMS) method* have been applied to simulate flow past a two-dimensional NACA0012 airfoil at a high Reynolds number ($Re = 3 \times 10^6$) for four different angles of attack. The predicted flow characteristics have been compared and the effects of increasing the order of the spline element on the accuracy of prediction and computational efficiency are evaluated. In this study it turns out that flow separation does not take place up to an angle of attack of $16°$. Up to this angle of attack all three solvers predict similar results in good agreement with each other and with available experimental results. However, a big spread in lift and drag coefficients is observed in the stall regime. Our study also shows that for linear spline elements all three solvers are computationally similar. For quadratic spline elements the Chorin solver compares favorably to the others based on the results presented here.
© 2014 Elsevier B.V. All rights reserved.

*Keywords:* Isogeometric analysis; NACA0012 airfoil; Chorin projection method; Spalart–Allmaras; Variational Multiscale

---

[*] Corresponding author.
*E-mail addresses:* knut.nordanger@math.ntnu.no (K. Nordanger), runar.holdahl@sintef.no (R. Holdahl), arne.morten.kvarving@sintef.no (A.M. Kvarving), adil.rasheed@sintef.no (A. Rasheed), trond.kvamsdal@math.ntnu.no (T. Kvamsdal).

## 1. Introduction

Renewable energy is a growing sector with promising prospects of generating energy from wind as an important driving force. Therefore, being able to simulate flow around wind turbines is becoming increasingly important as the demand for larger and larger offshore wind turbines is growing. Larger turbines present many new challenges which cannot easily be addressed by traditional engineering methods.

Many methods exist for computing flow around wind turbines. Today an increased focus is put on the overall simulation efficiency, i.e. the time consumption related to modeling, analysis and interpretation of results. In particular, the lack of interoperability between modeling using modern Computer Aided Design (CAD) systems and classical finite element analysis programs is a bottleneck. To address this bottleneck the concept of isogeometric analysis was introduced by Thomas J.R. Hughes and co-workers [1,2]. This concept is characterized by using splines, i.e. B-splines or non-rational uniform B-splines (NURBS), as basis functions in the finite element analysis as well as in the CAD system. In turn, this opens up for exact geometric modeling, which can be of utmost importance when it comes to modeling aerodynamically shaped objects like airfoils. Furthermore, isogeometric analysis gives better accuracy per degree-of-freedom than more traditional methods.

The computational efficiency of isogeometric analysis methods for solving the incompressible Navier–Stokes equations is a current research topic. Aiming at attaining a solution as quickly as possible within a desired, acceptable accuracy is an obvious goal in all design situations. The pioneers in isogeometric analysis, such as Yuri Bazilevs among others, have developed coupled formulations based on variational multiscale stabilization (VMS) [3] and VMS turbulence models based on the work by Victor Calo [4]. These models have been further developed in [5].

Designing efficient linear solvers for fully coupled formulations of the incompressible Navier–Stokes flows as mentioned above is very challenging because of the coupling of the velocity and pressure unknowns through the incompressibility constraint. Projection methods can be a more efficient alternative for time-dependent problems since one only needs to solve several decoupled systems of parabolic or elliptic equations at each timestep. Standard Krylov subspace methods like the conjugate gradient method or GMRES with efficient preconditioners like multigrid or domain decomposition can then be used to solve the linear systems. The main drawback of projection methods is that high-order methods are hard to design and analyze due to the introduction of additional unphysical boundary conditions.

Valen-Sendstad et al. [6] studied the performance of six different solvers for incompressible flow and among them a Chorin projection method (incremental pressure correction) and a least-squares stabilized Galerkin scheme. From their study they conclude that the incremental pressure scheme was the most efficient and accurate method. However, this depends of course on the problem at hand. They looked at low Reynolds number cases, whereas our interest lies in high Reynolds flow.

In this paper we intend to highlight some aspects related to the quality of computed solutions and computational efficiency of three isogeometric incompressible Navier–Stokes solvers applied to a two-dimensional problem. The first solver is based on a Chorin projection method (incremental pressure correction) along with the Spalart–Allmaras turbulence model [7], the second is based on a coupled formulation of the Navier–Stokes equations combined with the Spalart–Allmaras turbulence model and the third is a variational multiscale approach [3]. Common to all methods is that the equations are discretized using linear and quadratic spline elements. As a test case we have chosen flow past a fixed two-dimensional NACA0012 airfoil, which is considered to be a relevant airfoil for wind turbine application.

The paper is organized as follows: Section 2 starts with a brief description of the family of NACA airfoils followed by the relevant governing flow equations. Then we describe the two different types of turbulence modeling approaches that we have used as well as the implementation of the Chorin and coupled Navier–Stokes solvers. Our quantities of interest are lift, drag and pressure coefficients, so their expressions are also presented. Section 3 describes the simulation setup and other simulation parameters used in the study. Finally, in Section 4 the results from the three different solvers for linear and quadratic spline elements are compared and their computational efficiencies are evaluated. The paper ends with the main conclusion of the study in Section 5.

## 2. Theory

### 2.1. Symmetric 4-digit NACA airfoils

The 4-digit NACA airfoils denote a series of airfoil shapes developed by the National Advisory Committee for Aeronautics (NACA). All NACA airfoils are identified by four digits and are usually written in the form NACA
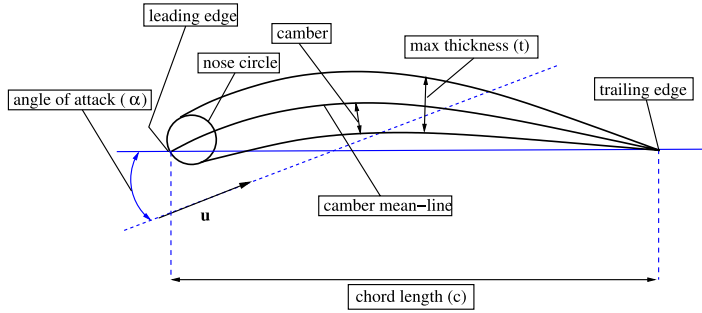
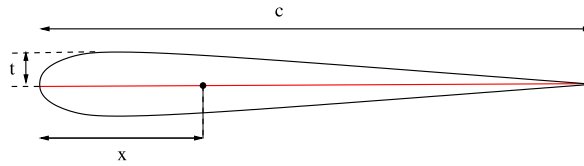Fig. 1. Design parameters for NACA XXXX airfoil.



Fig. 2. Symmetric NACA 00XX airfoil.

XXXX where the first digit is the maximum camber as a percentage of the chord, the second digit is the distance of maximum camber from the leading edge in percent of the chord and the last two digits are the maximal thickness as a percentage of the chord. See Fig. 1 for a description of the different design parameters of the NACA airfoil. Symmetric NACA airfoils have no camber and are only characterized by the two last digits, i.e. the ratio between the maximal thickness $t$ and the chord length $c$, see Fig. 2. The shapes of these airfoils (NACA 00XX) are given by the analytical formula

$$y_t = 5tc \left[ 0.2969\sqrt{\frac{x}{c}} - 0.1260\left(\frac{x}{c}\right) - 0.3516\left(\frac{x}{c}\right)^2 + 0.2843\left(\frac{x}{c}\right)^3 - 0.1015\left(\frac{x}{c}\right)^4 \right], \tag{1}$$

where $y_t$ is the distance from the centerline, $t$ is the maximal thickness from centerline, $c$ is the chord length and $x$ is the position along the chord from 0 to $c$. Eq. (1) does not give a closed curve for the wing profile since $y$ is not exactly 0 for $x = c$. To get a closed curve the last coefficient is modified to get

$$y_t = 5tc \left[ 0.2969\sqrt{\frac{x}{c}} - 0.1260\left(\frac{x}{c}\right) - 0.3516\left(\frac{x}{c}\right)^2 + 0.2843\left(\frac{x}{c}\right)^3 - 0.1036\left(\frac{x}{c}\right)^4 \right]. \tag{2}$$

This formula has been used to approximate the NACA0012 wing profile in the numerical investigation presented in this paper.

### 2.2. Governing equations

Subsonic, viscous flows is mathematically described by the incompressible Navier–Stokes equations given by

$$\rho\frac{\partial \boldsymbol{u}}{\partial t} + \rho\left(\boldsymbol{u}\cdot\nabla\right)\boldsymbol{u} - \nabla\cdot\boldsymbol{\sigma}\left(\boldsymbol{u},\,p\right) = \rho\boldsymbol{f} \quad \text{in } \Omega$$
$$\nabla\cdot\boldsymbol{u} = 0 \quad \text{in } \Omega. \tag{3}$$

Here, $\Omega \in \mathbb{R}^d$, $d = 2, 3$, is a suitable, sufficiently regular and open domain, $\rho$ is the constant fluid density, $p$ is the pressure, $\boldsymbol{u}$ is the fluid velocity vector and $\boldsymbol{f}$ is a volumetric body force. The Cauchy stress tensor can be written as

$$\boldsymbol{\sigma}\left(\boldsymbol{u},\,p\right) = -p\boldsymbol{I} + 2\mu\boldsymbol{\epsilon}\left(\boldsymbol{u}\right),$$

where $\boldsymbol{I}$ is the identity tensor, $\mu$ the dynamic viscosity and the strain rate $\boldsymbol{\epsilon}$ is defined as

$$\boldsymbol{\epsilon}(\boldsymbol{u}) = \frac{1}{2}\left(\nabla \boldsymbol{u} + (\nabla \boldsymbol{u})^T\right).$$

We also define $\partial \Omega = \Gamma = \Gamma_D \cup \Gamma_N \cup \Gamma_M$ where $\Gamma_D$ are the boundaries with Dirichlet conditions, $\Gamma_N$ are the boundaries with Neumann conditions and $\Gamma_M$ are the boundaries with mixed conditions. Mixed boundary conditions are used in situations where the normal velocity component is given, usually zero, together with the tangential stresses, and can model symmetry planes and slip or friction conditions.

The variational formulation is expressed as: Find $(\boldsymbol{u}, p) \in \boldsymbol{U} \times Q$ such that

$$\left(\rho \frac{\partial \boldsymbol{u}}{\partial t}, \boldsymbol{v}\right) + c(\boldsymbol{u}; \boldsymbol{u}, \boldsymbol{v}) + b(p, \boldsymbol{v}) + a(\boldsymbol{u}, \boldsymbol{u}) + b(q, \boldsymbol{u}) = f(\boldsymbol{v}) \quad (\boldsymbol{v}, q) \in \boldsymbol{V} \times Q, \tag{4}$$

where we have defined the spaces

$$\boldsymbol{U} = \boldsymbol{H}_{\Gamma_D, \Gamma_M^{\perp}}(\Omega) = \left\{\boldsymbol{v} \in \boldsymbol{H}^1(\Omega) \mid \boldsymbol{v} = \boldsymbol{u_D} \text{ on } \Gamma_D \text{ and } \boldsymbol{v} \cdot \boldsymbol{n} = u_{\perp} \text{ on } \Gamma_M\right\}$$

$$\boldsymbol{V} = \boldsymbol{H}_{\Gamma_D, \Gamma_M^{\perp};0}(\Omega) = \left\{\boldsymbol{v} \in \boldsymbol{H}^1(\Omega) \mid \boldsymbol{v} = 0 \text{ on } \Gamma_D \text{ and } \boldsymbol{v} \cdot \boldsymbol{n} = 0 \text{ on } \Gamma_M\right\}$$

$$Q = L^2(\Omega),$$

where $\boldsymbol{u_D}$ and $u_{\perp}$ both are given functions and $\boldsymbol{n}$ is the unit outer normal on $\Gamma$, and the forms

$$a(\boldsymbol{u}, \boldsymbol{v}) = 2 \int_{\Omega} \mu \boldsymbol{\epsilon}(\boldsymbol{u}) : \boldsymbol{\epsilon}(\boldsymbol{v}) \, d\boldsymbol{x}$$

$$b(q, \boldsymbol{v}) = -\int_{\Omega} (\nabla \cdot \boldsymbol{v}) q \, d\boldsymbol{x}$$

$$c(\boldsymbol{w}; \boldsymbol{u}, \boldsymbol{v}) = \int_{\Omega} \rho (\boldsymbol{w} \cdot \nabla) \boldsymbol{u} \cdot \boldsymbol{v} \, d\boldsymbol{x}$$

$$f(\boldsymbol{v}) = \int_{\Omega} \rho \boldsymbol{f} \cdot \boldsymbol{v} \, d\boldsymbol{x} + \int_{\Gamma_N} \boldsymbol{t} \cdot \boldsymbol{v} \, d\boldsymbol{s},$$

where $\boldsymbol{t} = \boldsymbol{\sigma} \cdot \boldsymbol{n}$ is the traction vector on $\Gamma$.

### 2.2.1. Isogeometric finite element approximation

The isogeometric finite element method approximates the solution by using a spline basis of polynomial order $p$ and regularity $C^{p-1}$, whereas $C^0$ Lagrange polynomials of low order (typically $p = 1$ or $p = 2$) are used in traditional finite element formulations. Our approach is based on a conforming finite element approximation, i.e.

$$\boldsymbol{U}_h \subset \boldsymbol{U}, \qquad \boldsymbol{V}_h \subset \boldsymbol{V}, \qquad Q_h \subset Q.$$

The discrete approximation spaces $\boldsymbol{U}_h, \boldsymbol{V}_h, Q_h$ are chosen as the isogeometric finite element spaces. This gives the semi-discrete formulation of the variational problem stated in Eq. (4): Find $(\boldsymbol{u}_h, p_h) \in \boldsymbol{U}_h \times Q_h$ such that

$$\left(\rho \frac{\partial \boldsymbol{u}_h}{\partial t}, \boldsymbol{v}_h\right) + c(\boldsymbol{u}_h; \boldsymbol{u}_h, \boldsymbol{v}_h) + a(\boldsymbol{u}_h, \boldsymbol{u}_h) + b(p, \boldsymbol{v}_h) + b(q, \boldsymbol{u}_h) = f(\boldsymbol{v}_h)$$

for all $(\boldsymbol{v}_h, q_h) \in \boldsymbol{V}_h \times Q_h$.

Herein, we have developed a block-structured B-spline isogeometric finite element approximation of the Navier–Stokes equations described above. To construct a B-spline basis for a domain $\Omega$ which is subdivided into a number of patches (a patch is equivalent to a block) $\Omega_e$ such that $\Omega = \cup_{e=1}^{N} \Omega_e$ we associate for each patch a knot-vector in each coordinate direction

$$\Xi_k^e = \left\{\xi_{1,k}^e, \xi_{2,k}^e, \dots, \xi_{n_k^e + p_k^e + 1}^e\right\}$$

for $k = 1, \dots, d$. The B-spline basis for patch $\Omega_e$ on the parametric domain $\hat{\Omega} = (0, 1)^d$ is written as $\hat{\boldsymbol{\mathcal{S}}}_{\boldsymbol{\alpha}^e}^{\boldsymbol{p}^e}$ where the multi-indices $\boldsymbol{\alpha}^e = \left(\alpha_1^e, \dots, \alpha_d^e\right)$ and $\boldsymbol{p}^e = \left(p_1^e, \dots, p_d^e\right)$ denote the regularity and order for the basis in each

coordinate directions, respectively. The corresponding basis for the physical domain $\Omega_e$ can be expressed using the coordinate mapping $\phi_e : \hat{\Omega} \to \Omega_e$ as

$$\mathcal{S}_{\boldsymbol{\alpha}^e}^{\boldsymbol{p}^e} = \left\{ v_h \mid v_h \circ \boldsymbol{\phi}_e \in \hat{\mathcal{S}}_{\boldsymbol{\alpha}^e}^{\boldsymbol{p}^e} \right\}.$$

If the variational formulation allows a discontinuous approximation the spline finite element basis for the domain $\Omega$ can be defined as

$$\mathcal{S}_h = \left\{ v_h \mid v_{h|\Omega_e} \in \mathcal{S}_{\boldsymbol{\alpha}^e}^{\boldsymbol{p}^e} \right\}.$$

If we assume that the knot-vectors and geometrical mapping $\boldsymbol{\phi}_e$ for all the patches are consistent on common edges and faces we can define a continuous basis

$$\mathcal{S}_h = \left\{ v_h \in C(\Omega) \mid v_{h|\Omega_e} \in \mathcal{S}_{\boldsymbol{\alpha}^e}^{\boldsymbol{p}^e} \right\}.$$

We use the same basis for the geometry as for the discretization of the velocity and the pressure.

### 2.3. Turbulence modeling

High Reynolds number flows involving reasonably complex geometries like airfoils are mostly turbulent and require turbulence modeling since their explicit resolution using Direct Numerical Simulation (DNS) is still computationally intractable. Thus one is left with either of the two choices Reynolds Averaged Navier–Stokes (RANS) or Large Eddy Simulation (LES) based models. In the former all the scales are modeled while in the latter only the small isotropic scales are modeled while the larger energy-containing scales are resolved. In the present study we use the Spalart–Allmaras model and variational multiscale model which can be seen to lie in the category of RANS and LES classes. A brief discussion of the models is presented in the following subsections.

#### 2.3.1. Spalart–Allmaras model

In RANS models the flow is divided into a time-averaged and fluctuating part known as *Reynolds decomposition*

$$\boldsymbol{u} = \bar{\boldsymbol{u}} + \boldsymbol{u}',$$
$$p = \bar{p} + p',$$

where $\bar{\boldsymbol{u}}$, $\bar{p}$ are the time-averaged components while the $\boldsymbol{u}'$, $p'$ are the fluctuations in time. The Navier–Stokes equations are then time-averaged to give an equation for the time-averaged quantities. Assuming that the time average of the fluctuation part is zero, the Reynolds averaged Navier–Stokes equations can be written as

$$\rho \left( \frac{\partial \bar{\boldsymbol{u}}}{\partial t} + (\bar{\boldsymbol{u}} \cdot \nabla)\bar{\boldsymbol{u}} \right) - \nabla \cdot \left( \boldsymbol{\sigma}(\bar{\boldsymbol{u}}, \bar{p}) + \rho \langle \boldsymbol{u}' \otimes \boldsymbol{u}' \rangle \right) = \rho \bar{\boldsymbol{f}},$$
$$\nabla \cdot \bar{\boldsymbol{u}} = 0,$$

where $\langle \cdot \rangle$ is the averaging operator and $(\langle \boldsymbol{u}' \otimes \boldsymbol{u}' \rangle)_{ij} = \langle u_i' u_j' \rangle$. The equations have a form similar to the original Navier–Stokes equations except for the last term on the left hand side of the momentum equation which results from the time averaging and acts similar to the viscous stress term and is therefore called the *Reynolds stress* term. The Reynolds stress tensor is symmetric and introduces new unknowns, 6 in 3D and 3 in 2D, and therefore additional equations are required to close the system. In the present study we employ the Spalart–Allmaras model [7]. This model solves a scalar transport equation for the modified kinematic viscosity parameter $\tilde{\nu}$. The formulation of the model is the transport equation

$$\frac{\partial \tilde{\nu}}{\partial t} + \boldsymbol{u} \cdot \nabla \tilde{\nu} = c_{b1} \tilde{S} \tilde{\nu} + \frac{1}{\sigma} \left( \nabla \cdot (\nu + \tilde{\nu}) \nabla \tilde{\nu} + c_{b2} |\nabla \tilde{\nu}|^2 \right) - c_{w1} f_w \left( \frac{\tilde{\nu}}{d} \right)^2.$$

Here $\nu = \mu/\rho$ denotes the laminar kinematic viscosity, $\boldsymbol{u}$ the fluid velocity and $d$ the distance from a given point to the closest solid wall. From the modified viscosity the eddy viscosity can be computed as

$$\nu_t = \tilde{\nu} f_{v1}, \quad f_{v1} = \frac{\tilde{\nu}^3}{\tilde{\nu}^3 + \nu^3 c_{v1}^3}.$$

Modifications of the original model for the modified vorticity were published in [8]. The modified vorticity $\tilde{S}$ is now given by

$$\overline{S} = \frac{\tilde{\nu}}{\kappa^2 \cdot d^2} f_{v2}, \quad f_{v2} = 1 - \frac{\tilde{\nu}}{\nu + \tilde{\nu} f_{v1}}$$

where $S$ represents the magnitude of the vorticity and $d$ the distance to the closest wall, and

$$\tilde{S} = \begin{cases} S + \overline{S} & : \overline{S} \geq -c_{v2}S \\ S + \dfrac{S\left(c_{v2}^2 S + c_{v3}\overline{S}\right)}{(c_{v3} - 2c_{v2})S - \overline{S}} & : \overline{S} < -c_{v2}S \end{cases}$$

with $c_{v2} = 0.7$ and $c_{v3} = 0.9$. The new modified vorticity $\tilde{S}$ does not have the possibility of becoming negative and thus avoids a possible problem of disrupting other Spalart–Allmaras functions. Furthermore we have for the destruction term

$$f_w = g \left[ \frac{1 + c_{w3}^6}{g^6 + c_{w3}^3} \right]^{1/6}$$

$$g = r + c_{w2}(r^6 - r)$$

$$r = \frac{\tilde{\nu}}{\tilde{S}\kappa^2 d^2}.$$

In the original work [7] the following values were given for the constants appearing in the model

$$c_{b1} = 0.1355, \quad c_{b_2} = 0.622, \quad c_{w_2} = 0.3, \quad c_{w3} = 2,$$
$$\sigma = 2/3, \quad c_{v1} = 7.1, \quad \kappa = 0.41.$$

To relax the need for high resolution in the mesh close to the wall the law-of-the-wall parametrization given in [8] is introduced. Here the turbulent viscosity close to the wall is approximated by an analytical expression derived for idealized flow conditions. The use of the law-of-the-wall parametrization allows for a much coarser resolution close to the wall, typically a wall distance $y^+ \sim 10$–30. Here, $y^+$ is the non-dimensional wall distance defined in terms of the friction or shear stress velocity $u_\tau$ as

$$y^+ = \frac{u_*}{\nu} \quad \text{with } u_* = \sqrt{\frac{\tau_w}{\rho}}$$

where the wall shear stress $\tau_w$ is given by

$$\tau_w = \mu \left[ \frac{\partial \boldsymbol{u}}{\partial \boldsymbol{n}} \right]_{y=0} = \mu \left[ \nabla \boldsymbol{u} \cdot \boldsymbol{n} \right]_{y=0}.$$

The starting point for the derivation is the following simple solution of the SA model

$$\tilde{\nu} = \kappa u_\tau y, \quad \tilde{S} = \frac{u_\tau}{\kappa y}, \tag{5}$$

where $y$ is the distance from the wall. The shear stress velocity can be written as $u_\tau = u_{\text{tan}}/u^+$, where $u_{\text{tan}}$ is the tangential velocity and $u^+$ the dimensionless velocity. By using the common assumptions for the derivation of wall laws, i.e. incompressible flow, zero pressure gradient, constant velocity in the outer region, negligible advection in the boundary layer, the following simplified expression for the wall law is derived

$$u^+(y^+) = \bar{B} + c_1 \log\left((y^+ + a_1)^2 + b_1^2\right) - c_2 \log\left((y^+ + a_2)^2 + b_2^2\right)$$

$$- c_3 \operatorname{atan2}[y^+ + a_1, b_1] - c_4 \operatorname{atan2}[y^+ + a_2, b_2]. \tag{6}$$

The atan2 function can be defined from the standard arctan function as

$$
\text{atan2}(y, x) =
\begin{cases}
\arctan\left(\dfrac{y}{x}\right), & x > 0, \\[2mm]
\arctan\left(\dfrac{y}{x}\right), & y \geq 0, \; x < 0, \\[2mm]
\arctan\left(\dfrac{y}{x}\right), & y < 0, \; x < 0, \\[2mm]
\dfrac{\pi}{2}, & y > 0, \; x = 0, \\[2mm]
-\dfrac{\pi}{2}, & y < 0, \; x = 0, \\[2mm]
\text{undefined}, & y = 0, \; x = 0.
\end{cases}
$$

Since the mean velocity $u^+$ is a function of the normalized wall normal distance $y^+$ the wall law can be explicitly evaluated and there is no need for non-linear Newton iterations. The value of the constants in Eq. (6) are given by $\bar{B} = 5.0333908790505579$ and

$$
\begin{aligned}
&a_1 = 8.148221580024245, & &b_1 = 7.4600876082527945, \\
&a_2 = -6.9287093849022945, & &b_2 = 7.468145790401841, \\
&c_1 = 2.5496773539754747, & &c_2 = 1.3301651588535228, \\
&c_3 = 3.599459109332379, & &c_4 = 3.6397531868684494.
\end{aligned}
$$

When using the wall law a no-slip condition is used for the fluid velocity and the modified vorticity is set to zero on the walls. A Dirichlet condition based on the wall law is imposed on the near-wall nodes. On the inflow boundaries $\tilde{v}_{\text{in}} = 5v$ is used, whilst a homogeneous Neumann boundary condition is applied on the outflow boundaries and symmetry planes,

$$
\frac{\partial \tilde{v}}{\partial \boldsymbol{n}} = \nabla \tilde{v} \cdot \boldsymbol{n} = 0.
$$

The turbulent viscosity field computed is then used to model the Reynolds stresses [7] through the constitutive relation

$$
-\langle u_i' u_j' \rangle = 2 v_t \epsilon_{ij}
$$

and thus to close the problem.

### 2.3.2. Variational multiscale

The variational multiscale formulation is similar to a LES model for fluid flow but without the concept of an eddy viscosity. The starting point for the derivation of the variational multiscale formulation of the incompressible Navier–Stokes equations is the variational formulation, Eq. (4). To simplify the notation we follow [3] and write $\boldsymbol{U} = (\boldsymbol{u}, p)$ and $\boldsymbol{V} = (\boldsymbol{v}, q)$ for the solutions and test functions, respectively. The corresponding functional spaces are given by

$$
\begin{aligned}
\mathcal{U} &= \mathsf{U} \times \mathsf{Q}, \\
\mathcal{V} &= \mathsf{V} \times \mathsf{Q}.
\end{aligned}
$$

The variational formulation of the incompressible Navier–Stokes problem, Eq. (3), can now be written as

$$
B(\boldsymbol{U}, \boldsymbol{V}) = B_L(\boldsymbol{U}, \boldsymbol{V}) + B_{NL}(\boldsymbol{U}; \boldsymbol{U}, \boldsymbol{V}) = F(\boldsymbol{V}), \tag{7}
$$

where the operator $B$ is split into a linear and a non-linear part as

$$
\begin{aligned}
B_L(\boldsymbol{U}, \boldsymbol{V}) &= \left( \rho \frac{\partial \boldsymbol{u}}{\partial t}, \boldsymbol{v} \right) + b(p, \boldsymbol{v}) + a(\boldsymbol{u}, \boldsymbol{v}) - b(q, \boldsymbol{u}), \\
B_{NL}(\boldsymbol{W}; \boldsymbol{U}, \boldsymbol{V}) &= c(\boldsymbol{w}; \boldsymbol{u}, \boldsymbol{v}),
\end{aligned} \tag{8}
$$

and the linear functional is given as

$$
F(\boldsymbol{V}) = f(\boldsymbol{v}).
$$

Then a decomposition of the solution space $\mathcal{U}$ into a "coarse scale" $\bar{\mathcal{U}}$ and "fine scale" $\mathcal{U}'$ is defined as

$$\mathcal{U} = \bar{\mathcal{U}} \oplus \mathcal{U}'. \tag{9}$$

It is assumed that $\bar{\mathcal{U}}$ is a finite dimensional space which in practical applications will be a numerical approximation space, for instance a finite element space. A unique decomposition (9) is defined by a projection operator $\mathbb{P} : \mathcal{U} \rightarrow \bar{\mathcal{U}}$ such that

$$\bar{U} = \mathbb{P}U,$$
$$U' = U - \bar{U} = (\mathbb{I} - \mathbb{P})U,$$

where $\mathbb{I}$ is the identity operator. The projection operator $\mathbb{P}$ can for example be the $L^2$- or $H^1$-projection onto the coarse space $\bar{\mathcal{U}}$. A similar decomposition is also introduced for the space of test functions $\mathcal{V}$ as

$$\bar{V} = \mathbb{P}V,$$
$$V' = (\mathbb{I} - \mathbb{P})V.$$

Writing the solution and test functions as $\bar{U} + U'$ and $\bar{V} + V'$, respectively, the variational problems (7) reads

$$B(\bar{U} + U', \bar{V} + V') = F(\bar{V} + V').$$

If both $\bar{V}$ and $V'$ are valid test functions for the original variational formulation (7), i.e. if $\bar{\mathcal{V}} \subset \mathcal{V}$ and $\mathcal{V}' \subset \mathcal{V}$, then one can first choose $V' = 0$ and then $\bar{V} = 0$ to get the coarse and fine scale equations

$$B(\bar{U} + U', \bar{V}) = F(\bar{V}),$$
$$B(\bar{U} + U', V') = F(V').$$

The fine scale equation can be rephrased in the form

$$DB_{\bar{U}}(U', V') + B_{NL}(U'; U', V') = \langle R(\bar{U}), V' \rangle_{\mathcal{V}'^*, \mathcal{V}'}$$

where $DB_{\bar{U}}$ is the linearization of $B$ about $\bar{U}$ in the direction of $U'$

$$\begin{aligned} DB_{\bar{U}}(U', V') &= \left. \frac{d}{d\epsilon} B(\bar{U} + \epsilon U', V') \right|_{\epsilon=0} \\ &= B_L(U', V') + B_{NL}(\bar{U}; U', V') + B_{NL}(U'; \bar{U}, V') \end{aligned}$$

and $R(\bar{U})$ is the coarse scale residual lifted to the fine scale by the duality pairing

$$\langle R(\bar{U}), V' \rangle_{\mathcal{V}'^*, \mathcal{V}'} = F(V') - B_L(\bar{U}, V') - B_{NL}(\bar{U}; \bar{U}, V').$$

The fine scale solution can formally be written as a functional of the form

$$U' = F'(\bar{U}, R(\bar{U})),$$

and then the equation for the finite dimensional coarse scale solution $\bar{U}$ can be written as

$$B(\bar{U} + F'(\bar{U}, R(\bar{U})), \bar{V}) = L(\bar{V}).$$

So far no approximations have been introduced, and thus the exact solution of the Navier–Stokes problem, Eq. (7), is given by $U = \bar{U} + U'$. However, in practice we are not able to obtain an analytical expression for the fine scale solution and some kind of approximation must be introduced.

The turbulence modeling concept introduced in [3] is based on approximating the functional $F'$ and thus find an approximate fine scale solution $U'$. The fine scale solution is then substituted into the coarse scale equation which then can be solved for $\bar{U}$. Hence the variational multiscale approach to turbulence modeling can be written as

$$\tilde{U}' = \tilde{F}'(\tilde{\bar{U}}, R(\tilde{\bar{U}})),$$
$$B(\tilde{\bar{U}} + \tilde{F}'(\tilde{\bar{U}}, R(\tilde{\bar{U}}), \bar{V})) = L(\bar{V}),$$

where $\tilde{F}'$ is an approximation to $F'$, and $\tilde{\bar{U}}$ and $\tilde{U}'$ are approximations to $\bar{U}$ and $U'$, respectively. In the turbulence model introduced in [3] the approximation of the fine scale $\tilde{U}'$ is based on

1. The expression of the fine scale solution $U'$ as a perturbation series of the form

$$U' = \epsilon U'_1 + \epsilon^2 U'_2 + \cdots = \sum_{k=1}^{\infty} \epsilon^k U'_k$$

   with $\epsilon = \|R(\bar{U})\|_{\mathcal{V}'^*}$.

2. Truncation of the perturbation series after the first term

$$U' \approx \epsilon U'_1.$$

3. An approximation of the fine scale Green's operator for the linearized Navier–Stokes equations is defined as $\tilde{G}'_{\bar{U}} \approx G'_{\bar{U}}$, and it is used to find an approximate solution for $U_1$.

4. Traditional SUPG and residual based stabilization methods have been shown to represent local approximations of the fine scale Green's operator, see [9–12]. Hence, a simple approximation of the fine scale field can be written as

$$\tilde{U}' \approx -\tau R(\tilde{\bar{U}}), \tag{10}$$

   where the matrix $\tau \in \mathbb{R}^{4\times4}$ can be computed element-wise as the mean value of the fine scale Green's operator over the element. Usually $\tau$ is taken to be a diagonal matrix on the form

$$\tau = \begin{pmatrix} \tau_M I_{3\times3} & \mathbf{0} \\ \mathbf{0} & \tau_C \end{pmatrix}.$$

For more details on the derivation of the variational multiscale formulation of turbulent incompressible flow presented above we refer to Bazilevs et al. [3]. For a detailed study of the fine scale Green's operator for the linear, steady advection–diffusion equation, see Hughes and Sangalli [12].

Substituting the fine scale approximation given by Eq. (10) into the variational formulation given by Eq. (7) gives the following final formulation: Find $U_h \in \mathcal{U}_h$ such that

$$B_h^{ms}(U_h, V_h) = L(V_h) \tag{11}$$

where

$$B_h^{ms}(U_h, V_h) = B(U_h, V_h) + B'_h(U_h, V_h) \tag{12}$$

and the additional terms are given by

$$B'_h(U_h, V_h) = \left( u_h \cdot \nabla v_h + \frac{\nabla q_h}{\rho}, \tau_M r_M(u_h, p_h) \right) + (\rho \nabla \cdot v_h, \tau_C r_c(u_h))$$

$$+ \left( u_h \cdot (\nabla v_h)^T, \tau_M r_M(u_h, p_h) \right) - \left( \frac{\nabla v_h}{\rho}, \tau_M r_M(u_h, p_h) \otimes \tau_M r_M(u_h, p_h) \right). \tag{13}$$

Here $r_M$ and $r_C$ denote the residual of the momentum and continuity equation, that is

$$r_M(u_h, p_h) = \rho \frac{\partial u_h}{\partial t} + \rho u_h \cdot \nabla u_h + \nabla p_h - \mu \Delta u_h - \rho f,$$

$$r_C(u_h) = \nabla \cdot u_h.$$

The non-conservative formulation is used for the definition of the momentum residual in the terms corresponding to the VMS stabilization terms. It is reported in [3] that this has a favorable effect on the stability of the formulation compared with the conservative formulation. We note that the first two terms on the right-hand side of Eq. (13) represent the standard SUPG, pressure and continuity stabilization terms, while the last two terms are unique for the variational multiscale formulation. The variational multiscale turbulence model defined by Eqs. (11)–(13) has been applied to forced homogeneous isotropic turbulence and turbulent channel flows with very good results in [3].

### 2.4. Coupled Navier–Stokes RANS

In this work using a coupled Navier–Stokes solver in a RANS setting is considered. Here one solves the variational problem: Find $\boldsymbol{U}_h \in \mathcal{U}_h$ such that

$$B_h(\boldsymbol{U}_h, \boldsymbol{V}_h) = L(\boldsymbol{V}_h) \tag{14}$$

where

$$B_h(\boldsymbol{U}_h, \boldsymbol{V}_h) = B(\boldsymbol{U}_h, \boldsymbol{V}_h) + B'_h(\boldsymbol{U}_h, \boldsymbol{V}_h) \tag{15}$$

and the additional terms are given by

$$B'_h(\boldsymbol{U}_h, \boldsymbol{V}_h) = \left( \boldsymbol{u}_h \cdot \nabla \boldsymbol{v}_h + \frac{\nabla q_h}{\rho}, \tau_M \boldsymbol{r}_M(\boldsymbol{u}_h, p_h) \right) + (\rho \nabla \cdot \boldsymbol{v}_h, \tau_C r_c(\boldsymbol{u}_h)). \tag{16}$$

This is Eq. (13) without the extra multiscale terms, i.e., the Reynolds-averaged Navier–Stokes equations with SUPG, continuity and pressure stabilization terms, where the Spalart–Allmaras model is used for the Reynolds stress terms.

### 2.5. The Chorin scheme

The projection methods were introduced in the late 1960s by Chorin [13] and Temam [14]. Here one only needs to solve decoupled problems of elliptic equations at each timestep instead of the full coupling of the velocity and pressure [15]. Thus standard Krylov subspace methods like the Conjugate Gradient (CG) method and Generalized Minimal RESidual method (GMRES) can be used to solve the linear systems, and one can readily construct efficient preconditioners. Drawbacks of the projection methods include an inherent splitting error and erroneous numerical boundary conditions for the pressure, causing a reduced convergence order for the pressure and erroneous boundary layers in the velocity.

In order to avoid the inconsistent pressure boundary condition present in many splitting schemes we choose a rotational formulation for the incremental pressure correction scheme as proposed in [16]. This gives us the following formulation

1. Velocity prediction step

$$\frac{\rho}{2\Delta t} \left( 3\bar{\boldsymbol{u}}^{n+1} - 4\boldsymbol{u}^n + \boldsymbol{u}^{n-1} \right) + \rho \left( 2\boldsymbol{u}^n - \boldsymbol{u}^{n-1} \right) \cdot \nabla \bar{\boldsymbol{u}}^{n+1} - \nabla \cdot \sigma \left( \bar{\boldsymbol{u}}^{n+1}, p^n \right) = \rho \boldsymbol{f}^{n+1}$$
$$\bar{\boldsymbol{u}}^{n+1} = 0 \quad \text{on } \Gamma.$$

2. Pressure correction step

$$\frac{\rho}{2\Delta t} \left( 3\boldsymbol{u}^{n+1} - \bar{\boldsymbol{u}}^{n+1} \right) + \nabla \phi^{n+1} = 0$$
$$\nabla \cdot \boldsymbol{u}^{n+1} = 0$$
$$\boldsymbol{u}^{n+1} \cdot \boldsymbol{n} = 0 \quad \text{on } \Gamma,$$

with

$$\phi^{n+1} = p^{n+1} - p^n - \mu \left( \nabla \cdot \bar{\boldsymbol{u}}^{n+1} \right).$$

The term "rotational" comes from the fact that if we add the two substeps together and use the vector identity

$$-\Delta \boldsymbol{u} + \nabla \left( \nabla \cdot \boldsymbol{u} \right) = \nabla \times \nabla \times \boldsymbol{u}$$

we get

$$\frac{\rho}{3\Delta t} \left( 3\boldsymbol{u}^{n+1} - 4\boldsymbol{u}^n + \boldsymbol{u}^{n-1} \right) + \rho \left( 2\boldsymbol{u}^n - \boldsymbol{u}^{n-1} \right) \cdot \nabla \bar{\boldsymbol{u}}^{n+1} + \nabla p^{n+1} + \mu \nabla \times \nabla \times \bar{\boldsymbol{u}}^{n+1} = \rho \boldsymbol{f}^{n+1},$$
$$\nabla \cdot \boldsymbol{u}^{n+1} = 0,$$
$$\boldsymbol{u}^{n+1} \cdot \boldsymbol{n} = 0 \quad \text{on } \Gamma.$$

Furthermore, from the pressure correction step we see that

$$\nabla \times \nabla \times \bar{\boldsymbol{u}}^{n+1} = \nabla \times \nabla \boldsymbol{u}^{n+1},$$

and $\bar{\boldsymbol{u}}^{n+1}$ can also be replaced by $\boldsymbol{u}^{n+1}$ without affecting the accuracy of the scheme. We can also deduce the following Neumann condition for the pressure

$$\frac{\partial p}{\partial \boldsymbol{n}} = \left( \rho \boldsymbol{f}^{n+1} - \rho \left( 2\boldsymbol{u}^n - \boldsymbol{u}^{n-1} \right) \cdot \nabla \boldsymbol{u}^{n+1} + \mu \nabla \times \nabla \times \boldsymbol{u}^{n+1} \right) \cdot \boldsymbol{n} \quad \text{on } \Gamma,$$

which is a consistent boundary condition. The resulting splitting error is only due to the slip condition imposed on the velocity. In this work this is combined with the Spalart–Allmaras turbulence model in order to perform RANS simulations.

## 2.6. Aerodynamic coefficients

The quantities of interest in numerical simulations of flow past an airfoil are the aerodynamic coefficients for a given angle of attack $\alpha$ and a given Reynolds number $Re$. The Reynolds number is defined as

$$Re = \frac{u_\infty c}{\nu},$$

where $u_\infty$ is the constant inflow velocity, $c$ is the chord length and $\nu = \mu/\rho$ is the kinematic viscosity. The three coefficients of interest are the drag coefficient $C_D$, the lift coefficient $C_L$ and the pressure coefficient $C_P$ defined as

$$C_D = \frac{F_x}{\frac{1}{2}\rho u_\infty^2 cl}, \qquad C_L = \frac{F_y}{\frac{1}{2}\rho u_\infty^2 cl}, \qquad C_P = \frac{p - p_\infty}{\frac{1}{2}\rho u_\infty^2}.$$

The quantities $F_x$ and $F_y$ are the horizontal and vertical force components acting on the airfoil respectively, $\rho$ is the density of the fluid, $l$ is the length in the spanwise direction and $p_\infty$ is the ambient pressure. The force components are computed as

$$F = [F_x, F_y]^T = \int_{\Gamma_w} \boldsymbol{\sigma} \cdot \boldsymbol{n} \, \mathrm{d}s,$$

where $\Gamma_w$ is the airfoil surface.

## 3. Simulation setup

Reliable results from the simulations of flow past an airfoil at high Reynolds number require a high quality mesh, properly chosen initial and boundary condition, time step for the simulation as well as the duration for which the simulations have to be run to achieve statistical convergence. Since one of the objectives of this study is the inter-comparison of the computational efficiencies of different methods, these parameters have been so chosen that they are valid and identical across all simulations. This simply means that we might be using smaller time steps or higher resolution or longer integration time than required in some cases. Optimization of these parameters for each solver is not considered here. However, important differences between the solvers will be pointed out.

### 3.1. Domain size and mesh resolution

The mesh is denoted S1 and has two variants: the first one based on linear spline elements and the other on quadratic spline elements. In all other aspects the meshes are similar. The meshes used throughout all the simulations have the same number of elements in order to better compare how each solver fares for the same number of degrees-of-freedom. Along the airfoil surface the meshes have 127 points with a grading factor of 0.96 towards each end. The mesh is designed iteratively for an average $y^+ = 30$ for all Spalart–Allmaras runs with wall function. This ensures that the first node close to the wall is well outside the viscous as well as the buffer layer but within the log layer. For the VMS simulations the same mesh was slightly refined so that after the simulation an average $y^+ = 10$ was obtained. Details about the mesh can be found in Table 1. The mesh is shown in Fig. 3 for $\alpha = 8°$ and $p = 2$. Each mesh consists of 128 patches, of which the layout is shown in Fig. 4.

Table 1
NACA0012: Detailed information about simulation mesh S1.

| Mesh | S1 | S1 |
|---|---|---|
| $p$ | 1 | 2 |
| $n_{el}$ | 34 104 | 34 104 |
| $n_{dof}$ | 103 539 | 117 069 |



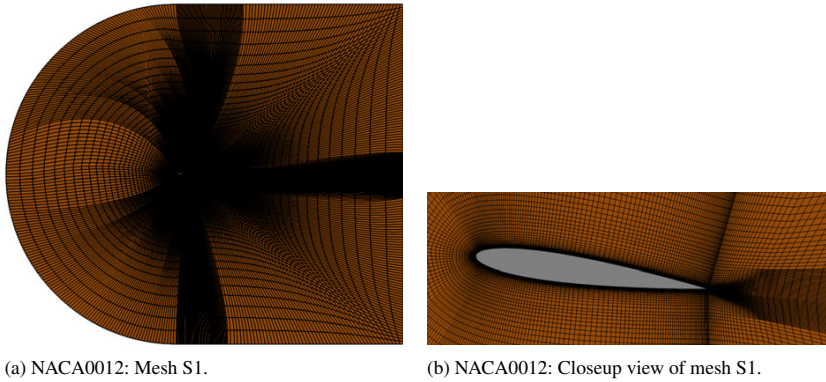(a) NACA0012: Mesh S1.

(b) NACA0012: Closeup view of mesh S1.

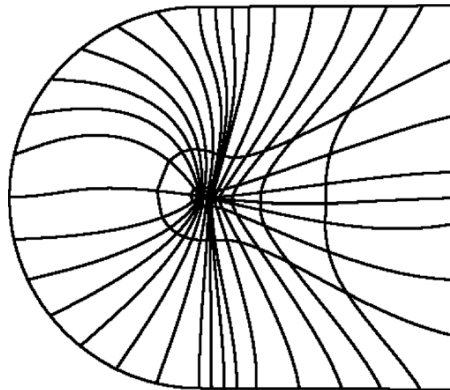Fig. 3. NACA0012: Mesh S1 for $\alpha = 8°$ and $p = 2$.



Fig. 4. NACA0012: Patch layout for all meshes, here shown for $\alpha = 8°$.

### 3.2. Initial and boundary conditions

For all simulations a fluid density of $\rho = 1.205$ kg/m$^3$ and a dynamic viscosity $\mu = 1.8208 \times 10^{-5}$ kg/(m s) are used. The inflow velocity is ramped up to a value of $u_\infty = 45.331$ m/s. The ramping function is given by:

$$u_\infty(t) = \begin{cases} u_\infty \dfrac{1 - \cos(\pi t)}{2} & t < 1.0 \\ u_\infty & \text{otherwise.} \end{cases}$$

All the simulations involving the Chorin and coupled solver with the Spalart–Allmaras turbulence model make use of a no-slip condition on the airfoil surface. For simulations with the VMS solver a weak Dirichlet condition is applied on this boundary. A slip boundary condition is imposed on the top and bottom boundaries. At the outflow a homogeneous Neumann condition for velocity is imposed. The computational domain is shown in Fig. 5.
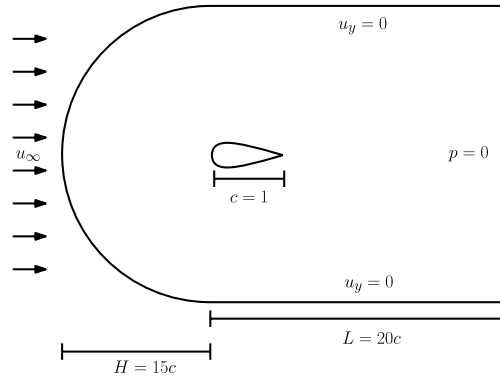
Fig. 5. NACA0012: Computational domain for fixed NACA0012 airfoil.

### 3.3. Time step determination

Determining a sufficiently small time step is crucial for the convergence of the simulations. In order to determine such a time step, simulations with all three solvers for angles of attack $\alpha = 16°, 20°$ until a non-dimensional time $t = 150$ were conducted. These two angles of attack are considered to be the most challenging of our chosen angles of attack because stall is expected at or around these cases. It was found that the biggest time step was $\Delta t = 0.00025$ that could be used with all three solvers without any issue with convergence. We can therefore conclude that the Courant–Friedrichs–Lewy (CFL) condition, which is necessary for stability, is satisfied for all the simulations. It was evident that the time step restriction is stricter for the VMS simulations than for those based on the RANS model. However, for comparison reasons, all the simulations are run with the same time step.

### 3.4. Simulation length

The values of drag and lift coefficients change with time and at some point attain a somewhat constant value. We treat this as a warm-up period and do not use the period in computing the time-averaged quantities. For the VMS simulations the warm-up period is significantly larger than the RANS simulations. In a RANS approach (in this case Spalart–Allmaras) the equations are time-averaged and then solved, while in LES (VMS in this case) the equations are solved and then the desired quantities are time-averaged. The time-averaging requires that most of the flow realizations have been taken into account in the averaging procedure. It is because of this reason that one needs to use much larger time interval over which averaging is conducted. In order to get some idea about the total simulation length a case with an angle of attack of $\alpha = 16°$ was run and evolution of drag and lift coefficients was monitored. These quantities are plotted in Fig. 6. It is clear from the figure that the SA results have already converged for $t < 60$ s. However, for the VMS simulations the averaging procedure can start only after $t > 100$ s. To be consistent all the simulations have been run till $t = 150$ s, i.e. 600 000 timesteps, and the reported quantities are based on the averaging between $t = 125$–150 s.

### 3.5. Definition of test cases

Four angles of attack ($\alpha = 0°, 8°, 16°, 20°$) have been chosen for the investigation. Six simulations have been conducted using VMS, Chorin with Spalart–Allmaras and coupled solver with Spalart–Allmaras for linear and quadratic spline elements. All inputs, including domain size, mesh resolution, boundary conditions, initial condition and simulation time step are identical for all the simulations as explained above. This amounts to a total of 24 simulations under investigation. In addition, similar simulations are conducted with all three solvers for linear and quadratic spline elements for angles of attack of $\alpha = 4°, 10°, 12°, 14°, 18°$. These 30 cases are only used for lift and drag analysis and to populate Fig. 7.
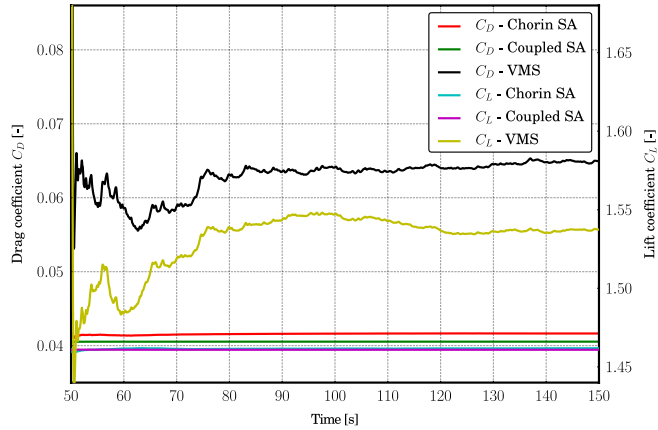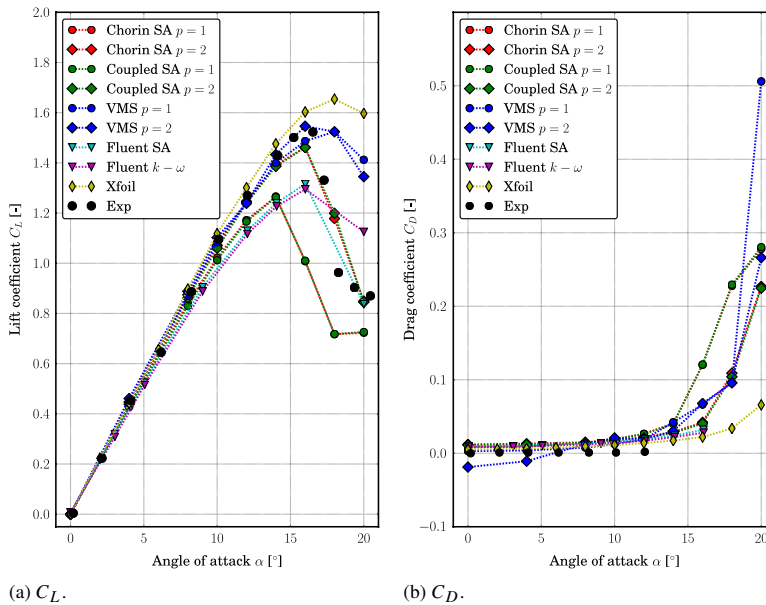
Fig. 6. NACA0012: Cumulative mean of $C_D$ and $C_L$ calculated from $t = 50$ s for grid S1, $p = 2$, $\alpha = 16°$, $\Delta t = 0.00025$ using all three solvers.



(a) $C_L$.

(b) $C_D$.

Fig. 7. NACA0012: Lift and drag coefficients for different combinations of solvers and turbulence models and for different angles of attack.

## 4. Results and discussion

In this section we present a comparison of the results produced by different methods and turbulence models. We have also taken some data from the simulations conducted by Eleni, see [17]. Those simulations were conducted using the commercial finite volume code FLUENT using $k − \omega$ and Spalart–Allmaras turbulence models. The experimental results used for validation purpose are due to Abbott, see [18]. We also compare our simulation results to Xfoil runs. Xfoil is a freely distributed software package which can be used for estimating lift, drag and pressure distributions based on 2D airfoil profiles [19]. The results presented here are based on Xfoil runs in viscous mode at the correct Reynolds number with free transition. For the sake of convenience, in the rest of the paper, we use VMSp1, VMSp2, ChorinSAp1, ChorinSAp2, CoupledSAp1 and CoupledSAp2 to address different simulations. The convention is self-explanatory.

Table 2
NACA0012: Lift and drag coefficients for flow past a fixed NACA0012 airfoil at $\alpha = 0°$ and $Re = 3 \times 10^6$.

|  | Grid | $p$ | $\Delta t$ | $C_L$ | $C_D$ |
|---|---|---|---|---|---|
| IFEM (ChorinSAp1) | S1 | 1 | 0.00025 | −0.0006 | 0.0082 |
| IFEM (ChorinSAp2) | S1 | 2 | 0.00025 | 0.0004 | 0.0119 |
| IFEM (CoupledSAp1) | S1 | 1 | 0.00025 | 0.0000 | 0.0079 |
| IFEM (CoupledSAp2) | S1 | 2 | 0.00025 | 0.0000 | 0.0112 |
| IFEM (VMSp1) | S1 | 1 | 0.00025 | 0.0006 | 0.0029 |
| IFEM (VMSp2) | S1 | 2 | 0.00025 | −0.0005 | −0.0188 |
| Xfoil |  |  |  | 0.0000 | 0.0051 |
| ANSYS Fluent (SA) [17] |  |  |  | 0.0070 | 0.0090 |
| ANSYS Fluent ($k - \omega$ SST) [17] |  |  |  | 0.0070 | 0.0090 |
| Exp: Abbott et al. [18] |  |  |  | 0.0040 | 0.0000 |

## 4.1. Lift, drag and pressure coefficients

For flow around a NACA0012 airfoil it has been observed that the lift increases linearly with the angle of attack up to an angle of approximately 17° after which there is a sudden drop in the lift coefficient and a corresponding increase in the drag coefficient. This condition is referred to as stall. A plot of experimental values of $C_D$ and $C_L$ along with the numerically computed values are presented in Fig. 7. It is clear from the figure that it is relatively easier to predict these quantities up to an angle of 15° before which the flow is attached to the airfoil surface. Different simulations produce almost identical results. However, beyond this angle of attack stall is experienced, characterized by flow separation and different methods/models behave differently resulting in a wide spread of lift and drag coefficients. In the following subsections we explain the flow characteristics for the four different angles of attack investigated in this work in more detail.

### 4.1.1. Results for $\alpha = 0°$

For $\alpha = 0°$ lift and drag coefficients computed by different simulations are presented in a tabular format in Table 2. As is evident from the table, all the simulations give a value of $C_L$ and $C_D$ close to the observation. This is quite expected. The aerodynamic design of the airfoil ensures that the body experiences very small drag force while the perfect symmetry along the centerline ensures that the flow characteristics on the top and bottom surface of the airfoil are exactly the same. The computed pressure contours presented in Figs. 9 and 10 do show a symmetric pressure distribution about the centerline. The vertical component of the pressure forces integrated over the top surface is balanced by those integrated over the bottom surface resulting in zero lift. Also, as can be seen in Figs. 11 and 12 the flow field is perfectly symmetric as expected. The streamlines show that the flow is strongly attached to the airfoil. The vertical component of the resultant of shear forces integrated over the top and bottom surfaces will therefore cancel each other. It should be mentioned that in reality owing to inherent unsteadiness in the flow the drag and lift coefficients can show some variations over time however, in experimental results only the time-averaged quantities are reported. Such variations were also present in the numerical simulations so the reported results were averaged over time as described earlier. The pressure coefficient curves computed by different methods are nearly the same and are presented in Fig. 8(a).

### 4.1.2. Results for $\alpha = 8°$

For $\alpha = 8°$ nothing special is observed except an increase in the lift coefficient. The exact values are shown in Table 3. Once again all the methods produce similar results. The VMS simulations using linear and quadratic spline elements compute values of lift coefficients which are closest to the experimental values. The slight tilt of the airfoil with respect to the incoming flow breaks the symmetry of the flow resulting in a relatively higher pressure caused by a sudden stagnation of the flow on the lower part of the airfoil close to the leading edge (see Figs. 9 and 10). For $\alpha = 0°$ the stagnation zone was just in front of the leading edge and was symmetric with respect to the centerline. The net imbalance in the vertical component of the pressure forces results in a lift force that is represented by the lift coefficient. The drag coefficient also shows a corresponding increase. The increase can be attributed to the larger obstruction offered at this angle of attack. The streamlines in Figs. 11 and 12 confirm that although the flow is unsymmetric it is still attached to the airfoil surface. The pressure coefficient curves computed in different simulations

(a) $\alpha = 0°$.

(b) $\alpha = 8°$.

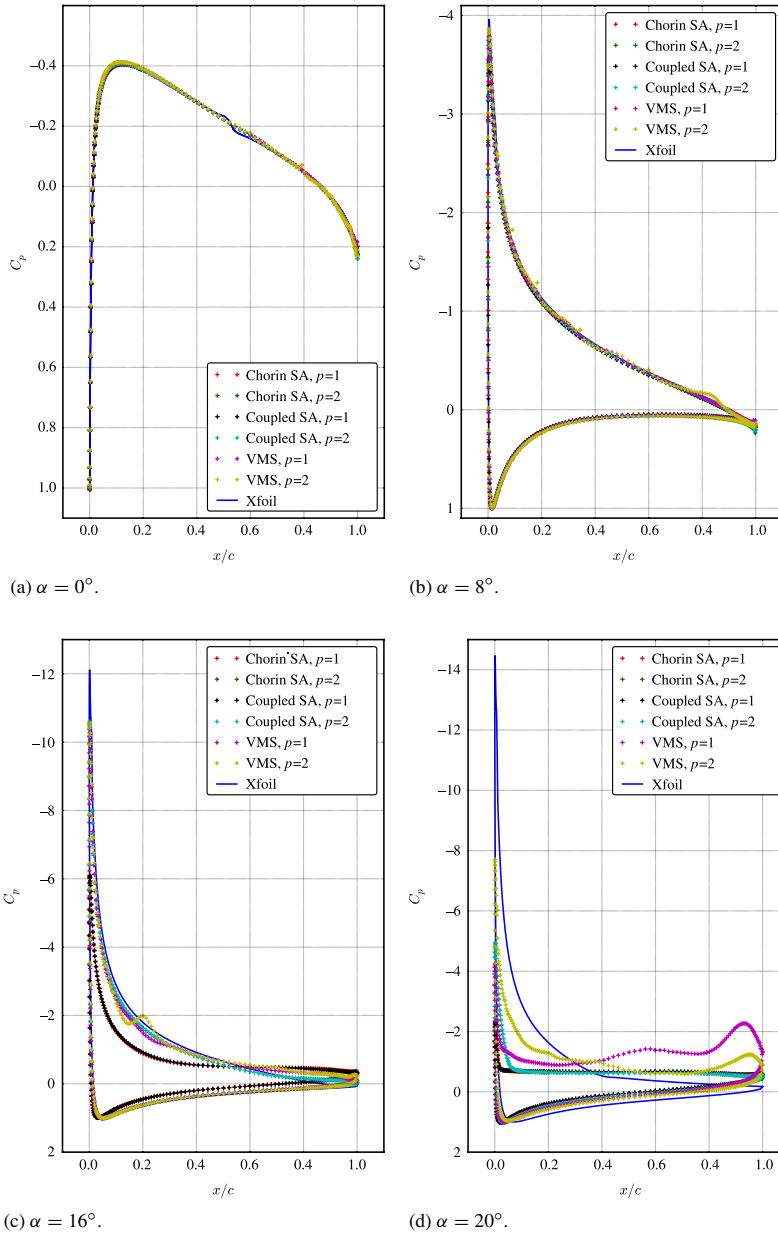(c) $\alpha = 16°$.

(d) $\alpha = 20°$.

Fig. 8. NACA0012: Surface pressure distributions.

even for this angle of attack are still exactly the same except close to the trailing edge where slight differences are observed, see Fig. 8(b).

### 4.1.3. Results for $\alpha = 16°$

In the experimental results presented, the lift coefficient increases almost linearly up to an angle of attack $\alpha = 18°$ after which there is a sharp fall in the lift coefficient and a corresponding increase in the drag coefficient characteristic of the stalled condition. It is worth noting here that different methodologies (including those of others, i.e. Fluent)

Table 3

NACA0012: Lift and drag coefficients for flow past a fixed NACA0012 airfoil at $\alpha = 8°$ and $Re = 3 \times 10^6$.

|  | Grid | $p$ | $\Delta t$ | $C_L$ | $C_D$ |
|---|---|---|---|---|---|
| IFEM (ChorinSAp1) | S1 | 1 | 0.00025 | 0.841 | 0.0143 |
| IFEM (ChorinSAp2) | S1 | 2 | 0.00025 | 0.874 | 0.0149 |
| IFEM (CoupledSAp1) | S1 | 1 | 0.00025 | 0.830 | 0.0141 |
| IFEM (CoupledSAp2) | S1 | 2 | 0.00025 | 0.862 | 0.0144 |
| IFEM (VMSp1) | S1 | 1 | 0.00025 | 0.871 | 0.0077 |
| IFEM (VMSp2) | S1 | 2 | 0.00025 | 0.888 | 0.0124 |
| Xfoil |  |  |  | 0.897 | 0.0093 |
| ANSYS Fluent (SA) [17] |  |  |  | 0.812 | 0.0130 |
| ANSYS Fluent ($k - \omega$ SST) [17] |  |  |  | 0.791 | 0.0120 |
| Exp: Abbott et al. [18] |  |  |  | 0.887 | 0.0010 |

Table 4

NACA0012: Lift and drag coefficients for flow past a fixed NACA0012 airfoil at $\alpha = 16°$ and $Re = 3 \times 10^6$.

|  | Grid | $p$ | $\Delta t$ | $C_L$ | $C_D$ |
|---|---|---|---|---|---|
| IFEM (ChorinSAp1) | S1 | 1 | 0.00025 | 1.008 | 0.1203 |
| IFEM (ChorinSAp2) | S1 | 2 | 0.00025 | 1.462 | 0.0416 |
| IFEM (CoupledSAp1) | S1 | 1 | 0.00025 | 1.010 | 0.1207 |
| IFEM (CoupledSAp2) | S1 | 2 | 0.00025 | 1.461 | 0.0405 |
| IFEM (VMSp1) | S1 | 1 | 0.00025 | 1.487 | 0.0663 |
| IFEM (VMSp2) | S1 | 2 | 0.00025 | 1.546 | 0.0678 |
| Xfoil |  |  |  | 1.603 | 0.0220 |
| ANSYS Fluent (SA) [17] |  |  |  | 1.316 | 0.0320 |
| ANSYS Fluent ($k - \omega$ SST) [17] |  |  |  | 1.295 | 0.0280 |
| Exp: Abbott et al. [18] |  |  |  | 1.523 | N/A |

produce similar results up to an angle of attack of $\alpha = 15°$. However, at around an angle of attack of $\alpha = 16°$, the flow on the upper surface of the airfoil begins to separate and a condition known as stall begins to develop. At this point there are big variations in the prediction of lift coefficients by different simulations. The best predictions are by the VMS simulations. However, Table 4 reveals that almost all the simulations conducted with quadratic spline elements irrespective of the turbulence model do well to predict the lift coefficient accurately. In the current situation the effect of changing the order has little effect on the VMS simulations compared to that involving Spalart–Allmaras model. A closer inspection of Figs. 11 and 12 reveals interesting facts regarding the flow behavior on the top surface. ChorinSAp1 predicts flow separation very close to the leading edge while in the CoupledSAp1 this is observed further downward. The VMSp1 predicts this separation further towards the trailing edge. An increase in the order of the elements suppresses the flow separation and makes it happen close to the trailing edge. The results predicted by ChorinSAp2, CoupledSAp2, VMSp1 and VMSp2 also compare well with the experiment. The fact that stall is not observed at $\alpha = 16°$ in the experiment also attests the fact that an increase in the order helps in predicting reality much better and hence their use is highly recommended.

### 4.1.4. Results for $\alpha = 20°$

An angle of attack $\alpha = 20°$ corresponds to a situation which is marked by flow separation predicted by all simulations. The difference is only in the location of the separation point. For the Spalart–Allmaras models this is closer to the leading edge compared to the VMS simulations. Table 5 shows that the Spalart–Allmaras models make a better estimate of the lift coefficients with the best predictions by the one using quadratic elements. VMS simulations according to the Figs. 9–12 are characterized by vortex shedding.

In general the flow behavior, pressure distribution, streamlines on the bottom side of the airfoil are very similar for all the methods adopted for a particular angle of attack. The profile of $C_P$, see Fig. 8(d), stresses that point as the parts of all the profiles corresponding to the bottom surface nearly collapse into a single curve. However, on the part corresponding to the upper surface significant variations are observed especially for $\alpha = 16°, 20°$.

(a) ChorinSA.          (b) CoupledSA.          (c) VMS.

(d) ChorinSA.          (e) CoupledSA.          (f) VMS.

(g) ChorinSA.          (h) CoupledSA.          (i) VMS.

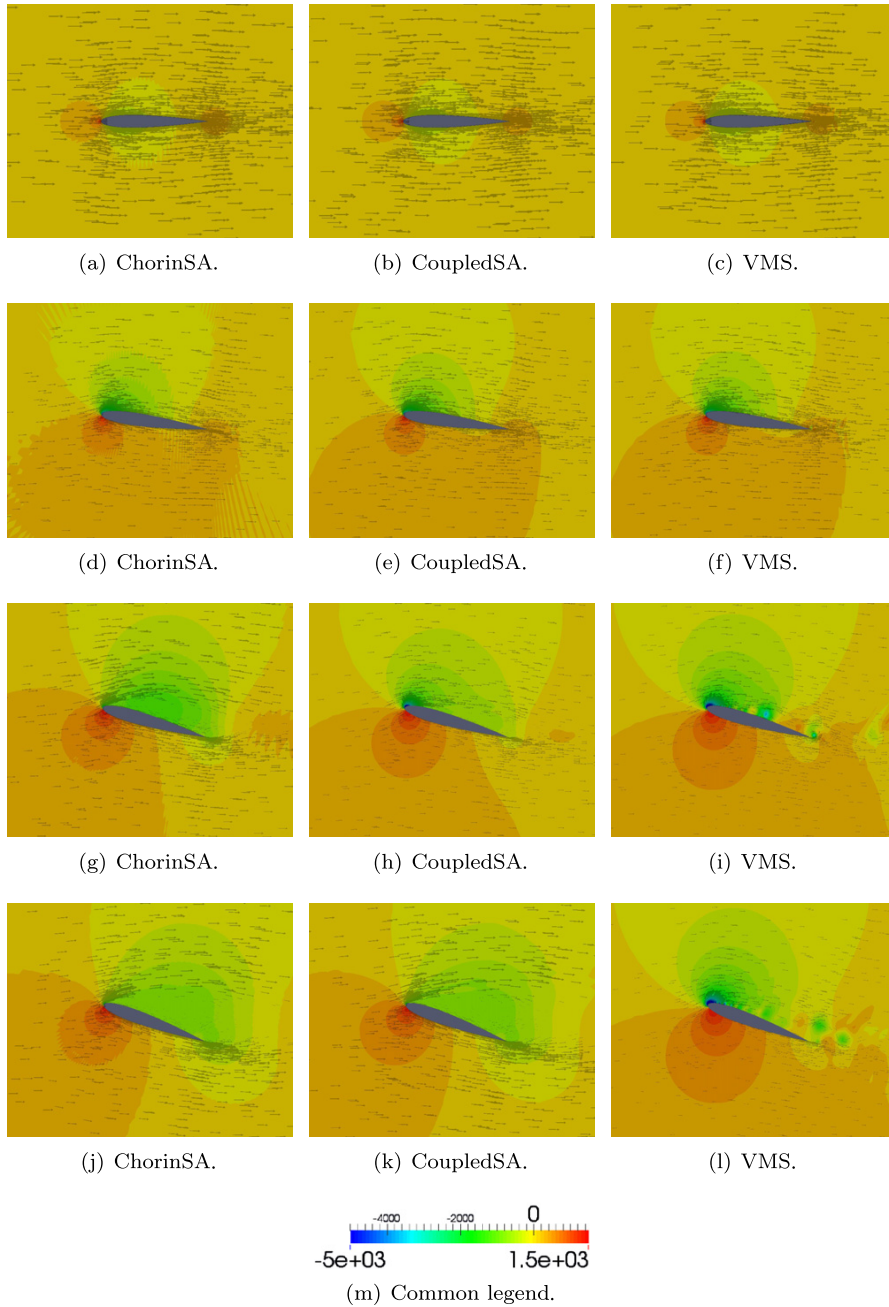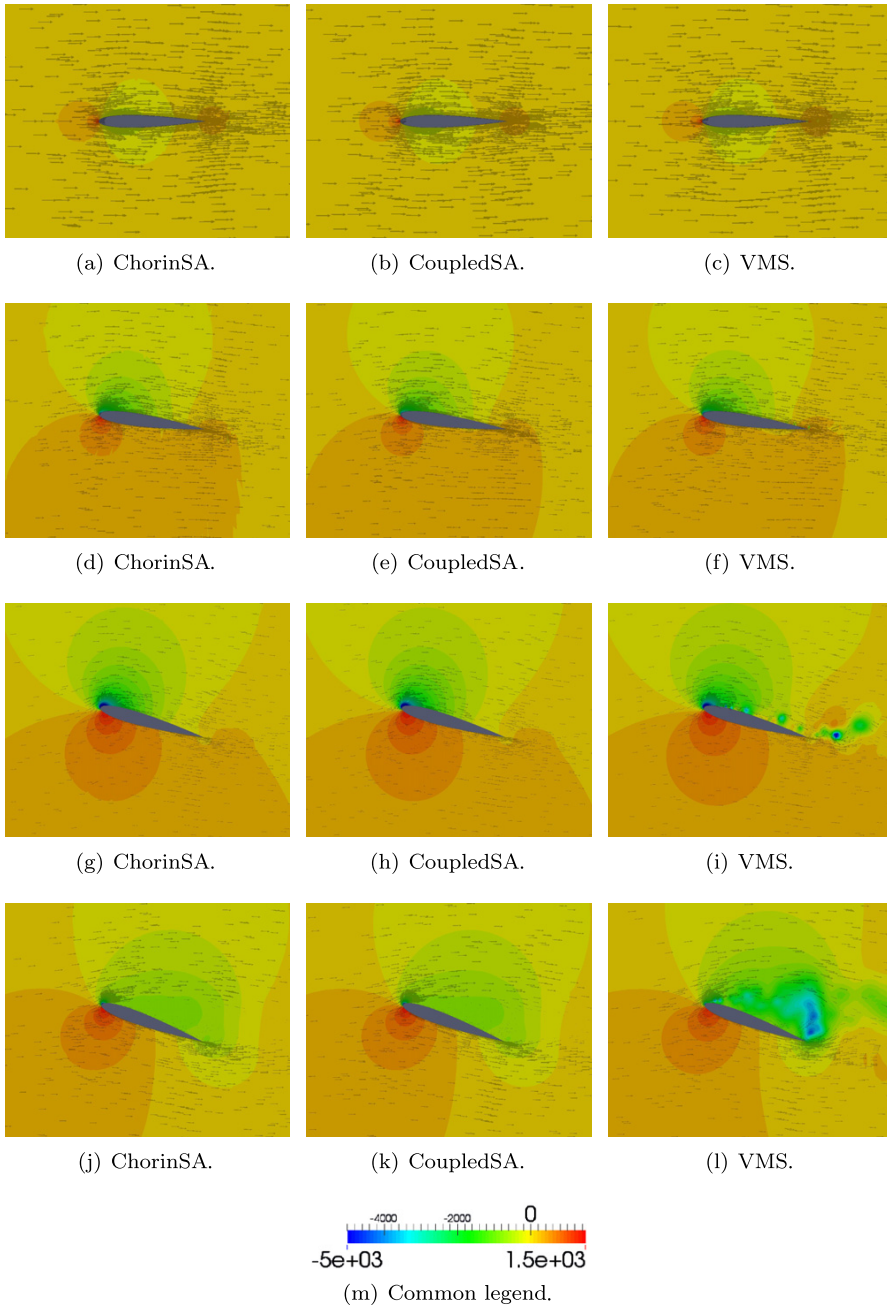(j) ChorinSA.          (k) CoupledSA.          (l) VMS.

(m) Common legend.

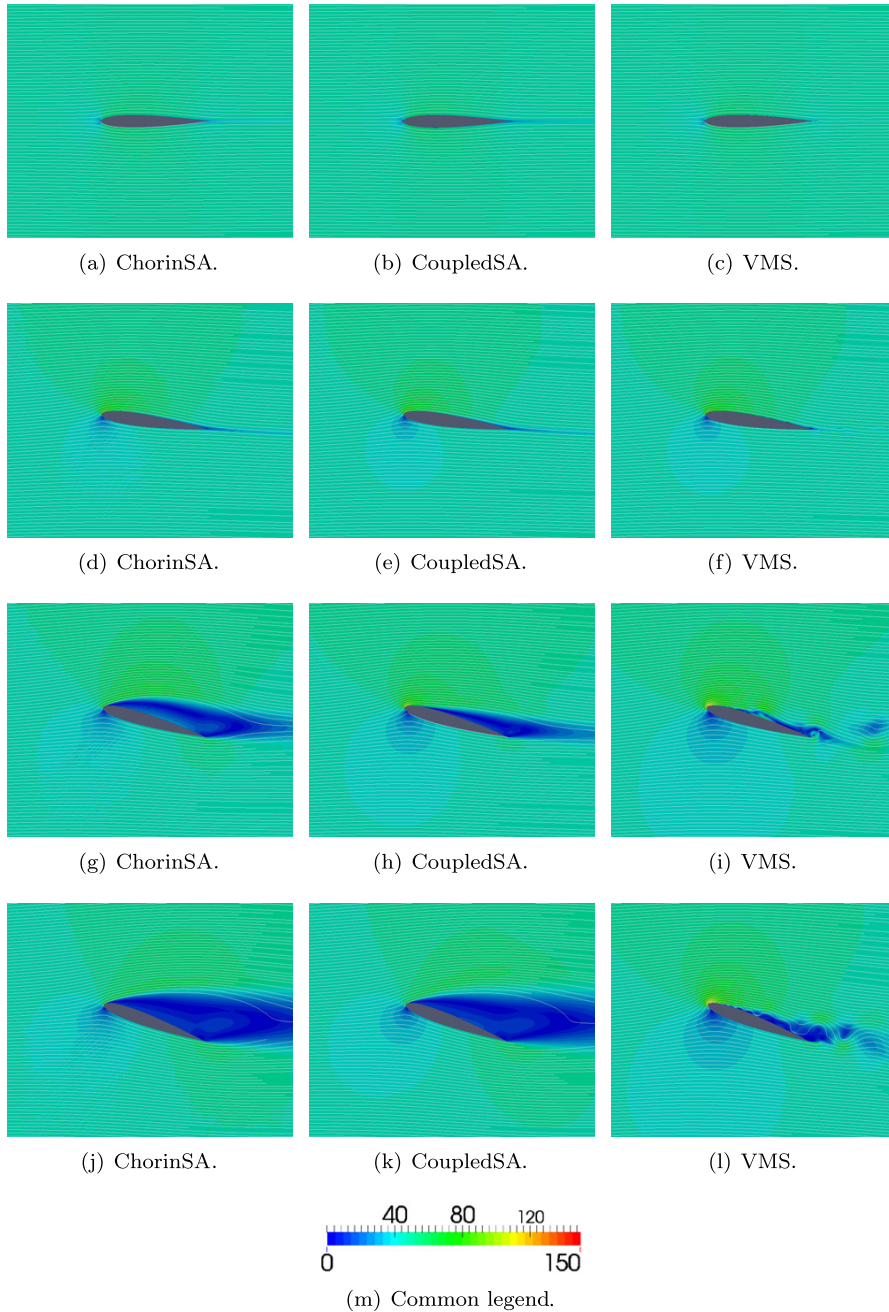Fig. 9. Pressure field computed by Chorin-SA, Coupled-SA,VMS for angles of attack of 0° (a–c), 8° (d–f), 16° (g–i) and 20° (j–l) with linear spline elements.

## 4.2. Comparison of the computational efficiency of different methods

Determination and comparison of the computational efficiency of the different methods is one of the main objectives of this work. All the simulations were conducted using our in-house CFD code IFEM. The linear solvers

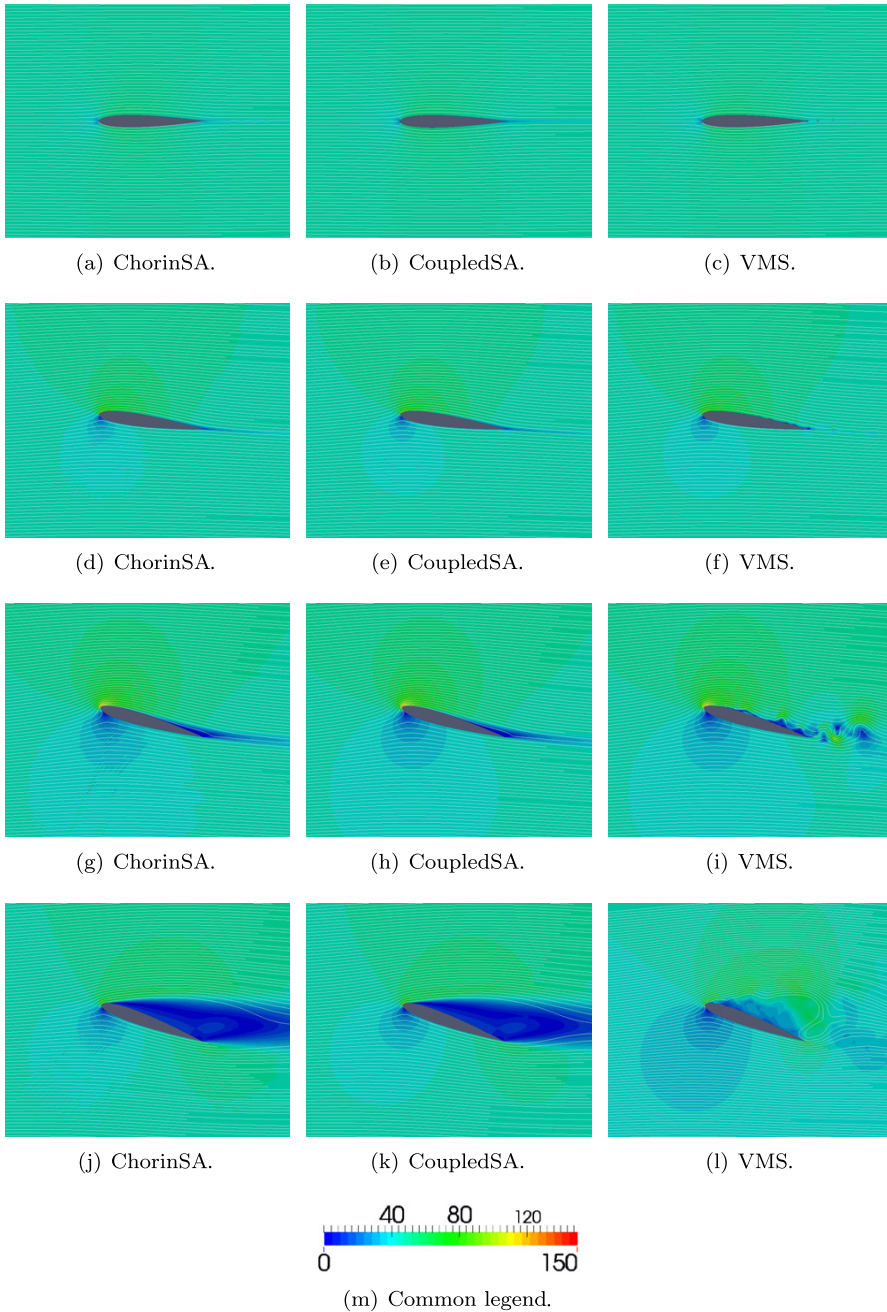Fig. 10. Pressure field computed by Chorin-SA, Coupled-SA, VMS for angles of attack of 0° (a–c), 8° (d–f), 16° (g–i) and 20° (j–l) with quadratic spline elements.

are based on the PETSc package [20] version 3.4.2 and are compiled with the Intel C++ compiler version 13.0.1, using the SGI MPT MPI implementation, all running on SUSE Linux Enterprise Server 11. The simulations were run on the "Vilje" supercomputer at the Norwegian University of Science and Technology which is currently ranked as number 99 on the top 500 list (June 2014). This is an SGI Altix system with Intel Xeon E5-2670 (Sandy Bridge)

(a) ChorinSA.

(b) CoupledSA.

(c) VMS.

(d) ChorinSA.

(e) CoupledSA.

(f) VMS.

(g) ChorinSA.

(h) CoupledSA.

(i) VMS.

(j) ChorinSA.

(k) CoupledSA.

(l) VMS.

(m) Common legend.

Fig. 11. Velocity magnitude computed by Chorin-SA, Coupled-SA, VMS for angles of attack of 0° (a–c), 8° (d–f), 16° (g–i) and 20° (j–l) with linear spline elements.

processors. The 1404 computational nodes in the system consist of 2 octa-core processors in SMP, with 20 MB L3 cache per processor. The nodes are connected using a high-speed infiniband network.

To understand the computational behavior of the three methods evaluated in this work it is important to have a deeper understanding of how the solvers work. In a VMS-based solver, a single non-linear saddle-point system has to

Fig. 12. Velocity magnitude computed by Chorin-SA, Coupled-SA, VMS for angles of attack of 0° (a–c), 8° (d–f), 16° (g–i) and 20° (j–l) with quadratic spline elements.

be solved at each time level without any additional equations. On the other hand, in a coupled Navier–Stokes solver in a RANS setting, an additional elliptic equation for eddy viscosity has to be solved along with the non-linear saddle-point system. The Chorin-based solver avoids the need to solve a non-linear saddle-point system at each time level, and rather updates the velocity and pressure through a series of elliptic solves. This is based on a hope that solving
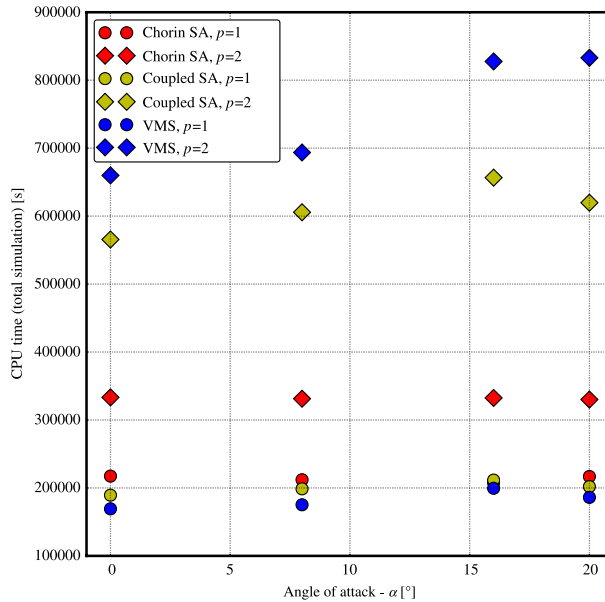
Fig. 13. NACA0012: Total CPU time for the simulations using all three solvers.

Table 5
NACA0012: Lift and drag coefficients for flow past a fixed NACA0012 airfoil at $\alpha = 20°$ and $Re = 3 \times 10^6$.

|  | Grid | $p$ | $\Delta t$ | $C_L$ | $C_D$ |
|---|---|---|---|---|---|
| IFEM (ChorinSAp1) | S1 | 1 | 0.00025 | 0.723 | 0.2779 |
| IFEM (ChorinSAp2) | S1 | 2 | 0.00025 | 0.849 | 0.2267 |
| IFEM (CoupledSAp1) | S1 | 1 | 0.00025 | 0.726 | 0.2805 |
| IFEM (CoupledSAp2) | S1 | 2 | 0.00025 | 0.845 | 0.2246 |
| IFEM (VMSp1) | S1 | 1 | 0.00025 | 1.412 | 0.5060 |
| IFEM (VMSp2) | S1 | 2 | 0.00025 | 1.345 | 0.2662 |
| Xfoil |  |  |  | 1.597 | 0.0658 |
| ANSYS Fluent (SA) [17] |  |  |  | 0.837 | N/A |
| ANSYS Fluent ($k - \omega$ SST) [17] |  |  |  | 1.125 | N/A |
| Exp: Abbott et al. [18] |  |  |  | 0.870 | N/A |

the elliptic equations will have a lower cost than solving a single saddle-point system. If used in a RANS setting, an additional equation is required to solve for the eddy viscosity, giving a grand total of four elliptic solves per time step. It might now appear like the coupled solver in RANS setting will always be outperformed by the VMS-based solver, however this is not the case. The reason for this is the additional terms in Eq. (13). These include the Hessian of the basis functions, which is expensive to evaluate (except for linears where it is zero by definition). Thus, for higher order elements the assembly time for the VMS approach will increase significantly. They also typically make the system matrix more ill-conditioned, resulting in a double penalty, as linear solves will increase in cost.

Furthermore, the use of isogeometric elements influences the results. The extra smoothness of the basis implies that there are basis functions with support across two elements, and which are smooth across the element boundaries. Since Gaussian quadrature is still used, and this can only be used with success if the integrand is smooth, more integration points are required per basis function. In particular, for quadratics one has to use two Gauss points per knot-span, where one classical element corresponds to two knot-spans (the support of a basis function). This results in more time being spent on assembly compared to traditional finite elements.

The total simulation time, calculated as an average of all 64 processors, is given in Fig. 13. As expected, the difference in the total CPU time is more pronounced for simulations with $p = 2$ than for simulations with $p = 1$. For
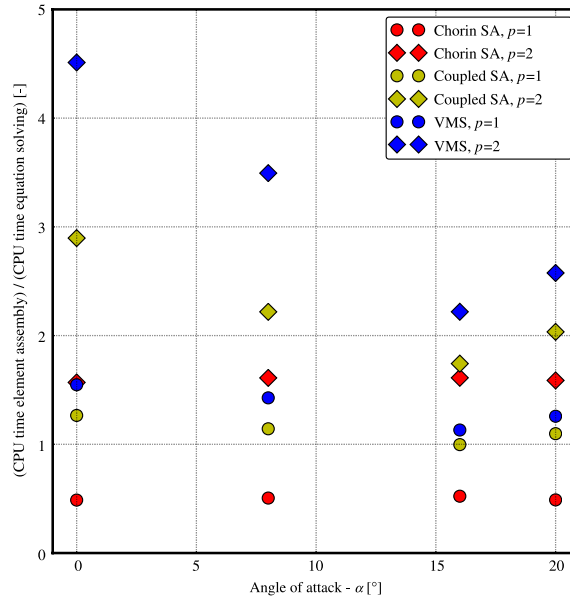
Fig. 14. NACA0012: Ratio of CPU time spent on element assembly and equation solving.

$p = 1$ the total CPU time is similar for all the three solvers. However, the VMS solver has a slight advantage, which is not a big surprise keeping in mind the discussion in the previous paragraph. The cost of solving and assembling extra systems is higher than the extra cost of assembling the VMS terms, since the Hessian can be skipped. For $p = 2$, however, the balance tips. Now the Chorin solver is significantly faster than the others, with the VMS solver as the slowest. This is the accumulated effect of the extra terms to be assembled, and the extra assembly caused by the isogeometric approach rearing its head. Additionally, the coupled approaches both are penalized at higher angles of attack. For the Chorin solver this does not seem to influence the simulation time to any significant degree.

In Fig. 14 the ratio of CPU time spent on assembly compared to equation solving is given. We clearly see that this ratio drops for the coupled solvers for higher angles of attack, indicating that more time is spent on solving equations. Most likely, this is the effect of larger element aspect ratios in the boundary layer making the preconditioner less efficient. While this effect is also present for the Chorin solver, it is much less pronounced. This can be attributed to the SIMPLE approach used in the Schur-decomposition-based preconditioner for the saddle-point system. The multigrid sweep is a worse approximation of the Helmholtz operator, and thus the pressure preconditioner block suffers. These results indicate that a RANS approach can be of great benefit for simulations with $p = 2$ or higher, in particular if a Chorin solver is employed. The figure shows clearly that the ratio is much higher for the VMS solver than the other solvers. For the high angles of attack the ratio is reduced both for the VMS and the coupled solver, which means that the solvers spend more time on equation solving.

The assembly process can be further analyzed. For the coupled and VMS solvers we normalize the CPU time by the average number of nonlinear iterations used in each time step. The result is shown in Fig. 15. The huge difference between $p = 1$ and $p = 2$ is evident. For $p = 1$ the VMS solver spends the least time of the three solvers on element assembly, but spends the longest time for $p = 2$.

## 5. Conclusions

In this work we have contributed a comparison of three isogeometric incompressible Navier–Stokes solvers. These three solvers are a Chorin solver with the Spalart–Allmaras turbulence model, a coupled Navier–Stokes solver with the Spalart–Allmaras turbulence model and a variational multiscale solver. All solvers have been used for investigating flows past a fixed NACA0012 airfoil at a Reynolds number $3 \times 10^6$ at four different angles of attack. The most
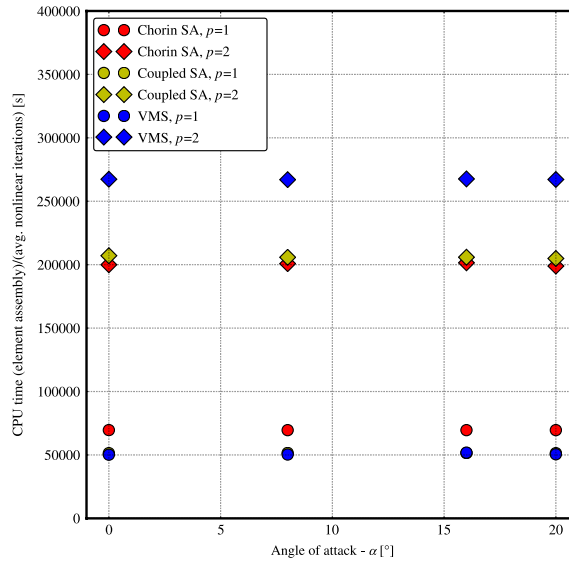
Fig. 15. NACA0012: CPU time spent on element assembly (normalized by number of nonlinear iterations).

significant findings are:

- computation of lift and drag coefficient in accordance with other references, both experimental and numerical. It seems to be relatively easy to predict lift and drag up to an angle of attack of 15° before which the flow is attached to the airfoil surface. Beyond an angle of attack of 15° we notice a large spread in lift and drag coefficients, meaning that it is more difficult to predict lift and drag when the flow enters the stall regime.
- increasing element order from 1 to 2 generally gives better approximation of lift, drag and pressure coefficients. However, the effect of increasing the element order from 1 to 2 is more pronounced for the Spalart–Allmaras models.
- there is not much difference between the total computational time for the three solvers with $p = 1$. With $p = 2$ the Chorin solver is significantly faster than the two others. The Chorin solver is not penalized at higher angles of attack in the same way as the other two solvers.
- a general recommendation for the kind of simulations presented in this paper, i.e. 2D simulation of high Reynolds number flow past an airfoil, is to use a RANS approach, preferably with a Chorin solver, with $p = 2$. The VMS solver would probably prove more useful if the goal is to investigate vortex shedding and wake effects. Furthermore, the conclusions presented herein apply to 2D simulations, separate investigations should be done for 3D simulations.

However, we want to underline that the VMS turbulence model is (theoretically only) applicable for three-dimensional flows. In this study we have suppressed the three-dimensionality of the flow thereby eliminating the physical processes like three-dimensional vorticity fluctuations and the associated vortex-stretching from happening. Thus, the simulation by VMS was reduced to a mere numerical exercise, and therefore not much should be read into their ability to model the physical processes. For this, separate three-dimensional studies should be undertaken. Having said that, the discussion regarding the computational efficiency still holds. One more point worth mentioning here is that for a RANS model like the Spalart–Allmaras model there is no need to run the simulations for so long because convergence is reached within approximately 1/4th of the total time of simulation we used. However, VMS owing to inherent unsteadiness had to be run for a much longer time to ensure statistical convergence. Thus the RANS simulations in this study are much faster than they appear in the paper.

### Acknowledgments

## References

[1] T. Hughes, J. Cottrell, Y. Bazilevs, Isogeometric analysis: CAD, finite elements, NURBS, exact geometry and mesh refinement, Comput. Methods Appl. Mech. Engrg. 194 (39–41) (2005) 4135–4195.

[2] J.A. Cottrell, T.J. Hughes, Y. Bazilevs, Isogeometric Analysis: Toward Integration of CAD and FEA, Wiley, Chichester, 2009.

[3] Y. Bazilevs, V.M. Calo, J.A. Cottrell, T.J.R. Hughes, A. Reali, G. Scovazzi, Variational multiscale residual-based turbulence modeling for large eddy simulation of incompressible flows, Comput. Methods Appl. Mech. Engrg. 197 (2007) 173–201.

[4] V.M. Calo, Residual-based multiscale turbulence modeling: finite volume simulation of bypass transistion (Ph.D. Thesis), Stanford University, 2004.

[5] I. Akkerman, Y. Bazilevs, V. Calo, T. Hughes, S. Hulshoff, The role of continuity in residual-based variational multiscale modeling of turbulence, Comput. Mech. 41 (3) (2008) 371–378.

[6] K. Valen-Sendstad, A. Logg, K.-A. Mardal, H. Narayanan, M. Mortensen, A comparison of some common finite element schemes for the incompressible Navier–Stokes equations, in: Lect. Notes Comput. Sci. Eng., Vol. 84, Springer, 2012, pp. 395–418 (chapter 21).

[7] P. Spalart, S. Allmaras, One-equation turbulence model for aerodynamic flows, Rech. Aerosp. 1 (1994) 5–21.

[8] S.R. Allmaras, F.T. Johnson, P.R. Spalart, Modifications and clarifications for the implementation of the Spalart–Allmaras turbulence model, in: 7th International Conference on Computational Fluid Dynamics, ICCFD7, Proceedings, 2012.

[9] F. Brezzi, L.P. Franca, T.J.R. Hughes, A. Russo, $b = \int g$, Comput. Methods Appl. Mech. Engrg. 145 (1997) 329–339.

[10] T.J.R. Hughes, Multiscale phenomena: Green's functions, the Dirichlet-to-Neumann formulation, subgrid scale models, bubbles and the origins of stabilized methods, Comput. Methods Appl. Mech. Engrg. 127 (1995) 387–401.

[11] T.J.R. Hughes, G.R. Feijóo, L. Mazzei, J.-B. Quincy, The variational multiscale method—a paradigm for computational mechanics, Comput. Methods Appl. Mech. Engrg. 166 (1998) 3–24.

[12] T.J.R. Hughes, G. Sangalli, Variational multiscale analysis: the fine-scale Green's function, projection, optimization, localization, and stabilized methods, SIAM J. Numer. Anal. 245 (2007) 539–557.

[13] A.J. Chorin, Numerical solution of the Navier–Stokes equations, Math. Comp. 22 (1968) 745–762.

[14] R. Temam, Sur l'approximation de la solution des equations de Navier–Stokes par la methode des pas fractionnaires (II), Arch. Ration. Mech. Anal. 33 (5) (1969) 377–385.

[15] J. Guermond, P. Minev, J. Shen, An overview of projection methods for incompressible flows, Comput. Methods Appl. Mech. Engrg. 195 (44–47) (2006) 6011–6045.

[16] L. Timmermans, P. Minev, F. Van De Vosse, An approximate projection scheme for incompressible flow using spectral elements, Internat. J. Numer. Methods Fluids 22 (7) (1996) 673–688.

[17] D.C. Eleni, T.I. Athanasios, M.P. Dionissios, Evaluation of the turbulence models for the simulation of the flow over a National Advisory Committee for Aeronautics (NACA) 0012 airfoil, J. Mech. Eng. Res. 4 (3) (2012) 100–111.

[18] I.H. Abbott, A.E. von Doenhoff, Theory of Wing Sections, Dover Publishing, 1959.

[19] Xfoil. URL: http://web.mit.edu/drela/Public/web/xfoil/.

[20] S. Balay, S. Abhyankar, M.F. Adams, J. Brown, P. Brune, K. Buschelman, V. Eijkhout, W.D. Gropp, D. Kaushik, M.G. Knepley, L.C. McInnes, K. Rupp, B.F. Smith, H. Zhang, PETSc Web page, 2014. URL: http://www.mcs.anl.gov/petsc.

# Paper III

## Numerical benchmarking of fluid-structure interaction: An isogeometric finite element approach

Knut Nordanger, Adil Rasheed, Knut Morten Okstad, Arne Morten Kvarving, Runar Holdahl and Trond Kvamsdal

# Paper III

# Numerical benchmarking of fluid-structure interaction: An isogeometric finite element approach

Knut Nordanger[a,*], Adil Rasheed[b], Knut Morten Okstad[b], Arne Morten Kvarving[b], Runar Holdahl[b], Trond Kvamsdal[a,b]

[a]*Department of Mathematical Sciences, Norwegian University of Science and Technology, NO-7491 Trondheim, Norway*
[b]*SINTEF ICT, Department of Applied Mathematics, Postboks 4760 Sluppen, NO-7465 Trondheim, Norway*

## Abstract

In this paper we describe and evaluate an isogeometric finite element program, IFEM-FSI, for doing coupled fluid-structure interaction simulations. We investigate the role played by employing higher polynomial orders and higher regularity for solving a well known benchmark problem for flow past a circular cylinder with an attached flexible bar at Reynolds number $Re = 100$. Furthermore, we investigate the sensitivity to resolution in the fluid mesh as well as stiffness distribution in the mesh movement algorithm. Mesh quality is also assessed. Our simulations indicate that quadratic and cubic spline elements give better estimation of lift, drag and displacements than linear spline elements.

*Keywords:* Isogeometric analysis, Fluid-structure interaction

## 1. Introduction

Coupled fluid-structure interaction (FSI) simulations of full-scale wind turbine rotors under realistic operational conditions have been conducted recently [1, 2, 3]. Such simulations open new possibilities of detailed studies of nonlinear effects, which are important for the design and performance of wind turbines [4]. These effects include high frequency structural vibrations and aerodynamical instabilities like buckling and fluttering. Buckling and fluttering can lead to fatigue or structural failure of the turbine, as well as the initialization, transport and decay of wake vortices. This is a major concern for the power production in wind parks. However, coupled FSI simulations of transitional and turbulent flows remain computationally very expensive, and more effort has to be put into research on numerical methods and software development.

The development of numerical tools for FSI simulations of wind turbines require accurate, robust and computationally efficient numerical solvers for the

---

*Corresponding author
*Email addresses:* `knut.nordanger@math.ntnu.no` (Knut Nordanger), `adil.rasheed@sintef.no` (Adil Rasheed), `knut.morten.okstad@sintef.no` (Knut Morten Okstad), `arne.morten.kvarving@sintef.no` (Arne Morten Kvarving), `runar.holdahl@sintef.no` (Runar Holdahl), `trond.kvamsdal@math.ntnu.no` (Trond Kvamsdal)

air flow and structural dynamics of the rotor. Isogeometric analysis (IGA), introduced in [5], has demonstrated that much can be gained in this respect by replacing traditional low-order finite elements (FE) by volumetric NURBS (Non-Uniform Rational B-Splines). Spline approximations have some desirable properties both with respect to geometrical representation and analysis, since both the order and the smoothness of the basis functions are easily changed. In particular, numerical results indicate that increased continuity of the finite element basis improve the approximation of both material stresses in structural analysis and sharp boundary layers in CFD analysis [6].

Fluid-structure interaction problems usually lead to an unsteady moving domain for the fluid part. Traditional computational fluid dynamic codes solve the fluid equations on a fixed (Eulerian) grid. A classical approach to overcome this difficulty is to consider the so-called Arbitrary Lagrangian-Eulerian (ALE) method where the grid is moved arbitrary inside the fluid domain, following the movement of the boundary [7, 8]. Furthermore, a fluid-structure interaction problem is not only a two-field (fluid and solid) but a three-field coupling problem (fluid, solid and mesh). We also have to add that the global solution must not depend on the mesh motion, and this is naturally verified when the quality of the mesh is preserved. In this paper we apply our isogeometric finite element solver IFEM to the well known FSI benchmark problem presented in [9, 10].

## 2. Theory

Here we present the theory behind our fluid and structural solvers, along with details of how they are coupled and how the mesh movement is done. Mesh generation is also explained. The fluid domain, consisting of an incompressible Newtonian fluid, is denoted $\Omega^f$, while the structural domain, consisting of an elastic solid, is denoted $\Omega^s$.

### 2.1. Fluid solver

The flow is mathematically described by the incompressible Navier-Stokes equations which read

$$\rho \frac{\partial \boldsymbol{u}^f}{\partial t} + \rho \left( \boldsymbol{u}^f \cdot \nabla \right) \boldsymbol{u}^f - \nabla \cdot \boldsymbol{\sigma} \left( \boldsymbol{u}^f, p \right) = \rho \boldsymbol{f} \quad \text{in } \Omega^f$$
$$\nabla \cdot \boldsymbol{u}^f = 0 \quad \text{in } \Omega^f. \tag{1}$$

In this setting $\Omega \in \mathbb{R}^d$, $d = 2, 3$, is a suitable, sufficiently regular and open domain, $\rho$ is the constant fluid density, $p$ is the pressure, $\boldsymbol{u}^f$ is the fluid velocity vector and $\boldsymbol{f}$ a volumetric body force. The Cauchy stress tensor can be written as

$$\boldsymbol{\sigma}(\boldsymbol{u}^f, p) = -p\boldsymbol{I} + 2\mu \boldsymbol{\epsilon}(\boldsymbol{u^f}),$$

where $\boldsymbol{I}$ is the identity tensor, $\mu$ the dynamic viscosity and the strain rate $\boldsymbol{\epsilon}$ is defined as

$$\boldsymbol{\epsilon}(\boldsymbol{u}^f) = \frac{1}{2} \left( \nabla \boldsymbol{u}^f + (\nabla \boldsymbol{u}^f)^T \right).$$

Furthermore we define the boundary to be $\partial \Omega^f = \Gamma^f = \Gamma_D^f \cup \Gamma_N^f \cup \Gamma_M^f$ in order to handle boundaries with Dirichlet, Neumann or mixed boundary conditions. We

denote $\Gamma_D^f$ the boundaries with Dirichlet conditions, $\Gamma_N^f$ the boundaries with Neumann conditions and $\Gamma_M^f$ the boundaries with mixed conditions. Mixed boundary conditions are used in situations where the normal velocity component is given, usually zero, together with the tangential stresses, and can model symmetry planes and slip or friction conditions.

The variational formulation can now be expressed as: Find $(\boldsymbol{u}^f, p) \in \boldsymbol{U} \times Q$ such that

$$\left( \rho \frac{\partial \boldsymbol{u}^f}{\partial t}, \boldsymbol{v} \right) + c(\boldsymbol{u}^f; \boldsymbol{u}^f, \boldsymbol{v}) + b(p, \boldsymbol{v}) + a(\boldsymbol{u}^f, \boldsymbol{u}^f) + b(q, \boldsymbol{u}^f) = f(\boldsymbol{v}) \qquad (2)$$

for $(\boldsymbol{v}, q) \in \boldsymbol{V} \times Q$. We have defined the spaces

$$\boldsymbol{U} = \boldsymbol{H}_{\Gamma_D, \Gamma_M^\perp}(\Omega) = \left\{ \boldsymbol{v} \in \boldsymbol{H}^1(\Omega) \mid \boldsymbol{v} = \boldsymbol{u}_{\boldsymbol{D}}^f \text{ on } \Gamma_D \text{ and } \boldsymbol{v} \cdot \boldsymbol{n} = u_\perp^f \text{ on } \Gamma_M \right\}$$

$$\boldsymbol{V} = \boldsymbol{H}_{\Gamma_D, \Gamma_M^\perp; 0}(\Omega) = \left\{ \boldsymbol{v} \in \boldsymbol{H}^1(\Omega) \mid \boldsymbol{v} = 0 \text{ on } \Gamma_D \text{ and } \boldsymbol{v} \cdot \boldsymbol{n} = 0 \text{ on } \Gamma_M \right\}$$

$$Q = L^2(\Omega),$$

where $\boldsymbol{u}_{\boldsymbol{D}}^f$ and $u_\perp^f$ both are given functions and $\boldsymbol{n}$ is the unit outer normal on $\Gamma$. We have also defined the forms

$$a(\boldsymbol{u}^f, \boldsymbol{v}) = 2 \int_\Omega \mu \boldsymbol{\epsilon}(\boldsymbol{u}^f) \,:\, \boldsymbol{\epsilon}(\boldsymbol{v}) \, \mathrm{d}\boldsymbol{x}$$

$$b(q, \boldsymbol{v}) = -\int_\Omega (\nabla \cdot \boldsymbol{v}) q \, \mathrm{d}\boldsymbol{x}$$

$$c(\boldsymbol{w}; \boldsymbol{u}^f, \boldsymbol{v}) = \int_\Omega \rho (\boldsymbol{w} \cdot \nabla) \boldsymbol{u}^f \cdot \boldsymbol{v} \, \mathrm{d}\boldsymbol{x}$$

$$f(\boldsymbol{v}) = \int_\Omega \rho \boldsymbol{f} \cdot \boldsymbol{v} \, \mathrm{d}\boldsymbol{x} + \int_{\Gamma_N} \boldsymbol{t} \cdot \boldsymbol{v} \, \mathrm{d}\boldsymbol{s},$$

where $\boldsymbol{t} = \boldsymbol{\sigma} \cdot \boldsymbol{n}$ is the traction vector on $\Gamma$.

### 2.1.1. Isogeometric finite element approximation

In this work we employ an isogeometric finite element method similar to what was introduced in [5] and presented in [11]. The isogeometric finite element method approximates the solution by using a spline basis of polynomial order $p$ and regularity $C^{p-1}$. In traditional finite element formulations $C^0$ Lagrange polynomials of low order (typically $p = 1$ or $p = 2$) are used. Our approach is based on a conforming finite element approximation, i.e.

$$\boldsymbol{U}_h \subset \boldsymbol{U}, \quad \boldsymbol{V}_h \subset \boldsymbol{V}, \quad Q_h \subset Q.$$

The discrete approximation spaces $\boldsymbol{U}_h$, $\boldsymbol{V}_h$, $Q_h$ are chosen as the isogeometric finite element spaces. This gives the semi-discrete formulation of the variational problem stated in Eq. (2): Find $(\boldsymbol{u}_h^f, p_h) \in \boldsymbol{U}_h \times Q_h$ such that

$$\left( \rho \frac{\partial \boldsymbol{u}_h^f}{\partial t}, \boldsymbol{v}_h \right) + c(\boldsymbol{u}_h^f; \boldsymbol{u}_h^f, \boldsymbol{v}_h) + a(\boldsymbol{u}_h^f, \boldsymbol{u}_h^f) + b(p, \boldsymbol{v}_h) + b(q, \boldsymbol{u}_h^f) = f(\boldsymbol{v}_h) \qquad (3)$$

for all $(\boldsymbol{v}_h, q_h) \in \boldsymbol{V}_h \times Q_h$.

As described in [12] we have developed a block-structured B-spline isogeo-metric finite element approximation of the Navier-Stokes equations described above. A domain $\Omega$ can be subdivided into a number of patches $\Omega_e$ such that $\Omega = \cup_{e=1}^{N} \Omega_e$, where what we call a patch is equivalent to a block. To construct a B-spline basis for $\Omega$ we associate for each patch a knot-vector in each coordinate direction

$$\Xi_k^e = \left\{ \xi_{1,k}^e, \xi_{2,k}^e, \ldots, \xi_{n_k^e+p_k^e+1}^e \right\}$$

for $k = 1, \ldots, d$. The B-spline basis for patch $\Omega_e$ on the parametric domain $\hat{\Omega} = (0,1)^d$ is written as $\hat{\boldsymbol{S}}_{\boldsymbol{\alpha}^e}^{\boldsymbol{p}^e}$ where the multi-indices $\boldsymbol{\alpha}^e = (\alpha_1^e, \ldots, \alpha_d^e)$ and $\boldsymbol{p}^e = (p_1^e, \ldots, p_d^e)$ denote the regularity and order for the basis in each coordinate direction, respectively. The corresponding basis for the physical domain $\Omega_e$ can be expressed using the coordinate mapping $\phi_e : \hat{\Omega} \to \Omega_e$ as

$$\boldsymbol{S}_{\boldsymbol{\alpha}^e}^{\boldsymbol{p}^e} = \left\{ v_h \mid v_h \circ \boldsymbol{\phi}_e \in \hat{\boldsymbol{S}}_{\boldsymbol{\alpha}^e}^{\boldsymbol{p}^e} \right\}.$$

If the variational formulation allows a discontinuous approximation the spline finite element basis for the domain $\Omega$ can be defined as

$$\boldsymbol{S}_h = \left\{ v_h \mid v_{h|\Omega_e} \in \boldsymbol{S}_{\boldsymbol{\alpha}^e}^{\boldsymbol{p}^e} \right\}.$$

If we assume that the knot-vectors and geometrical mapping $\boldsymbol{\phi}_e$ for all the patches are consistent on common edges and faces we can define a continuous basis

$$\boldsymbol{S_h} = \left\{ v_h \in C(\Omega) \mid v_{h|\Omega_e} \in \boldsymbol{S}_{\boldsymbol{\alpha}^e}^{\boldsymbol{p}^e} \right\}.$$

We use the same basis for the geometry as for the discretization of the velocity and the pressure.

### 2.1.2. Projection method

In order to solve the mixed variational problem given in Eq. (3) the following inf-sup condition

$$\inf_{q_h \in Q_h, q_h \neq 0} \sup_{\boldsymbol{v}_h \in \boldsymbol{V}_h, \boldsymbol{v}_h \neq 0} \frac{b(q_h, \boldsymbol{v}_h)}{\|q_h\|_{L^2(\Omega)} \|\boldsymbol{v}_h\|_{\boldsymbol{H}^1(\Omega)}} \geq C > 0.$$

needs to be satisfied in order to avoid spurious pressure modes [13]. This imposes restrictions on the choices of $\boldsymbol{V}_h$ and $Q_h$.

Traditionally a mixed finite element method with different approximation spaces for pressure and velocity is required. In this work we use a pressure correction projection scheme which allows for equal-order approximation of the velocity and pressure. This is based on the work pioneered by Chorin [14] and Temam [15] in the late 1960s. In order to stabilize the equal-order approximation we employ Minev stabilization as described in [16]. A backward differentiation formula of order 2 (BDF2 scheme) is used for the time integration.

## 2.2. Structural solver

In a Lagrangian description, the balance equation (conservation of linear momentum) of the structure can be written as

$$\rho^s \frac{\partial^2 \boldsymbol{u}^s}{\partial t^2} = \nabla \cdot \left( J \boldsymbol{F}^{-1} \cdot \boldsymbol{\sigma}(\boldsymbol{u}^s) \right) + \rho^s \boldsymbol{g} \quad \text{in } \Omega^s, \tag{4}$$

where $\boldsymbol{u}^s$ denotes the displacement of the structure, $\rho^s$ is the mass density, and $\boldsymbol{g}$ is the gravitation vector. The deformation gradient tensor, $\boldsymbol{F}$, is given by

$$\boldsymbol{F} = \boldsymbol{I} + \frac{\partial \boldsymbol{u}^s}{\partial \boldsymbol{X}} = \boldsymbol{I} + \nabla \boldsymbol{u}^s,$$

and $J = \det \boldsymbol{F}$.

We use a Total Lagrangian formulation for the structural solver, in which the second Piola-Kirchhoff stress tensor ($\boldsymbol{S}$) is a more convenient stress measure in the constitutive relation. It is related to the Cauchy stress tensor ($\boldsymbol{\sigma}$) through

$$\boldsymbol{\sigma} = \frac{1}{J} \boldsymbol{F} \cdot \boldsymbol{S} \cdot \boldsymbol{F}^T.$$

Assuming isotropic linear-elastic material, the constitutive relation for the structure can be written

$$\boldsymbol{S} = \lambda^s (\text{Tr} \, \boldsymbol{E}) \boldsymbol{I} + 2\mu^s \boldsymbol{E},$$

where $\boldsymbol{E}$ denotes the Green-Lagrange strain tensor

$$\boldsymbol{E}(\boldsymbol{u}^s) = \frac{1}{2}(\boldsymbol{F}^T \boldsymbol{F} - \boldsymbol{I}).$$

Furthermore, $\lambda^s$ and $\mu^s$ are the Lamé coefficients defined by

$$\lambda^s = \frac{\nu^s E}{(1+\nu^s)(1-2\nu^s)}, \qquad \mu^s = \frac{E}{2(1+\nu^s)}, \tag{5}$$

where $E$ and $\nu^s$ are the Young's modulus the Poisson's ratio, respectively.

The weak form of Equation (4) is obtained by taking the product with a test function $\boldsymbol{v}^s$, and integrating over the undeformed reference configuration, $\Omega_0^s$. This results in

$$\int_{\Omega_0^s} \rho^s \frac{\partial^2 \boldsymbol{u}^s}{\partial t^2} \cdot \boldsymbol{v}^s \mathrm{d}\boldsymbol{X} + \int_{\Omega_0^s} \boldsymbol{S}(\boldsymbol{u}^s) : \boldsymbol{E}(\boldsymbol{v}^s) \mathrm{d}\boldsymbol{X}$$

$$= \int_{\Omega_0^s} \rho^s \boldsymbol{g} \cdot \boldsymbol{v}^s \mathrm{d}\boldsymbol{X} + \int_{\Gamma_0^s} \bar{\boldsymbol{t}} \cdot \boldsymbol{v}^s \mathrm{d}\boldsymbol{X}, \tag{6}$$

where $\bar{\boldsymbol{t}}$ is the prescribed traction vector on the Neumann boundary $\Gamma^s$.

The structural problem is solved by integrating in time the linearized version of Equation (6), using a BDF2 scheme. Alternatively, the Hilber–Hughes–Taylor method [17] may be employed, but has not been used in the current study. As of the fluid solver, an isogeometric FE discretization based on spline basis functions is used in the numerical implementation.

## 2.3. Solver coupling

We couple the fluid and the structural solver at the interface using a Dirichlet-Neumann coupling as presented in [18]. The coupling conditions are

$$\boldsymbol{v}_\Gamma^f = \frac{\mathrm{d}\boldsymbol{u}_\Gamma}{\mathrm{d}t}$$

$$\boldsymbol{\sigma}_\Gamma^f \cdot \boldsymbol{n} = \boldsymbol{\sigma}_\Gamma^s \cdot \boldsymbol{n},$$

where $\boldsymbol{n}$ is the unit normal vector to the interface $\Gamma$.

For the benchmark case we investigate we have $\rho^f = 0.1\rho^s$, i.e. the fluid density is relatively large compared to the structural density. This known to give added mass effects [19, 20], and such cases can have slow convergence [21]. To stabilize the partitioned approach we use relaxation [22] and define a convergence criteria for the subiterations as

$$c\left(\boldsymbol{d}_{\Gamma,i}^{n+1}, \boldsymbol{d}_{\Gamma,i+1}^{n+1}\right) = \frac{\max_j \left(\left|\boldsymbol{d}_{\Gamma,i+1}^{n+1} - \boldsymbol{d}_{\Gamma,i}^{n+1}\right|\right)_j}{\max_j \left(\left|\boldsymbol{d}_{\Gamma,i+1}^{n+1}\right|\right)_j} < \epsilon_{\text{subit}},$$

where we use a convergence criteria of $\epsilon_{\text{subit}} = 10^{-6}$ for all the simulations in this paper.

Next the partitioned algorithm for solving the FSI problem is presented. Equal time step size $\Delta t$ is applied for both the fluid and structural fields. Furthermore, we define $n_{\max}$ as the maximum number of subiterations. For every time step we use the algorithm

1: **while** $c\left(\boldsymbol{d}_{\Gamma,i}^{n+1}, \boldsymbol{d}_{\Gamma,i+1}^{n+1}\right) > \epsilon_{\text{subit}}$ and $n+1 <= n_{\max}$ **do**

2:  Solve fluid problem and determine fluid forces on the interface $\tilde{\boldsymbol{f}}_{\Gamma,i+1}^{n+1}\left(\boldsymbol{d}_{\Gamma,i}^{n+1}\right)$.

3:  Transfer relaxed fluid forces to the structural solver

$$\boldsymbol{f}_{\Gamma,i+1}^{n+1} = \omega_i \tilde{\boldsymbol{f}}_{\Gamma,i+1}^{n+1} + (1-\omega_i)\boldsymbol{f}_{\Gamma,i}^{n+1}$$

4:  Solve structural problem for structural displacements $\tilde{\boldsymbol{d}}_{i+1}^{n+1}$

5:  Check convergence

6:  Solve grid problem for the new positions

7:  Compute the new grid velocity

8:  Derive new fluid velocity along surface to be used as Dirichlet boundary condition

9: **end while**

For all subiterations the relaxation parameter $\omega$ is kept constant.

## 2.4. Arbitrary Lagrangian-Eulerian description and mesh movement

We employ the Arbitrary Lagrangian-Eulerian (ALE) concept, as first presented in [7], to handle the movement of the structure within the fluid mesh. Our implementation of the ALE concept herein are based on the work done earlier by our group, see [23], [24] and [25]. For more information about the ALE concept we refer to [26], [8], [27] and [28]. The ALE description uses a reference domain which we denote $\hat{\Omega}^d$. Coordinates in the reference domain are

written $\hat{\boldsymbol{x}}$. Following the notation used in [28] the fluid spatial domain $\Omega_t^f$ is given by

$$\Omega_t^f = \left\{ \boldsymbol{x} \mid \boldsymbol{x} = \boldsymbol{\phi}(\hat{\boldsymbol{x}}, t) \; \forall \hat{\boldsymbol{x}} \in \hat{\Omega}, \, t \in (0, T) \right\},$$

and the mapping used is given by

$$\boldsymbol{\phi}(\hat{\boldsymbol{x}}, t) = \hat{\boldsymbol{x}} + \hat{\boldsymbol{y}}(\hat{\boldsymbol{x}}, t).$$

Here, $\hat{\boldsymbol{y}}$ is the time-dependent displacement of the reference fluid domain. The fluid domain velocity is thus given by

$$\hat{\boldsymbol{u}}^f = \left. \frac{\partial \hat{\boldsymbol{y}}}{\partial t} \right|_{\hat{x}},$$

and is taken while $\hat{\boldsymbol{x}}$ is being held fixed. The ALE description of the incompressible Navier-Stokes equations can now be written as

$$\rho \left. \frac{\partial \boldsymbol{u}^f}{\partial t} \right|_{\hat{x}} + \rho \left( \left( \boldsymbol{u}^f - \hat{\boldsymbol{u}}^f \right) \cdot \nabla \right) \boldsymbol{u}^f - \nabla \cdot \boldsymbol{\sigma} \left( \boldsymbol{u}^f, p \right) = \rho \boldsymbol{f} \quad \text{in } \Omega^f$$

$$\nabla \cdot \boldsymbol{u}^f = 0 \quad \text{in } \Omega^f. \tag{7}$$

However, for successful application of the ALE description a mesh movement algorithm is needed. Herein, we solve a linear elasticity problem at each time step. Our implementation is based on the developments made by our group first presented in [25] and later extended to handle two moving structures in [29]. A similar approach is used in [30]. Regarding the stability of the chosen mesh movement approach we refer to [26]. The linear elasticity equations can be written as

$$\nabla \cdot \boldsymbol{\sigma}^s + \boldsymbol{f} = \boldsymbol{0} \quad \text{on } \Omega,$$

where $\boldsymbol{\sigma}$ is the Cauchy stress tensor and $\boldsymbol{f}$ is the external force. The Cauchy stress tensor for an isotropic material and for linear elasticity reads

$$\boldsymbol{\sigma}^s = 2\mu^s \boldsymbol{\varepsilon}(\boldsymbol{u}) + \lambda^s \operatorname{Tr}(\boldsymbol{\varepsilon}) \boldsymbol{I},$$

where $\lambda^s$ and $\mu^s$ are the Lamé constants, $\boldsymbol{u}$ the displacement, $\boldsymbol{I}$ the identity tensor and $\boldsymbol{\varepsilon}(\boldsymbol{u})$ the strain tensor. The strain tensor is given by

$$\boldsymbol{\varepsilon}(\boldsymbol{u}) \frac{1}{2} \left( \nabla \boldsymbol{u} + ((\nabla \boldsymbol{u})^T \right),$$

and the Lamé coefficients are defined in Eq. (5) Here, $\nu^s$ is the Poisson ratio and $E$ the Young modulus. We will specify our mesh problem through these two parameters. Notice, that we might alternatively use a non-linear elasticity solver, similar to the one used to solve the structural displacements above, in the mesh movement algorithm. However, in our numerical tests the linear solver turned out to be more robust.

### 2.5. Mesh generation

Generation of a high quality block-structured mesh can often be challenging. The computational domain shall be decomposed into 2D quadrilaterals which are not too skewed or distorted. Furthermore, distorted elements and abrupt changes in the element size should be avoided. Such cases can lead to unwanted grid effects. Also, we would like to have smaller elements at parts of the boundary with high curvature and close to solid walls in order to capture boundary layers.

*2.5.1. Block-structured mesh generation*

A bottom-up approach is often preferred for constructing a block-structured mesh. For two-dimensional problems the procedure can be described as

1. Define the corner nodes for the blocks.
2. Connect the corners to form the edges.
3. Refine the edges with a suitable grading.
4. Connect the edges to form surfaces.

To define the grading of the mesh a geometrical factor $r$ can be defined as the ratio of the element size of two consecutive elements, i.e. if $\{\boldsymbol{x}_i\}_{i=1}^m$ are the points on the edge or curve and $\Delta s_i = \|\boldsymbol{x}_i - \boldsymbol{x}_{i-1}\|_2$ defines the cell size, then

$$r = \Delta s_i / \Delta s_{i-1},$$

for $i = 2, \ldots, m$. To impose a smooth change in element size, we typically have that $0.8 < r < 1.2$, and for sharp boundary layers we may even use $0.9 < r < 1.1$ to capture the rapid change in the solution.

*2.5.2. Spline curves*

In this section we define spline curves, which form the foundation of the mesh generation, as in [11]. Assume that we have a knot-vector

$$\Xi = \{0 = \xi_1, \xi_2, \ldots, \xi_{n+p+1} = 1\}.$$

and a set of control points $\boldsymbol{C} = \{\boldsymbol{c}_1, \ldots, \boldsymbol{c}_n\}$ which defines the spline curve

$$\boldsymbol{c}(\xi) = \sum_{i=1}^n \boldsymbol{c}_i B_{i,p}(\xi),$$

where $\{B_i\}_{i=1}^n$ are the basis functions. The parameter $p$ is the polynomial order of the spline curve, and each knot $\xi_i$ may be repeated several times, but the knot-span should be non-decreasing

$$\xi_1 \leq \xi_2 \leq \cdots \leq \xi_{n+p+1}.$$

For $p = 0$ the basis functions are piecewise constants

$$B_{i,0}(\xi) = \begin{cases} 1, & \xi_i \leq \xi < \xi_{i+1}, \\ 0 & \text{otherwise.} \end{cases}$$

The higher order B-spline basis functions are defined as a linear combination of splines of lower order using the *Cox-de Boor recursion formula*

$$B_{i,p}(\xi) = \frac{\xi - \xi_i}{\xi_{i+p} - \xi_i} B_{i,p-1}(\xi) + \frac{\xi_{i+p+1} - \xi}{\xi_{i+p+1} - \xi_{i+1}} B_{i+1,p-1}(\xi). \tag{8}$$

We restrict our attention to *open* knot-vectors, i.e. splines that are interpolatory at the end points, and then the first and last knots are repeated $p+1$ times. Furthermore, if the spline is $C^{p-1}$ continuous then all the internal knots have multiplicity one and the knot-vector can be written as

$$\Xi = \{\underbrace{\xi_1, \ldots, \xi_1}_{p+1}, \xi_2, \ldots, \xi_{m-1}, \underbrace{\xi_m, \ldots \xi_m}_{p+1}\},$$

where the number of unique knots is given by $q = n - p + 1$. The corresponding knot-vector without repeated knots is

$$\bar{\Xi} = \{\bar{\xi}_1, \bar{\xi}_2, \ldots, \bar{\xi}_q\}.$$

8

The mesh generation process is dependent on standard cubic spline inter-polation [31]. The starting point is a set of $m$ points $\{\boldsymbol{x}_i\}_{i=1}^m$ that we want to approximate by a cubic spline curve $\boldsymbol{c}(\xi)$ such that

- $\boldsymbol{c}(\tilde{\xi}_i) = \boldsymbol{x}_i$ for $\tilde{\xi}_i \in [0, 1]$.

- $\boldsymbol{c}(\xi) \in \boldsymbol{C}^2([0, 1])$.

The points $\{\tilde{\xi}_i\}_{i=1}^q$ where the spline curve interpolates the data are called the *Greville points*. Two extra conditions are needed to uniquely define the inter-polation. We use either Hermitian ($\boldsymbol{c}'(0) = \boldsymbol{t}_0, \boldsymbol{c}'(1) = \boldsymbol{t}_1$) or natural boundary conditions ($\boldsymbol{c}''(0) = \boldsymbol{c}''(1) = 0$), where $\boldsymbol{t}_0$ and $\boldsymbol{t}_1$ are the tangent vectors of the spline curve at the endpoints. This leads to an $n \times n$ linear system with $n = m + 2$, which can be solved for the unknown control points $\{\boldsymbol{c}_i\}_{i=1}^n$. The interpolation is not uniquely defined since the parametrization can be different.

The entire meshes presented in this paper are made for polynomial order $p = 3$, and only lowered to orders $p = 1$ and $p = 2$ once all patches and refinements have been completed.

### 2.5.4. Surface generation

For surface generation we employ the concept of Coons patches [32]. Given four boundary curves $\boldsymbol{u}_0(\xi)$, $\boldsymbol{u}_1(\xi)$, $\boldsymbol{w}_0(\eta)$, $\boldsymbol{w}_1(\eta)$ as given in Figure 1. These



Figure 1: Boundary curves for Coons surface patch.

curves have normalized knot vectors and are connected such that $\boldsymbol{u}_0(\xi_1) = \boldsymbol{w}_0(0)$, $\boldsymbol{u}_0(1) = \boldsymbol{w}_1(0)$, $\boldsymbol{u}_1(1) = \boldsymbol{w}_1(1)$, $\boldsymbol{u}_1(0) = \boldsymbol{w}_0(1)$, thus forming a closed loop. By defining the surfaces

$$S_1(\xi, \eta) = (1 - \eta)\boldsymbol{u}_0(\xi) + \eta\boldsymbol{u}_1(\xi)$$
$$S_2(\xi, \eta) = (1 - \eta)\boldsymbol{w}_0(\eta) + \xi\boldsymbol{w}_1(\eta)$$
$$S_3(\xi, \eta) = (1 - \xi)(1 - \eta)\boldsymbol{u}_0(0) + \xi(1 - \eta)\boldsymbol{u}_0(1) + \eta(1 - \xi)\boldsymbol{u}_1(0) + \xi\eta\boldsymbol{u}_1(1)$$

the Coons surface paths is given by

$$S_c(\xi, \eta) = S_1(\xi, \eta) + S_2(\xi, \eta) - S_3(\xi, \eta).$$

The Coons surface patch approach is a quick and easy way of building the surfaces. Being able to define the geometry through the boundary curves of each surface or patch is a great advantage.

We calculate mean value and amplitude of the time-dependent quantities as in [9]. The mean value of quantity $x$ is denoted $\bar{x}$ and calculated from last period of oscillations as

$$\bar{x} = \frac{1}{2}(x_{\max} + x_{\min}).$$

Similarly, the amplitude of quantity $x$ is denoted $x_{\mathrm{amp}}$ and calculated as

$$x_{\mathrm{amp}} = \frac{1}{2}(x_{\max} - x_{\min}).$$

Frequencies are calculated by the Lomb-Scargle algorithm [33, 34].

## 3. Simulation setup

### 3.1. Problem description

In this paper we aim to simulate the FSI2 benchmark case defined in [9], with updated results given in [10], with our isogeometric code IFEM. The benchmark case is defined for flow past a fixed circular cylinder with a flexible bar attached, see Figure 2. The computational domain is identical to the domain in [9], except
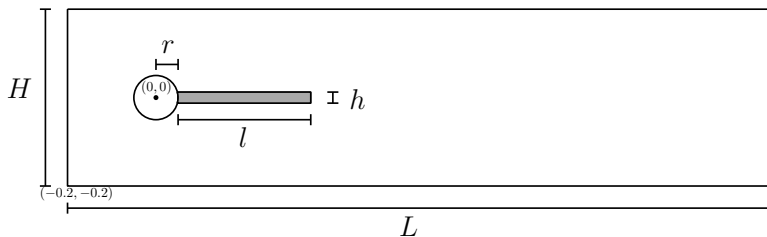


Figure 2: Cyl2DBar: Computational domain. The dimensions are $H = 0.41$, $L = 2.5$, $r = 0.05$, $h = 0.02$ and $l = 0.35$.

that the origin is shifted from the lower left corner to the centre of the cylinder.

Inflow is from the left only and we prescribe a parabolic velocity profile

$$v_x^{\mathrm{in}}(0, y) = 1.5\bar{U}\frac{(y + 0.2)(H - (y + 0.2))}{\left(\frac{H}{2}\right)^2}$$
$$= 1.5\bar{U}\frac{4.0}{0.1681}(y + 0.2)(0.41 - (y + 0.2)), \tag{9}$$

where $\bar{U}$ is the mean inflow velocity. The top and bottom wall, circle and fluid-structure interface $\Gamma_t^0$ is prescribed the no-slip condition. At the outflow, i.e. the right boundary, the pressure is prescribed to be 0.

The inflow velocity is ramped up through as smooth increase of the velocity profile as suggested in [9] through

$$v_x^{\mathrm{in}}(t, 0, y) = \begin{cases} v_x^{\mathrm{in}}(0, y)\frac{1 - \cos(\frac{\pi}{2}t)}{2} & \text{if } t < 5.0 \\ v_x^{\mathrm{in}}(0, y) & \text{otherwise.} \end{cases}$$

10

Our main quantities of interest are the vertical position, $y(t)$, of the end of the flexible bar, identified by the letter $A$ in Figure 3, and the lift, $F_L$, and drag forces, $F_D$, on the cylinder and flexible bar considered as one single object. The coordinates of the reference point A at time $t = 0$ is $(0.4, 0)$. The drag and
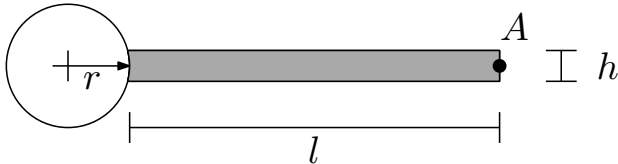


Figure 3: Cyl2DBar: Structural part of the domain

lift forces, $F_D$ and $F_L$ are the horizontal and vertical force components acting on the cylinder and flexible bar respectively, $\rho$ is the density of the fluid, $l$ is the length in the spanwise direction and $p_\infty$ is the ambient pressure. The force components are computed as

$$F = [F_D, F_L]^T = \int_\Gamma \boldsymbol{\sigma} \cdot \boldsymbol{n} \, \mathrm{d}\boldsymbol{s},$$

where $\Gamma$ is the surface of the cylinder and the flexible bar.

The flow and material properties given in Table 1 are used throughout the simulations. As can be incurred from the table, the Reynolds number for all

Table 1: Cyl2DBar: Flow and material properties.

| Parameter | Quantity | Unit |
|-----------|----------|------|
| $\rho^s$ | 10000 | kg/m$^3$ |
| $\nu^s$ | 0.4 | - |
| $E^s$ | $1.4 \cdot 10^6$ | Pa |
| $\rho^f$ | 1000 | kg/m$^3$ |
| $\nu^f$ | 0.001 | m$^2$/s |
| $\bar{U}$ | 1.0 | m/s |

simulations is 100.

## 3.2. Mesh description

The patch structure along with the refinement edges $e_1 - e_8$ are shown in Figure 4. Detailed refinement information can be found in Table 2.

The resulting number of elements and degrees-of-freedom for the different meshes and polynomial orders are shown in Table 3. The meshes are designed such that the number of fluid and structural elements double for each refinement level.

The mesh for the coarsest grid, G1, for $p = 2$ along with a zoomed view of the mesh close to the cylinder and the flexible are shown in Figure 5. In both figures the fluid domain is light blue, whilst the structural domain is light red.
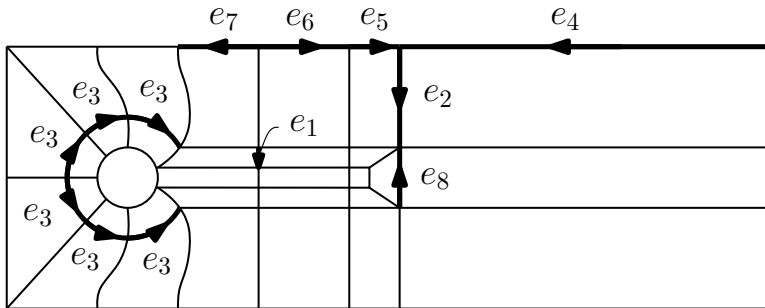
Figure 4: Cyl2DBar: Refinement edges.

Table 2: Cyl2DBar: Detailed refinement information for the simulations meshes. Edge grading factor is given by $r$ and $n$ is the number of inserted knots along the given edge.

| Edge / Mesh | | G1 | G2 | G3 | G4 | G5 |
|---|---|---|---|---|---|---|
| $e_1$ | $r$ | 0.61 | 0.74 | 0.82 | 0.909 | 0.9605 |
| | $n$ | 5 | 7 | 9 | 13 | 18 |
| $e_2$ | $r$ | 1.0 | 1.0 | 0.97 | 0.97 | 0.97 |
| | $n$ | 5 | 7 | 8 | 13 | 20 |
| $e_3$ | $r$ | 1.0 | 1.0 | 1.0 | 1.0 | 1.0 |
| | $n$ | 2 | 4 | 7 | 10 | 15 |
| $e_4$ | $r$ | 0.94 | 0.97 | 0.99 | 0.985 | 0.99 |
| | $n$ | 25 | 40 | 80 | 98 | 133 |
| $e_5$ | $r$ | 1.0 | 1.0 | 1.0 | 1.0 | 1.0 |
| | $n$ | 2 | 3 | 5 | 7 | 9 |
| $e_6$ | $r$ | 0.95 | 0.96 | 0.97 | 0.96 | 0.96 |
| | $n$ | 4 | 6 | 8 | 15 | 20 |
| $e_7$ | $r$ | 1.0 | 1.0 | 1.0 | 1.0 | 1.0 |
| | $n$ | 4 | 6 | 8 | 12 | 18 |
| $e_8$ | $r$ | 1.0 | 1.0 | 1.0 | 1.0 | 1.0 |
| | $n$ | 3 | 5 | 7 | 10 | 15 |

### 3.3. Time step determination

All simulations use a non-dimensional time step of $\Delta t = 0.025$ and a fixed relaxation parameter $\omega = 0.1$.

### 3.4. Simulation length

We run all simulations up till non-dimensional time 200, i.e. 8000 time steps. A plot of the cumulative standard deviation is shown in Figure 6 for grid G1. This indicates that the simulations are run long enough.

Table 3: Cyl2DBar: Number of elements and degrees-of-freedom for simulation meshes G1-G5 and polynomial orders $p = 1, 2, 3$.

| Mesh | $p$ | Structure $n_{\mathrm{el}}$ | $n_{\mathrm{dof}}$ | Fluid $n_{\mathrm{el}}$ | $n_{\mathrm{dof}}$ |
|------|-----|------|------|------|------|
| G1 | 1 | 52 | 140 | 1936 | 3144 |
| G2 | 1 | 108 | 266 | 4012 | 6381 |
| G3 | 1 | 192 | 450 | 8020 | 12612 |
| G4 | 1 | 407 | 912 | 15870 | 24597 |
| G5 | 1 | 800 | 1734 | 31832 | 48849 |
| G1 | 2 | 52 | 204 | 1936 | 4281 |
| G2 | 2 | 108 | 352 | 4012 | 7959 |
| G3 | 2 | 192 | 560 | 8020 | 14862 |
| G4 | 2 | 407 | 1066 | 15870 | 27657 |
| G5 | 2 | 800 | 1944 | 31832 | 53079 |
| G1 | 3 | 52 | 280 | 1936 | 5586 |
| G2 | 3 | 108 | 450 | 4012 | 9705 |
| G3 | 3 | 192 | 682 | 8020 | 17280 |
| G4 | 3 | 407 | 1232 | 15870 | 30885 |
| G5 | 3 | 800 | 2166 | 31832 | 57477 |
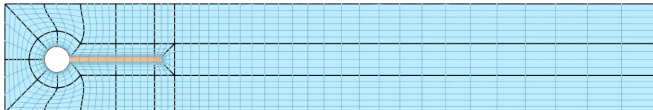


(a) Cyl2DBar: Mesh G1, $p = 2$.
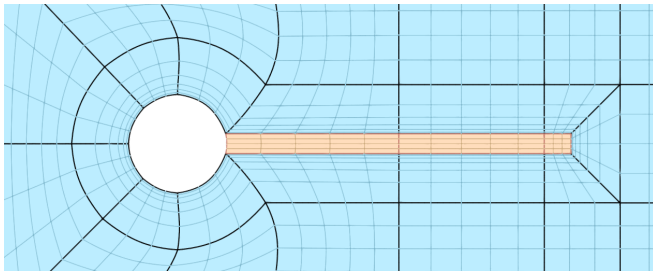


(b) Cyl2DBar: Zoomed view of mesh G1 close to the cylinder and the flexible bar, $p = 2$.

Figure 5: Cyl2DBar: Grid G1. The fluid domain is light blue and the structural domain is light. Patch boundaries are drawn with thick black lines.

### 3.5. Mesh stiffness

Ensuring mesh quality consistent with the model in use is the key to getting accurate results. In the case we are interested in the geometry is expected to undergo deformations and hence the mesh elements can change in shape and size. Fortunately, the quality of the mesh can still be controlled by cleverly

13
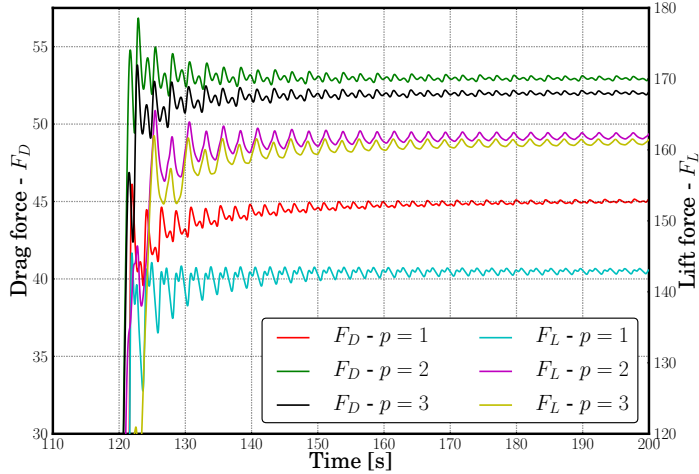
Figure 6: Cyl2DBar: Cumulative standard deviation for grid G1 calculated from $t = 120$.

choosing the distribution of mesh stiffness throughout the mesh domain. When a constant value of mesh stiffness is applied, specified displacements are homogeneously diffused throughout the mesh. On the other hand when the mesh stiffness is specified as varying throughout the domain, nodes in regions of high stiffness move together, i.e. there is little relative motion. Variable mesh stiffness is particularly useful to preserve the mesh distribution (and quality) near fine geometrical features, such as sharp corners, or in boundary layers. In principle, the computed spatio-temporal deflections, drag and lift force should be independent of the choice of mesh stiffness distribution. However, it has been observed that some mesh distributions, like constant mesh stiffness everywhere, resulted in divergence in solution. In this work seven different stiffness distributions were tried. In all the cases the mesh stiffness distribution was maximum close to the wall so that the initial mesh quality in the vicinity is preserved over the full course of simulation and then it decreased as a function of the distance from the wall $r$ to zero. A plot of the $r$ value for grid G1 is shown in Figure 7. Expressions given below give a mathematical description of the mesh stiffness as a function of $r$.

1. Base case: $E_{\mathrm{bc}} = 1 + 200e^{-100r}$
2. $E_1 = 1 + 200e^{-50r}$
3. $E_2 = 1 + 1000e^{-100r}$
4. $E_3 = \begin{cases} 201 & \text{if } r < 0.025 \\ 1 + 200e^{-100(r-0.025)} & \text{otherwise} \end{cases}$
5. $E_4 = \begin{cases} 201 & \text{if } r < 0.015 \\ 1 + 200e^{-100(r-0.015)} & \text{otherwise} \end{cases}$

14
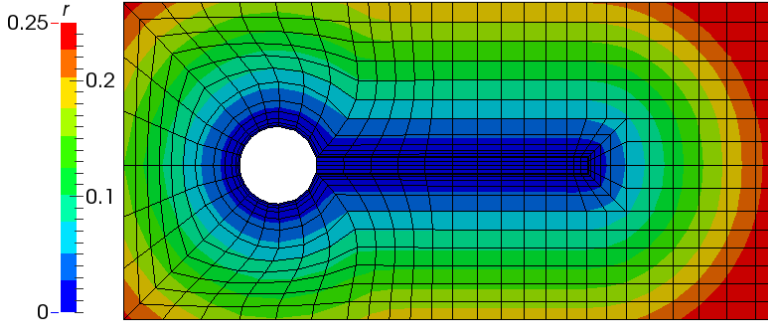
Figure 7: Cyl2DBar: Calculated wall distance for grid G1.

6. $E_5 = \begin{cases} 201 & \text{if } r < 0.035 \\ 1 + 200e^{-100(r-0.035)} & \text{otherwise} \end{cases}$

7. $E_6 = \begin{cases} 1001 & \text{if } r < 0.035 \\ 1 + 1000e^{-100(r-0.035)} & \text{otherwise} \end{cases}$

Stiffness contours are presented in Figure 8 and a more quantitative profile of the stiffness as a function of the distance $r$ is given by the Figure 9 for grid G3 for easier comparison. $E_{bc}$ is the least stiff mesh while $E_6$ is the stiffest mesh of all the cases simulated here. The basecase mesh stiffness has been used for all other simulations in this paper, and it was chosen based on experience of stability and required solution time.

*3.6. Definition of test cases*

Effects of changing the order of the elements (linear, quadratic and cubic) was investigated for five different mesh resolutions resulting in a total of fifteen simulations. Six additional simulations were conducted to understand the effect of changing the mesh stiffness.

## 4. Results and discussion

A comparison of lift, drag and displacements with respect to grid resolution and element order is presented here. Although the computational efficiency was not the focus of attention in this work we include this information for one particular grid. Finally, a subsection demonstrates the effect of changing the mesh stiffness.

*4.1. Mesh stiffness and quality*

The accuracy of simulation involving stationary bodies depend on the quality of the rigid mesh. However, for an FSI simulation involving deformations of solid bodies it is necessary to ensure that all the intermediate mesh configurations resulting during such movements are of high quality. To this effect, during the mesh generation step we applied four different criteria to obtain high quality

15
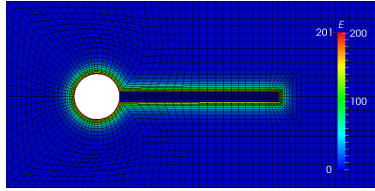
(a) $E_{\mathrm{bc}}$
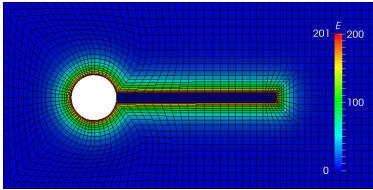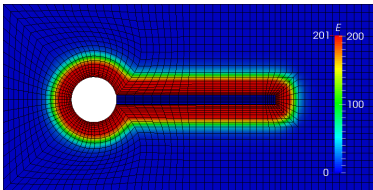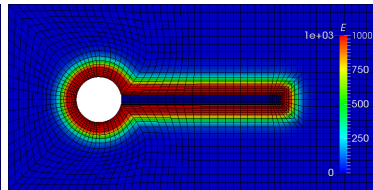
(b) $E_1$
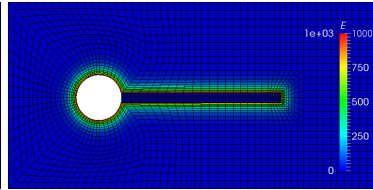
(c) $E_2$
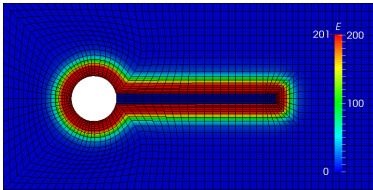
(d) $E_3$
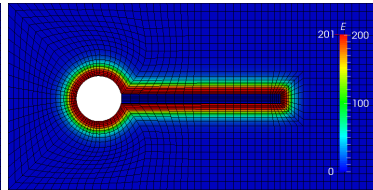
(e) $E_4$

(f) $E_5$

(g) $E_6$

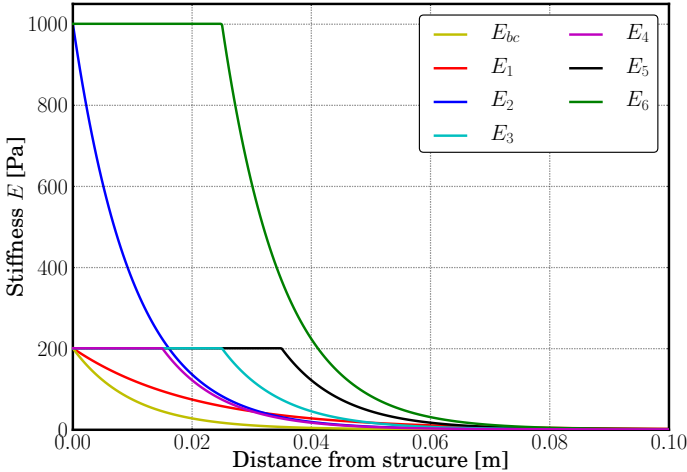Figure 8: Cyl2DBar: Mesh stiffness distributions for grid G3.

16

Figure 9: Cyl2DBar: Different mesh stiffnesses investigated.

meshes. It is worth mentioning that we have used only quadrilateral elements in all the simulations. Therefore, all subsequently mentioned mesh quality metrics are for quadrilaterals. In this paper we use four different mesh metrics for assessing the quality of the finite element meshes. Firstly, the scaled Jacobian can vary from −1 to 1 [35]. A positive value is necessary for the mesh to have the minimum quality. Typically, the acceptable range is [0.3, 1] [36]. A negative value signals an invalid element. Secondly, the shape quality metric is defined in [37]. This metric attains the value 1 if the quadrilateral is a square and 0 if it is degenerate. Thirdly, the skew quality metric is also defined in [37]. This metric aims to detect element distortions arising from large or small angles. It attains the value 1 if the quadrilateral is a rectangle and 0 if it is degenerate. Lastly, the stretch quality metric is a measure of the aspect ratio. This also attains values between 0 and 1.

Seven different mesh stiffness distribution were investigated and ensured that the mesh quality is maintained throughout the whole cycle considered. Although such investigations were conducted for all the grids and orders, in Figure 10 we just present the case for G3 grid and quadratic elements. The scaled Jacobian mesh metric for grid G3 is shown for the minimum quality element in Figure 10a. It is clear from the figure that the scaled Jacobian is always positive and therefore there are no intersecting grid lines which could result in unphysical results. The shape mesh metric for grid G3 is shown for the minimum quality element in Figure 10b. Since the boundary layer close to the solid structure was to be resolved, very fine resolution in the direction normal to the wall was required. It is therefore natural to expect that some cells close to the junction between cylinder and bar will have some degree of degeneracy. Similarly, the skew mesh metric for the worst quality element is
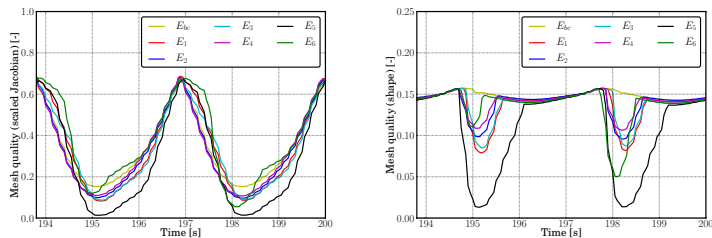
(a) Minimum of the scaled Jacobian mesh metric for grid G3 as a function of time

(b) Minimum of the shape mesh metric for grid G3 as a function of time
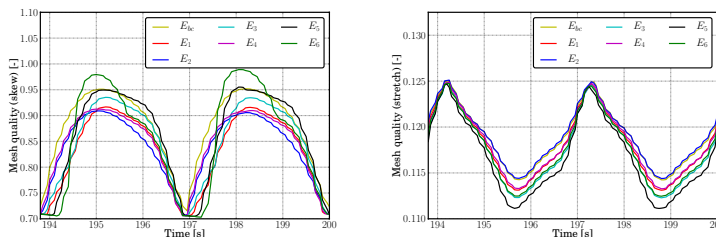
(c) Maximum of the skew mesh metric for grid G3 as a function of time

(d) Maximum of the stretch mesh metric for grid G3 as a function of time.

Figure 10: Cyl2DBar: Mesh quality

shown in Figure 10c. It is clear that even for the worst element the skewness value never gets below 0.7 throughout the cycle. Finally the stretch mesh metric for the worst quality element is shown in the Figure 10d. It is worth mentioning that the aspect ratio can easily be in of the order of $10^5$ and the solvers used in this work can easily handle such aspect ratios, see [12]. In light of that the stretch mesh metric is highly adorable. Satisfied with the quality of intermediate mesh configurations, seven different simulations were conducted to quantify the effects of different mesh stiffness distributions ($E_{bc}, E_1, E_2, E_3, E_4, E_5, E_6$). The results are presented in the Table 4. As expected all the different mesh stiffness distributions predicted the drag, lift and deformations characteristics within acceptable limits when compared to the reference data. We also investigate the differences in the total CPU time used by the simulations. The results are shown in Figure 11.

Also we investigate how the number of subiterations required at each time step is impacted by the mesh stiffness. A comparison plot is shown in Figure 12.

The qualitative differences between spline elements of order $p = 1$, $p = 2$ and $p = 3$ is shown in Figure 13 for grid G1 in a deformed state. It is clear from the figures that the use of higher order spline elements ($p = 2, 3$) gives an exact representation of the interface between the fluid and structure leading to smaller error when the forces are transferred at the interface.

Table 4: Cyl2DBar: Results for mesh stiffness investigations

|          | $F_D$  | $F_{D,\text{amp}}$ | $F_L$ | $F_{L,\text{amp}}$ | $u_x$     | $u_{x,\text{amp}}$ | $u_y$  | $u_{y,\text{amp}}$ |
|----------|--------|--------|-------|--------|-----------|--------|--------|--------|
| $E_{\text{bc}}$ | 214.94 | 78.97 | 1.20 | 230.5 | $-0.01486$ | 0.0128 | 0.0013 | 0.0813 |
| $E_1$    | 214.60 | 78.69 | 1.09 | 229.6 | $-0.01476$ | 0.0128 | 0.0013 | 0.0811 |
| $E_2$    | 214.80 | 79.03 | 1.21 | 230.6 | $-0.01485$ | 0.0128 | 0.0013 | 0.0813 |
| $E_3$    | 214.60 | 78.73 | 1.24 | 229.2 | $-0.01475$ | 0.0128 | 0.0013 | 0.0810 |
| $E_4$    | 214.79 | 78.89 | 1.23 | 229.9 | $-0.01481$ | 0.0128 | 0.0013 | 0.0812 |
| $E_5$    | 213.98 | 77.96 | 1.69 | 232.1 | $-0.01444$ | 0.0124 | 0.0013 | 0.0803 |
| $E_6$    | 214.49 | 78.67 | 1.19 | 229.7 | $-0.01475$ | 0.0128 | 0.0013 | 0.0811 |
| Ref.     | 215.06 | 77.65 | 0.61 | 237.8 | $-0.01485$ | 0.0127 | 0.0013 | 0.0817 |
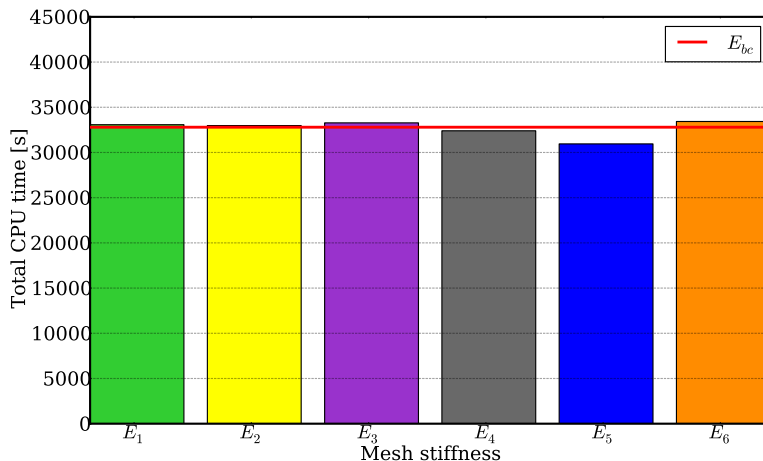


Figure 11: Cyl2DBar: Total CPU time for simulations with different mesh stiffness.

## 4.2. Velocity and pressure contours

Figures 14 and 15 give the velocity and pressure distribution, respectively, in the domain for a complete oscillation period $T$. One can notice the existence of a consistently high pressure on the leading side of the cylinder. The high pressure zone is created due to the impingement of flow on the surface of the cylinder. After the impingement the flow bifurcates and flows around the cylinder. In the absence of the bar on the trailing side, the flow would have reached a statistically steady state characterized by a repeating pattern of swirling vortices caused by the unsteady flow separation. The vortices shed on the upper side of the cylinder interact with those shed on the lower side giving rise to a von Karman vortex street. When the bar is attached to the cylinder such an interaction between the vortices is delayed. However, because of the elastic nature of the material and inherent instability in the flow the equilibrium of the bar is disturbed and it starts oscillating in an up-and-down motion. In Figure 15, one can see that for $t = 0T$ when the bar is in the uppermost extremity, the bar begins to obstruct the flow resulting in a retardation of flow and the development of a
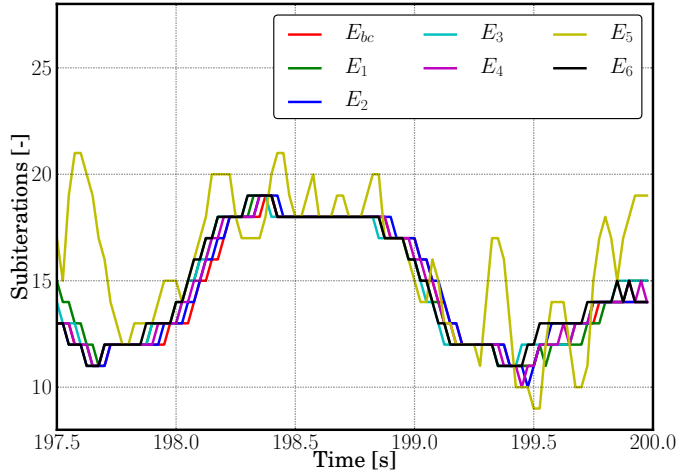
19

Figure 12: Cyl2DBar: Number of subiterations per time step for simulations with different mesh stiffness.

high pressure zone. A corresponding low pressure zone exists on the bottom side of the bar. The imbalance in the pressure on the two sides of the bar pushes the bar downward resulting in the neutralization of the pressure. However, as the bar starts approaching the horizontal position it, owing to inertia, continues to move downward. This results in the development of a high pressure zone on the lower side of the bar and the downward motion is stopped once the pressure value increases to a level where it can prevent further downward motion. At this point the motion once again sees a complete reversal in direction. In Figure 14 one can notice that the flow accelerates in the region close to the lateral surface of the bar when it attains a convex shape while the flow accelerates in the region close to the tip in the concave side. The flow on the either side of the bar thus accelerates on either side of the bar in a periodic fashion and have no interactions till they have passed a distance close the length of the bar.

### 4.3. Drag

Figure 16 gives a detailed comparison of the drag force for different grids and order of elements. Figure 16a shows the drag forces averaged over the last two cycles along with the variations over the cycles. It is clear that for quadratic and cubic elements ($p = 2, 3$) the predicted average drag forces are in excellent agreement with the reference data. For linear elements ($p = 1$), the grid resolution has a relatively bigger impact on the predicted drag. It is not entirely clear if grid independence was in fact realized or not. However, even with the coarsest grids, a switch to quadratic elements improves the prediction remarkably. It can also be inferred from the figure that quadratic elements are sufficient for producing the results in good agreement with the reference data.
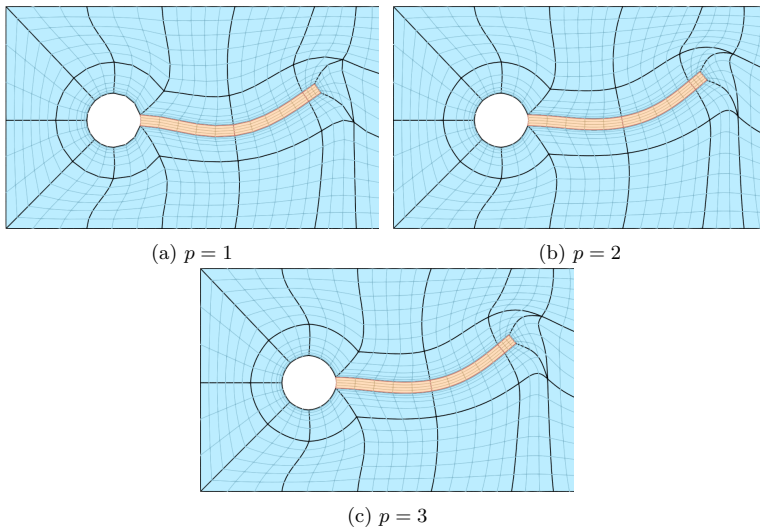
20

(a) $p = 1$

(b) $p = 2$

(c) $p = 3$

Figure 13: Cyl2DBar: Deformed G1 grid for spline element order $p = 1$, $p = 2$, $p = 3$.

Figure 16b, 16c and 16d give a better insight into the evolution of the drag forces over time. It appears that for linear elements different grids predict very different evolutions of the drag force. However, a promotion to quadratic elements diminishes the differences. Except for the coarsest grid G1, all the grids predict similar evolution. Further promotion to cubic elements results in the collapsing of all the evolution profiles of the drag force to a single curve. However, for both linear and quadratic elements a lag is noticed with respect to the reference profile. When one looks at Table 5, where all the frequency results are gathered, one finds that the predictions of drag frequency for quadratic and cubic elements are within 5% while the error goes up to 15% if linear elements are used with coarsest grid G1.

*4.4. Lift*

A detailed comparison of the lift forces for different grids and orders of elements with the reference data is presented in Figure 17. Figure 17a shows the lift forces averaged over the last two cycles along with the variations over the cycles. Because of the statistical symmetry in the case under symmetry the profile of lift over the upstroke should be exactly the same but opposite in direction during the downstroke. Therefore the lift force averaged over a full cycle will get cancelled resulting in zero net lift force. This can be seen in Figure 17a. Although the simulations conducted with linear elements did not result an exact cancellation of lift forces over a full cycle it is still very small. To get better insight into the evolution of lift forces as a function of time, the temporal profiles of lift, for different grids, for linear, quadratic and cubic elements are presented in Figures 17b, 17c and 17d respectively. It can be seen that for linear elements, grids G1, G2 and G3 show oscillations which vanish when the grid resolution is increased (G4 and G5). In fact the profiles of lift force for G4 and
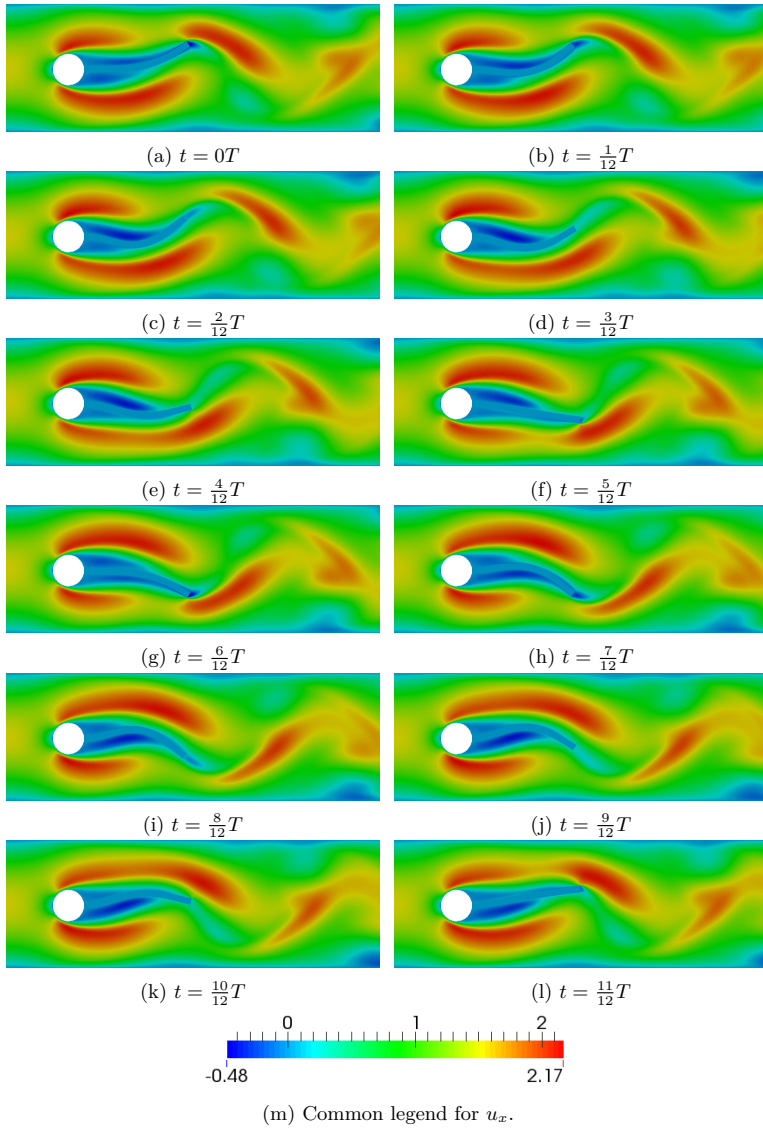
(a) $t = 0T$

(b) $t = \frac{1}{12}T$

(c) $t = \frac{2}{12}T$

(d) $t = \frac{3}{12}T$

(e) $t = \frac{4}{12}T$

(f) $t = \frac{5}{12}T$

(g) $t = \frac{6}{12}T$

(h) $t = \frac{7}{12}T$

(i) $t = \frac{8}{12}T$

(j) $t = \frac{9}{12}T$

(k) $t = \frac{10}{12}T$

(l) $t = \frac{11}{12}T$

(m) Common legend for $u_x$.

Figure 14: Cyl2DBar: $x$-component, $u_x$ of velocity for twelve timeshots in an oscillation cycle. The oscillation period is denoted $T$.
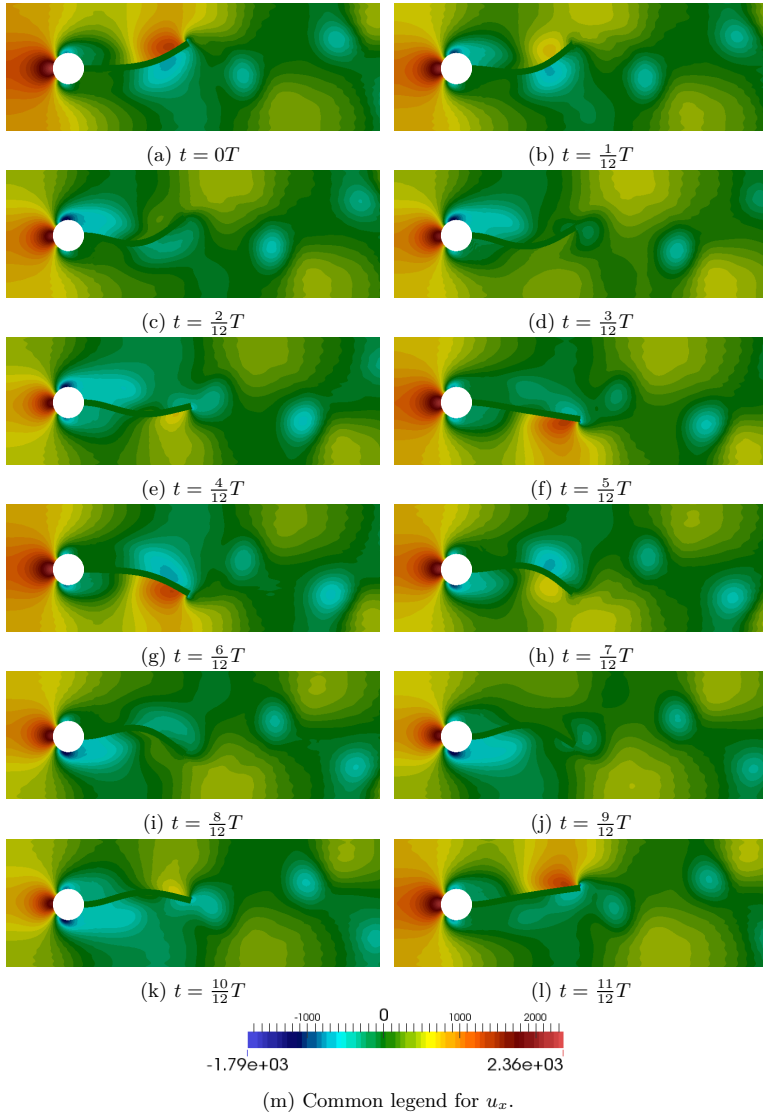
22

(a) $t = 0T$

(b) $t = \frac{1}{12}T$

(c) $t = \frac{2}{12}T$

(d) $t = \frac{3}{12}T$

(e) $t = \frac{4}{12}T$

(f) $t = \frac{5}{12}T$

(g) $t = \frac{6}{12}T$

(h) $t = \frac{7}{12}T$

(i) $t = \frac{8}{12}T$

(j) $t = \frac{9}{12}T$

(k) $t = \frac{10}{12}T$

(l) $t = \frac{11}{12}T$

(m) Common legend for $u_x$.

Figure 15: Cyl2DBar: Pressure for twelve timeshots in an oscillation cycle. The oscillation period is denoted $T$.

23

(a) Average drag force and its variation

(b) $p = 1$

(c) $p = 2$

(d) $p = 3$
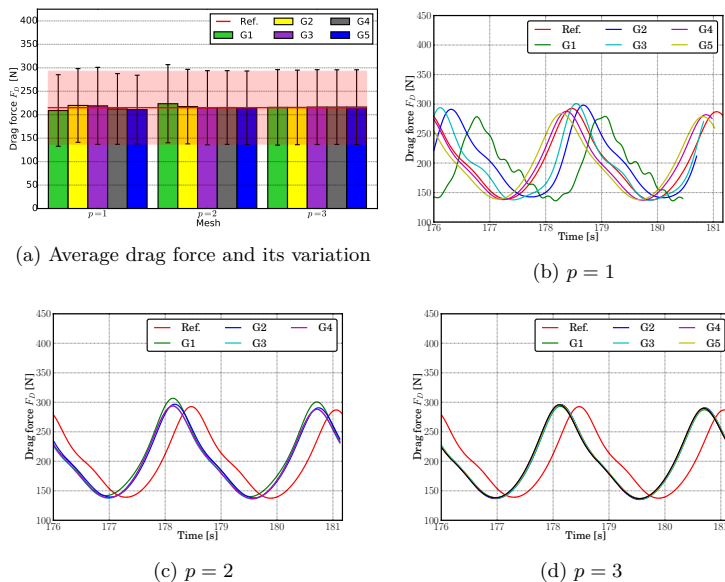
Figure 16: Cyl2DBar: Drag force $F_D$ over the last two cycles for $p = 1, 2, 3$ compared against reference results from [38].

G5 are very close to the reference profile. A promotion from linear to quadratic and then subsequently to cubic elements improves the predication remarkably and the effect is more pronounced for the coarser grids G1 and G2. For the cubic elements, once again, like the drag force, the lift force profiles for different grids collapse on each other. However, again, a lag was observed with respect to the reference profile. When one looks at Table 5 one finds that the predictions of lift frequency for quadratic and cubic elements are within 3% while the error goes up to 11% if linear elements are used with coarsest grid G1.

*4.5. Lateral and transverse displacements*

Figures 18 and 19 present the comparison of lateral and transverse displacements of the center of the tip against the reference values. Once again the comparison is first made of the displacements averaged over a full cycle and then for their evolution as a function of time. A similar trend as above is observed where the linear elements fail to give precise estimates even with very high resolution while the higher order elements give excellent estimates even with the coarsest grid. Frequency results for the displacements are also listed in Table 5.

*4.6. Computational cost for linear, quadratic and cubic elements*

All the simulations were conducted using our in-house CFD code IFEM. The linear solvers are based on the PETSc package [39] version 3.4.2 and are compiled with the Intel C++ compiler version 13.0.1, using the SGI MPT MPI
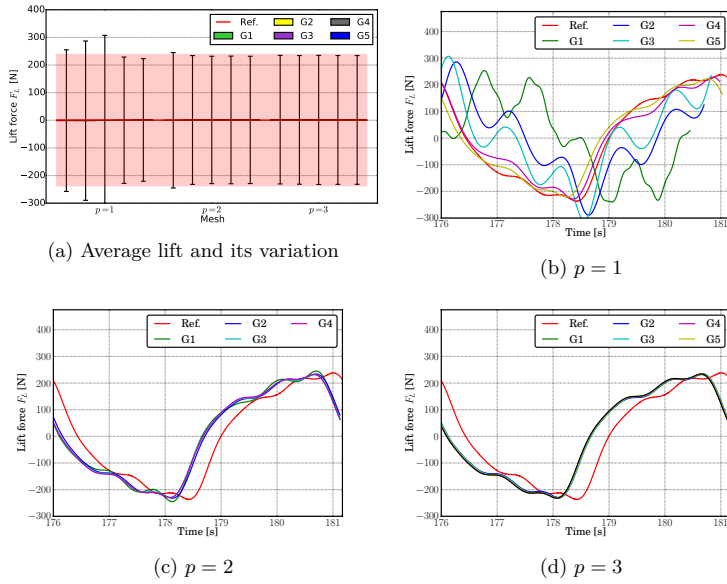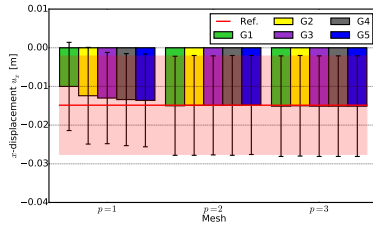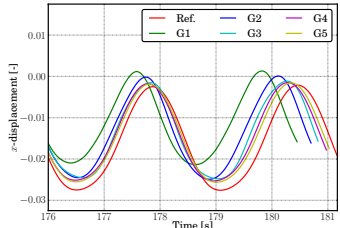
(a) Average lift and its variation



(b) $p = 1$



(c) $p = 2$



(d) $p = 3$

Figure 17: Cyl2DBar: Lift force $F_L$ over the last two cycles for $p = 1, 2, 3$ compared with reference results from [38].
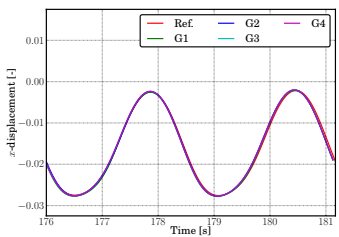
Table 5: Cyl2DBar: Frequency results

|  | $p$ | $f_{F_D}$ | $f_{F_L}$ | $f_{u_x}$ | $f_{u_y}$ |
|---|---|---|---|---|---|
|  | 1 | 4.52 | 2.24 | 4.50 | 2.24 |
| G1 | 2 | 3.92 | 1.94 | 3.87 | 1.94 |
|  | 3 | 3.90 | 1.94 | 3.88 | 1.94 |
|  | 1 | 4.23 | 2.11 | 4.22 | 2.11 |
| G2 | 2 | 3.86 | 1.95 | 3.92 | 1.95 |
|  | 3 | 3.88 | 1.94 | 3.89 | 1.94 |
|  | 1 | 4.09 | 2.06 | 4.11 | 2.06 |
| G3 | 2 | 3.87 | 1.94 | 3.89 | 1.94 |
|  | 3 | 3.90 | 1.94 | 3.87 | 1.94 |
|  | 1 | 3.95 | 2.01 | 3.99 | 2.00 |
| G4 | 2 | 3.87 | 1.94 | 3.89 | 1.94 |
|  | 3 | 3.90 | 1.94 | 3.87 | 1.94 |
|  | 1 | 3.91 | 1.98 | 3.99 | 1.98 |
| G5 | 2 | 3.88 | 1.94 | 3.89 | 1.94 |
|  | 3 | 3.91 | 1.94 | 3.87 | 1.94 |
| Ref. |  | 3.8 | 2.0 | 3.8 | 2.0 |

(a) Average $x$-displacement, $u_x$, and its variation
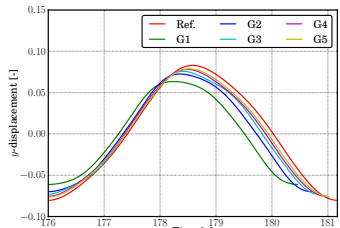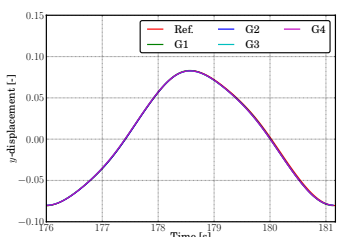
(b) $p = 1$

(c) $p = 2$
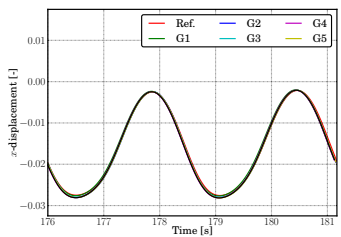
(d) $p = 3$

Figure 18: Cyl2DBar: $x$-displacement $u_x$ over the last two cycles for $p = 1, 2, 3$ compared with reference results from [38].
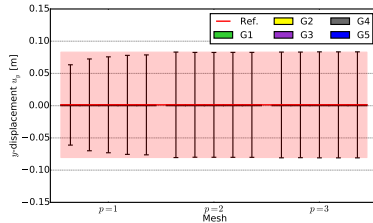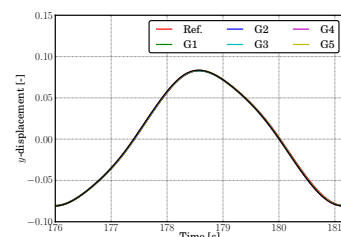


(a) Average $y$-displacement, $u_y$, and its variation

(b) $p = 1$

(c) $p = 2$

(d) $p = 3$

Figure 19: Cyl2DBar: Last two cycles for $p = 2$ compared with reference results from [38].

implementation, all running on SUSE Linux Enterprise Server 11. The simulations were run on the "Vilje" supercomputer at the Norwegian University of Science and Technology which is currently ranked as number 99 on the top 500 list (June 2014). This is an SGI Altix system with Intel Xeon E5-2670 (Sandy Bridge) processors. The 1404 computational nodes in the system consists of 2 octa-core processors in SMP, with 20MB L3 cache per processor. The nodes are connected using a high-speed infiniband network. A plot of the total CPU time required for running the simulations for all grids is shown in Figure 20.
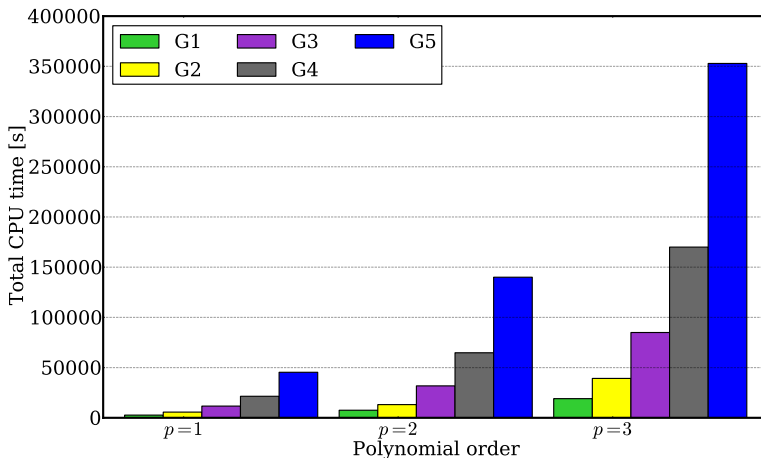


Figure 20: Cyl2DBar: Total CPU time for grids G1-G5 and polynomial orders $p = 1, 2, 3$.

## 5. Conclusions

In this work we have presented a validation of our isogeometric finite element based FSI code against the benchmark FSI case proposed by Turek in [9] and [10]. Effects of different mesh resolutions, stiffness distributions and orders of elements on the estimation of drag, lift and displacements were investigated. Furthermore, four different criteria for mesh generation were imposed resulting in the simulations providing good agreement with the reference data. Most important conclusions from the work can be enumerated as follows:

1. Different mesh stiffness distributions were tested out of which seven were presented in this paper. It turned out that if for a particular mesh stiffness distribution value, the solution converged then they gave the same estimate of quantities of interest, i.e. drag, lift and displacements in the current case. Furthermore, the different mesh stiffness distribution resulted in similar computational cost associated with them.

2. Linear elements are not good even with reasonably fine grid. This can be attributed to the errors associated with interpolation of forces when transferred from fluid to solid domain because of the fact that the geometry can not be represented in an exact form using linear elements. Switching

27

to quadratic or cubic elements led to an exact representation of the geometry in combination with better numerical accuracy resulting in a better estimation of drag, lift and displacements.

3. A switch to quadratic from linear elements resulted in a three-fold increase in the computational time and a seven-fold in the case of cubics. However, from the results it is apparent that the associated accuracy with quadratics was sufficient and gave estimates of the relevant quantities within 5% accuracy.

However, we want to underline the fact that the cases investigated herein were for low Reynolds number ($Re = 100$). Since the ultimate goal of this development work is to understand the fluid-structure interaction of a full rotating turbine under operational meteorological conditions, one will always encounter a very high Reynolds number flow which can be characterized by turbulence. Luckily, work is underway to address this issue and some preliminary study has already been published in the paper [12] for flow simulations around a NACA0012 airfoil for a high Reynolds number, $Re = 3 \times 10^6$. The next step should therefore be to conduct similar fluid-structure simulation for highly turbulent flow using Spalart-Allmaras and variational multiscale approach.

## 6. Acknowledgment

## References

[1] Y. Bazilevs, M.-C. Hsu, J. Kiendl, R. Wüchner, K.-U. Bletzinger, 3D simulation of wind turbine rotors at full scale. Part II: Fluid-structure interaction modeling with composite blades, International Journal for Numerical Methods in Fluids 65 (1-3) (2011) 236–253.

[2] M.-C. Hsu, Y. Bazilevs, Fluid-structure interaction modeling of wind turbines: Simulating the full machine, Computational Mechanics 50 (6) (2012) 821–833.

[3] Y. Bazilevs, A. Korobenko, X. Deng, J. Yan, Novel structural modeling and mesh moving techniques for advanced fluid-structure interaction simulation of wind turbines, International Journal for Numerical Methods in EngineeringArticle in press.

[4] M. Hansen, J. Sørensen, S. Voutsinas, N. Sørensen, H. Madsen, State of the art in wind turbine aerodynamics and aeroelasticity, Progress in Aerospace Sciences 42 (4) (2006) 285–330.

[5] T. Hughes, J. Cottrell, Y. Bazilevs, Isogeometric analysis: CAD, finite elements, NURBS, exact geometry and mesh refinement, Computer Methods in Applied Mechanics and Engineering 194 (39-41) (2005) 4135–4195.

[6] I. Akkerman, Y. Bazilevs, V. Calo, T. Hughes, S. Hulshoff, The role of continuity in residual-based variational multiscale modeling of turbulence, Computational Mechanics 41 (3) (2008) 371–378.

[7] J. Donea, S. Giuliani, J. Halleux, An arbitrary Lagrangian-Eulerian finite element method for transient dynamic fluid-structure interactions, Computer Methods in Applied Mechanics and Engineering 33 (1-3) (1982) 689–723.

[8] J. Donea, A. Huerta, J.-P. Ponthot, A. Rodriguez-Ferran, Encyclopedia of Computational Mechanics, John Wiley, Chichester, West Sussex, 2004, Ch. Arbitrary Lagrangian-Eulerian Methods.

[9] S. Turek, J. Hron, Proposal for numerical benchmarking of fluid-structure interaction between an elastic object and laminar incompressible flow, Tech. rep., University of Dortmund (2006).

[10] S. Turek, J. Hron, M. Madlik, M. Razzaq, H. Wobker, J. Acker, Numerical simulation and benchmarking of a monolithic multigrid solver for fluid-structure interaction problems with application to hemodynamics, Lecture Notes in Computational Science and Engineering 73 LNCSE (2010) 193–220.

[11] J. A. Cottrell, T. J. Hughes, Y. Bazilevs, Isogeometric analysis: toward integration of CAD and FEA, Wiley, Chichester, 2009.

[12] K. Nordanger, R. Holdahl, A. M. Kvarving, A. Rasheed, T. Kvamsdal, Implementation and comparison of three isogeometric Navier-Stokes solvers applied to simulation of flow past a fixed 2D NACA0012 airfoil at high Reynolds number, Computer Methods in Applied Mechanics and Engineering 284 (2015) 664–688.

[13] F. Brezzi, On the existence, uniqueness and approximation of saddle-point problems arising from Lagrangian multipliers, Rev. Francaise Automat. Informat. Recherche Operationelle Ser Rouge 8.

[14] A. J. Chorin, Numerical solution of the Navier-Stokes equations, Mathematics of Computation 22 (1968) 745–762.

[15] R. Temam, Sur l'approximation de la solution des equations de navier-stokes par la methode des pas fractionnaires (ii), Archive for Rational Mechanics and Analysis 33 (5) (1969) 377–385.

[16] P. Minev, A stabilized incremental projection scheme for the incompressible Navier-Stokes equations, International Journal for Numerical Methods in Fluids 36 (4) (2001) 441–464.

[17] H. M. Hilber, T. J. R. Hughes, R. L. Taylor, Improved numerical dissipation for time integration algorithms in structural dynamics, Earthquake Engineering & Structural Dynamics 5 (3) (1977) 283–292.

[18] S. Badia, A. Quaini, A. Quarteroni, Modular vs. non-modular preconditioners for fluid-structure systems with large added-mass effect, Computer Methods in Applied Mechanics and Engineering 197 (49-50) (2008) 4216–4232.

[19] H. Morand, R. Ohayon, Fluid-Structure Interaction: Applied Numerical Methods, Wiley-Masson Series Research in Applied Mathematics, Wiley, 1995.

[20] E. van Brummelen, Added mass effects of compressible and incompressible flows in fluid-structure interaction, Journal of Applied Mechanics, Transactions ASME 76 (2) (2009) 1–7.

[21] P. Le Tallec, J. Mouro, Fluid structure interaction with large structural displacements, Computer Methods in Applied Mechanics and Engineering 190 (24-25) (2001) 3039–3067.

[22] P. Causin, J. Gerbeau, F. Nobile, Added-mass effect in the design of partitioned algorithms for fluid-structure problems, Computer Methods in Applied Mechanics and Engineering 194 (42-44) (2005) 4506–4527.

[23] C. B. Jenssen, T. Kvamsdal, K. M. Okstad, J. Amundsen, Parallel methods for fluid-structure interaction, in: B. Kågström, J. Dongarra, E. Elmroth, J. Waśniewski (Eds.), Applied Parallel Computing Large Scale Scientific and Industrial Problems, Vol. 1541 of Lecture Notes in Computer Science, Springer Berlin Heidelberg, 1998, pp. 263–274.

[24] T. Kvamsdal, C. B. Jenssen, K. M. Okstad, J. Amundsen, Fluid-structure interactions for structural design, in: T. Kvamsdal (Ed.), Computational Methods for Fluid-Structure Interactions, Tapir Publisher, Trondheim, 1999, pp. 211–238.

[25] T. Kvamsdal, K. M. Okstad, K. Sørli, P. Pegon, Two-level adaptive mesh movement algorithms for FSI-computations, in: T. Kvamsdal (Ed.), Computational Methods for Fluid-Structure Interactions, Tapir Publisher, Trondheim, 1999, pp. 121–132.

[26] L. Formaggia, F. Nobile, Stability analysis for the arbitrary lagrangian eulerian formulation with finite elements, East-West Journal of Numerical Mathematics 7 (2) (1999) 105–131.

[27] M. Souli, D. Benson, Arbitrary Lagrangian Eulerian and Fluid-Structure Interaction: Numerical Simulation, ISTE, Wiley, 2010.

[28] Y. Bazilevs, K. Takizawa, T. Tezduyar, Computational Fluid-Structure Interaction: Methods and Applications, Wiley Series in Computational Mechanics, Wiley, 2013.

[29] K. Herfjord, G. Olsen, T. Kvamsdal, K. M. Okstad, Fluid–Structure Interaction in the case of Two Independent Cylinders in Vortex Induced Vibrations (VIV), International Journal of Applied Mechanics and Engineering 7 (2002) 65–83.

[30] K. Stein, T. Tezduyar, R. Benney, Automatic mesh update with the solid-extension mesh moving technique, Computer Methods in Applied Mechanics and Engineering 193 (21-22) (2004) 2019–2032.

[31] R. Bartels, J. Beatty, B. Barsky, An Introduction to Splines for Use in Computer Graphics and Geometric Modeling, Morgan Kaufmann Series in Computer Graphics and Geometric Modeling, Morgan Kaufmann, 1987.

[32] S. A. Coons, Surfaces for computer-aided design of space forms, Tech. Rep. MAC-TR-41, Cambridge, MA, USA (1967).

[33] N. Lomb, Least-squares frequency analysis of unequally spaced data, Astrophysics and Space Science 39 (2) (1976) 447–462.

[34] J. D. Scargle, Studies in astronomical time series analysis. II - Statistical aspects of spectral analysis of unevenly spaced data, The Astrophysical Journal 263 (1982) 835–853.

[35] P. Knupp, Achieving finite element mesh quality via optimization of the Jacobian matrix norm and associated quantities. Part II - A framework for volume mesh optimization and the condition number of the Jacobian matrix, International Journal for Numerical Methods in Engineering 48 (8) (2000) 1165–1185.

[36] C. J. Stimpson, C. D. Ernst, P. Knupp, P. P. Pebay, D. Thompson, The verdict geometric quality library, Tech. Rep. 2007-1751, Sandia National Laboratories (2007).

[37] P. Knupp, Algebraic mesh quality metrics for unstructured initial meshes, Finite Elements in Analysis and Design 39 (3) (2003) 217–241.

[38] S. Turek, FEATFLOW Web page, http://www.featflow.de/en/benchmarks/cfdbenchmarking/fsi_benchmark.html (2014).

[39] S. Balay, S. Abhyankar, M. F. Adams, J. Brown, P. Brune, K. Buschelman, V. Eijkhout, W. D. Gropp, D. Kaushik, M. G. Knepley, L. C. McInnes, K. Rupp, B. F. Smith, H. Zhang, PETSc Web page, http://www.mcs.anl.gov/petsc (2014).